

25 ABSTRACT

26 Magma-carbonate interaction is an increasingly recognised process occurring at active volcanoes
27 worldwide, with implications for the magmatic evolution of the host volcanic systems, their eruptive
28 behaviour, volcanic CO₂ budgets, and economic mineralisation. Abundant calc-silicate skarn xenoliths are
29 found at Merapi volcano, Indonesia. We identify two distinct xenolith types: magmatic skarn xenoliths,
30 which contain evidence of formation within the magma, and exoskarn xenoliths, which more likely
31 represent fragments of crystalline metamorphosed wall-rocks. The magmatic skarn xenoliths comprise
32 distinct compositional and mineralogical zones with abundant Ca-enriched glass (up to 10 wt% relative to
33 lava groundmass), mineralogically dominated by clinopyroxene (En₁₅₋₄₃Fs₁₄₋₃₆Wo₄₁₋₅₁) + plagioclase
34 (An₃₇₋₁₀₀) ± magnetite in the outer zones towards the lava contact and by wollastonite ± clinopyroxene
35 (En₁₇₋₃₈Fs₈₋₃₄Wo₄₉₋₅₉) ± plagioclase (An₄₆₋₁₀₀) ± garnet (Grs₀₋₆₅Adr₂₄₋₇₅Sch₀₋₇₆) ± quartz in the xenolith
36 cores. These zones are controlled by Ca transfer from the limestone protolith to the magma and by
37 transfer of magma-derived elements in the opposite direction. In contrast, the exoskarn xenoliths are
38 unzoned and essentially glass-free, representing equilibration at sub-solidus conditions. The major
39 mineral assemblage in the exoskarn xenoliths is wollastonite + garnet (Grs₇₃₋₉₇Adr₃₋₂₄) + Ca-Al-rich
40 clinopyroxene (CaTs₀₋₃₈) + anorthite ± quartz, with variable amounts of either quartz or melilite (Geh₄₂₋₉₁)
41 + spinel. Thermobarometric calculations, fluid inclusion microthermometry and newly calibrated
42 oxybarometry based on Fe³⁺/ΣFe in clinopyroxene indicate magmatic skarn xenolith formation conditions
43 of ~850 ± 45°C, < 100 MPa and at an oxygen fugacity between the NNO and HM buffer. The exoskarn
44 xenoliths, in turn, formed at 510-910°C under oxygen fugacity conditions between NNO and air. These
45 high oxygen fugacities are likely imposed by the large volumes of CO₂ liberated from the carbonate.
46 Halogen and sulphur-rich mineral phases in the xenoliths testify to the infiltration by a magmatic brine. In
47 some xenoliths this is associated with the precipitation of copper-bearing mineral phases by sulphur
48 dissociation into sulphide and sulphate, indicating potential mineralisation in the skarn system below
49 Merapi. Compositions of many xenolith clinopyroxene and plagioclase crystals overlap with that of
50 magmatic minerals, suggesting that the crystal cargo in Merapi magmas may contain a larger proportion
51 of skarn-derived xenocrysts than previously recognised. Assessment of xenolith formation timescales
52 demonstrates that magma-carbonate interaction and associated CO₂ release could affect eruption intensity,
53 as recently suggested for Merapi and similar carbonate-hosted volcanoes elsewhere.

54 Key words: Merapi; magma-carbonate interaction; skarn; xenolith; carbonate assimilation; oxybarometry

55

57 INTRODUCTION

58 Calc-silicate (skarn) xenoliths are found within the deposits of many hazardous arc volcanoes worldwide,
59 including Popocatepetl (e.g. Goff *et al.*, 2001), Vesuvius (e.g. Fulignati *et al.*, 2001), Merapi
60 (e.g. Chadwick *et al.*, 2007), Colli Albani (e.g. Di Rocco *et al.*, 2012) and Nisyros (Spandler *et al.*, 2012).
61 Formed as a result of interaction between crustal carbonate and the host magmatic system, these xenoliths
62 preserve evidence of complex reaction processes that can have profound impact on the host magmatic
63 system, including altering magmatic differentiation paths (e.g. Iacono-Marziano *et al.*, 2008), influencing
64 eruptive dynamics (e.g. Freda *et al.*, 2011; Troll *et al.*, 2012; Carr *et al.*, 2018), and liberating large
65 volumes of crustal CO₂ into the atmosphere (e.g. Mason *et al.*, 2017).

66 Much of the knowledge about crustal magma-carbonate interaction processes has been derived from
67 diverse approaches. Isotope mass balance calculations (e.g. Troll *et al.*, 2012, 2013; Jolis *et al.*, 2015)
68 have shown that large volumes of crustal carbonate, up to 30%, are incorporated into some volcanic
69 systems, and *in situ* stable isotopes have demonstrated decarbonation is highly efficient in magmatic
70 systems (Whitley *et al.*, 2019). Experimental magma-carbonate studies (e.g. Iacono-Marziano *et al.*,
71 2008; Deegan *et al.*, 2010; Jolis *et al.*, 2013; Blythe *et al.*, 2015; Carter and Dasgupta, 2016) have further
72 demonstrated how magmatic melt differentiation paths are modified towards silica undersaturation in
73 mafic melts, and that magma-carbonate interaction may be extremely rapid (syn-magmatic), operating on
74 the order of minutes to hours. Moreover, detailed petrographical and geochemical studies of the
75 individual xenoliths have provided insights into the architecture of subvolcanic skarn contact aureoles
76 (Matthews *et al.*, 1996; Fulignati *et al.*, 2004), the depth of magma-carbonate interaction from fluid
77 inclusions (Clocchiatti *et al.*, 1982), xenocryst incorporation into the magma and skarn recycling
78 (Chadwick *et al.*, 2007; Jolis *et al.*, 2015), changes in magmatic redox conditions and phase equilibria
79 (Wenzel *et al.*, 2002), and the economic metallogenic potential of magmatic fluids that interact with the
80 country rock (Fulignati *et al.*, 2013).

81 In this study, we present a detailed analysis of the petrography, mineralogy and geochemistry of calc-
82 silicate xenoliths from the 1994-2010 eruptions of Merapi volcano, Indonesia. We demonstrate that these
83 xenoliths represent fragments of either complete replacement of carbonate wall rock to calc-silicate
84 mineral assemblages around the magma reservoir margins, or are transient fragments of entrained
85 carbonate which are caught in the process of being metamorphosed within the magma itself. The
86 xenoliths record evidence of interaction with a magmatic-derived halogen-bearing fluid that produced
87 exotic halogen-bearing mineral phases, whilst enriching the xenoliths in economically important metals
88 such as copper and iron, and by analogy the more extensive skarn system below Merapi. We also show

89 that traditional mineral-melt thermobarometry and fluid inclusion analysis can be applied to some of the
90 xenoliths, and we present a new calibration of a single clinopyroxene crystal oxybarometer to determine
91 intensive variables (T, P, fO_2) during xenolith formation.

92 **GEOLOGICAL BACKGROUND**

93 Merapi is the most active of Indonesia's volcanoes, and is considered one of the Sunda arc's most
94 dangerous (e.g. Voight *et al.*, 2000; Gertisser *et al.*, 2011, 2012; Surono *et al.*, 2012). Activity is near
95 continuous, with periods of dome growth frequently interrupted by gravitational dome collapse and
96 associated pyroclastic density currents (e.g. Andreastuti *et al.*, 2000; Camus *et al.*, 2000; Newhall *et al.*,
97 2000; Voight *et al.*, 2000; Gertisser *et al.*, 2012). Larger explosive Vulcanian and sub-Plinian eruptions
98 occur at longer ~100 year time-scales, such as the 2010 VEI 4 eruption which killed close to 400 people
99 (Surono *et al.*, 2012; Komorowski *et al.*, 2013). Compositionally, the erupted material is medium to high-
100 K basalt to basaltic andesite with a restricted range of ~49 to 58 wt% SiO₂ (Gertisser and Keller, 2003a,
101 2003b). Early work at Merapi suggested a subducted sediment contamination component to the Merapi
102 magmas (Gertisser and Keller, 2003b), while subsequent work also highlighted a significant influence
103 from crustal carbonate on magma genesis (e.g. Chadwick *et al.*, 2007; Troll *et al.*, 2013; Aiuppa *et al.*,
104 2017). Merapi overlies an upper crust of 8 to 11 km thick sediments of the Kendeng basin, where
105 Cretaceous to Cenozoic volcanoclastic sediments are overlain by shallow marine limestones and marls, all
106 of which overlie inferred Cretaceous arc and ophiolite basement rocks (van Bemmelen, 1949; Smyth *et*
107 *al.*, 2005). Fragments of the sedimentary basement are frequently found as thermally metamorphosed
108 xenoliths within the eruptive deposits (Brouwer, 1928; Clocchiatti *et al.*, 1982; Camus *et al.*, 2000;
109 Gertisser and Keller, 2003b; Chadwick *et al.*, 2007; Troll *et al.*, 2012, 2013). These xenoliths testify to
110 prevalent magma-carbonate interaction (Chadwick *et al.*, 2007; Troll *et al.*, 2013; Whitley *et al.*, 2019), a
111 process that is ongoing and occurs at rapid timescales (Deegan *et al.*, 2010, 2011; Troll *et al.*, 2012;
112 Reagan *et al.*, 2017). Radiogenic (⁸⁷Sr/⁸⁶Sr) and stable ($\delta^{13}C$, $\delta^{18}O$) isotope analysis of bulk xenoliths and
113 mineral separates of calc-silicate mineral phases (wollastonite, diopside, calcite), have been used to
114 demonstrate up to 30% crustal carbonate assimilation during the genesis of Merapi magmas (Chadwick *et*
115 *al.*, 2007; Troll *et al.*, 2013; Whitley *et al.*, 2019). Liberation of large volumes of crustal CO₂ during syn-
116 magmatic activity has additionally been linked to enhancing eruptive explosivity at Merapi (e.g. Troll *et*
117 *al.*, 2012, 2013; Borisova *et al.*, 2013; Carr *et al.*, 2018). The available evidence thus indicates that
118 magma-carbonate interaction at Merapi may have wide-ranging implications for the magmatic evolution
119 and volcanic hazard potential at Merapi.

120 METHODS

121 Scanning electron microscopy was undertaken at Keele University, UK using a Hitachi TM3000 scanning
122 electron microscope. A rare unknown mineral found in sample MX1, compositionally similar to wadalite,
123 was analysed with Raman spectroscopy at Keele University using a confocal Thermo Scientific DXR
124 Raman spectrometer with a 532 nm laser, a 50x objective, and a standard 30 µm uncovered polished thin
125 section.

126 Microthermometry was carried out at Keele University using a Linkam THMS600 freezing-heating stage.
127 Thermocouples were calibrated at -56.6°C, 0.0°C and +374.1°C using synthetic fluid inclusions provided
128 by Linkam. The precision of temperature measurements at -56.6°C is ±0.1°C, and ±2°C at 374.1°C.
129 Measurements were made on ~100 µm thick double polished wafer fragments.

130 Major element concentrations in minerals, and major element, chlorine and sulphur concentrations in
131 groundmass glasses and melt inclusions were determined with a JXA 8900R Electron Probe
132 Microanalyser at the University of Kiel, Germany. Silicate and oxide minerals were analysed with a 15
133 kV accelerating voltage, a 15 nA beam current and a 2 µm beam diameter. Calcite was measured with a 7
134 µm beam diameter at 15 kV accelerating voltage and a 10 nA beam current. Glasses were measured with
135 a 5 µm beam at 15 kV accelerating voltage and a 12 nA beam current. Measurement times were 15 s at
136 the peak and 7 s on the background, excluding S, Cl, P which were measured for 30 s at the peak and 10s
137 on the background. Extended counting times of 30 s peak and 10 s background for Fe, Mg and Mn, and
138 60 s peak and 30 s background for Ba and Sr were applied during calcite analyses. Na was measured first
139 to minimise alkali migration. Natural mineral standards were used for calibration and Smithsonian
140 basaltic glass A-99, forsterite 83 USNM2566, plagioclase USNM115900, garnet RV2 USNM 87375, and
141 obsidian ASTIMEX Block SPGLASS7 were used as secondary within run standards to assess accuracy
142 and precision, presented in the supplementary material.

143 All Mg# values were calculated assuming all Fe as Fe²⁺ using $Mg\# = 100 \frac{Mg}{Mg+Fe_{total}}$. Ternary
144 clinopyroxene components are calculated assuming all Fe as Fe²⁺ e.g. $Fs = 100 \frac{Fe_{total}}{Mg+Fe_{total}+Ca}$. Fe³⁺ was
145 estimated for clinopyroxene from stoichiometry using Droop (1987). Al^{IV} was calculated as 2-Si, and any
146 remaining Al was allocated as Al^{VI}. Components for clinopyroxene thermobarometry were calculated
147 using Putirka *et al.* (1996). Garnet end member mole fractions and Fe³⁺ were estimated using the Arai
148 (2010) R script implementation of the Muhling and Griffin (1991) calculation scheme, which provides a
149 more accurate Fe³⁺ estimate for garnet than Droop (1987). Melilite mole fractions were calculated
150 considering 4 end members by firstly allocating Na to the Na-melilite end member, and then the
151 remaining cations, minus the Al required for Na-melilite, were allocated between gehlenite, åkermanite
152 and Fe-åkermanite. These mole fractions were calculated as follows (abbreviations as in Table 1):

$$\begin{aligned}
 153 \quad \text{Na-Mel} &= \frac{Na}{Na + Ca - 1} \\
 154 \quad \text{Geh} &= (1 - \text{Na-Mel}) \cdot \frac{\frac{Al-2Na}{2}}{\frac{Al-2Na}{2} + Fe + Mg} \\
 155 \quad \text{Ak} &= (1 - \text{Na-Mel}) \cdot \frac{Mg}{\frac{Al-2Na}{2} + Fe + Mg} \\
 156 \quad \text{Fe-Ak} &= (1 - \text{Na-Mel}) \cdot \frac{Fe}{\frac{Al-2Na}{2} + Fe + Mg}
 \end{aligned}$$

157 Due to the small size of most xenoliths (typically < 5 cm) combined with the textural and mineralogical
 158 uniqueness of each sample, whole-rock compositions for six representative xenoliths were determined by
 159 point counting (1000-2000 points) combined with averaged mineral and glass chemistry. Each zone was
 160 counted individually, then the respective areas of the zones were combined to calculate a whole-rock
 161 composition. The zone and whole-rock compositions were corrected for varying mineral densities using
 162 mineral densities from Deer *et al.* (1997) and the bulk compositions were obtained using the Rock-Maker
 163 spreadsheet (Büttner, 2012), which generates bulk compositions from mineral volumes. All calculated
 164 compositions are presented in the supplementary material.

165 All data produced in this study are found as supplementary material, including the collated published
 166 datasets used to produce the figures.

167 Thermodynamic modelling of the exoskarn samples MX99-5s and MX99-3s was undertaken using the
 168 Theriak-Domino software (built date 3-1-2012, de Capitani and Petrakakis, 2010), using calculated
 169 whole-rock compositions (see above) in the system Si-Al-Fe-Mg-Ca-C. The database used (Holland and
 170 Powell, 1998, version 5.5) lacks solid solution models that include the CaTs component in clinopyroxene,
 171 and mixing between gehlenite and åkermanite. Therefore, ideal mixing was assumed for these two solid
 172 solutions (Charlu *et al.*, 1981; Povoden *et al.*, 2002). Implementing a CaTs-Di-Hd ideal mixing model for
 173 clinopyroxene over the default database model however has little effect on the calculated phase
 174 boundaries of the system. For example, this clinopyroxene model produces only a ~20°C variation in
 175 melilite-garnet phase boundaries, which is relevant to the xenoliths.

176

177 **PETROGRAPHY**

178 Calc-silicate xenoliths ($n=33$) collected from the 1994 to 2010 eruption deposits at Merapi can be
 179 subdivided into three distinct groups (magmatic skarn $n=25$, exoskarn $n=5$ and buchite $n=3$) on the basis

180 of their dominant mineralogy, modal zonation, and the presence of glass. Twelve xenoliths that best
181 represent the three groups, and which highlight the mineralogical and textural variety of the xenoliths
182 were chosen for detailed study. The xenoliths are generally centimetre to tens of centimetre in size, and
183 texturally complex variations in mineralogy and zonation can be seen at hand specimen scale.
184 Volcaniclastic and metasedimentary xenoliths are additionally present at Merapi but not discussed in this
185 paper (see Chadwick *et al.*, 2007). A summary of the mineral phases identified in this study and their
186 formulas are presented in Table 1.

187 **Magmatic Skarn xenoliths**

188 The most abundant calc-silicate xenolith type ($n=25$) is the one we term ‘magmatic skarn’ (*c.f.* Fulignati
189 *et al.*, 2004) based on the abundance of Ca-enriched magmatic glass, melt inclusions in the newly formed
190 calc-silicate skarn minerals, and pronounced reaction zones at contacts with the host lava. Attempting to
191 explain the variety of xenoliths in this group, the magmatic skarn xenoliths are subdivided into a series of
192 idealised mineralogical/textural zones, such as a series of reaction zones and a core zone (Figs. 1, 2). The
193 lava contact (R1) is represented by a zone of coarse (100-300 μm), pale green clinopyroxene and a
194 concentration of magnetite (Fig. 2A). This is followed by a finer grained (up to 100 μm) zone (R2) of
195 plagioclase + clinopyroxene \pm glass (Fig. 2A), with rare amphibole also present in sample MX1. This
196 zone grades into a zone of coarse dark green/yellow pleochroic clinopyroxene (R3) separating R2 from a
197 zone of vesicular glass (R4) (Fig. 2A-B). The glass zone typically contains strongly irregularly Fe-Mg
198 zoned (see mineral chemistry), colourless to deep green/yellow pleochroic diopsidic clinopyroxene
199 crystals (Fig. 2B). These clinopyroxene crystals are similar to those of zone R3, and often appear to be
200 incorporated from zone R3. Plagioclase and wollastonite microlites are additionally present within the
201 glass. Sample MX5 has comparatively large quartz and plagioclase crystals ($\sim 100 \mu\text{m}$) within the glass
202 zone, and sample MX3 shows this zone to be almost fully crystallised to quartz and plagioclase, with
203 scarce melt inclusions within the quartz crystals. The xenolith core (Fig. 2C) has a sharp contact to
204 decussate wollastonite, but occasionally the core is a mixture of wollastonite, clinopyroxene, and
205 accessory garnet. Additionally, glass is often present within the core of these xenoliths. At glass-
206 wollastonite contacts, a thin rim of semi-dendritic ferrobustamite often forms. The samples have a
207 vesicular texture across all zones.

208 The described zonation is idealised, and variations naturally occur. Samples MX1 and M13-10, for
209 instance, show no glass zone (R4) separating the wollastonite-dominant core from R3 and R2. In this
210 case, a pale yellow clinopyroxene and garnet zone formed instead of the coarse clinopyroxene of zone R3,
211 which we call R3b (Figs. 1, 2D). This clinopyroxene is optically and chemically distinct (CaTs:
212 CaAlAlSiO_6 rich, see section Mineral Chemistry) from any others in the Merapi magmatic skarn
213 xenoliths. In sample MX1, one half of the xenolith shows the common zonation (with glass zone R4

214 present), whilst the other half has no glass and instead has the zone R3b CaTs clinopyroxene and garnet
215 zone (Fig. 1). Rare patches of garnet are found interstitial to wollastonite in the MX1 core, and also
216 together with wollastonite and CaTs clinopyroxene in sample CS16.

217 Accessory phases are generally restricted to the xenolith cores, and include calcite, titanite, chromite,
218 gehlenite, a wadalite-like Si-Al-Fe-Ca-O-Cl mineral, perovskite, a Ca-Zr-Ti-O mineral, cotunnite,
219 sulphates (anhydrite and baryte) and sulphides (pyrrhotite and cubanite) (Table 1). Titanite is also present
220 within the glass in zone R4 and ilmenite is exclusively found in sample MX3 in zone R2. Calcite is
221 present as four distinct textural types: 1) globular crystals within the glass R4 zone, 2) interstitial to
222 wollastonite in the cores, 3) inclusions in wollastonite and garnet, and 4) a melt-like infiltrative texture
223 containing rare Cl-F rich phases such as fluorite, cuspidine and the wadalite-like mineral within regions
224 where the calcite pools (Fig. 3A-B). These calcites are discussed in detail in Whitley *et al.* (2019).

225 Many crystals contain significant quantities of melt inclusions (Fig. 3C-G), exceeding 80 in a single 600
226 μm long wollastonite crystal. Melt inclusions are also present in clinopyroxene of zones R3-4, plagioclase
227 in zone R4 and titanite within the xenolith cores. The inclusions are most commonly glassy and have a
228 single shrinkage bubble but, in rare cases, they can contain daughter crystals and multiple bubbles. The
229 daughter crystals are found either in the glass or in the bubble, and are most commonly Fe-bearing phases
230 (pyrrhotite, cubanite, magnetite) and occasionally apatite. Vapour-rich CO_2 fluid inclusions are also
231 common in wollastonite.

232 **Exoskarn Xenoliths**

233 Exoskarn xenoliths are distinct from the magmatic skarn xenoliths by having a different mineralogy,
234 lacking mineralogical zonation, and by almost entirely lacking glass. On the basis of their mineral
235 assemblages resembling typical high temperature skarns worldwide (e.g. Meinert, 1992), and the lack of
236 glass, which indicates formation by subsolidus reactions, we classify these xenoliths as exoskarns (*c.f.*
237 Fulignati *et al.*, 2004, see also discussion). These xenoliths comprise two distinct skarn mineral
238 assemblages (A and B), often with a rim of clinopyroxene and plagioclase at the host lava contact. The
239 most common assemblage (A) is wollastonite + garnet + plagioclase \pm CaTs clinopyroxene \pm quartz \pm
240 calcite with a granoblastic texture (Fig. 4A). Some clinopyroxenes and garnets exhibit weak patchy
241 zonation. Accessory S, Cl, and F-bearing phases such as cuspidine, ellestadite, anhydrite and pyrrhotite
242 are additionally present, and also unidentified Ca-Al-Si-Cl-F minerals that are distinct from the wadalite-
243 like mineral in the magmatic skarn xenoliths. No hydrous phases that can often occur in skarns, such as
244 epidote and vesuvianite (*c.f.* Meinert, 1992), have been identified in this study, although epidote and
245 prehnite have been identified in earlier descriptions of Merapi xenoliths (Kerinec, 1982; Camus *et al.*,
246 2000). Garnet often contains inclusions of plagioclase and wollastonite. Calcite is present as either rare
247 inclusions within garnet crystals or as large mm-sized crystals, surrounded by complex reaction rims that

248 contain larnite, spurrite, and Ca-Si-rich S-Cl-F-bearing phases including fluorite, cuspidine, ellestadite,
249 anhydrite, and many additional unidentified phases (Ca-Si-O, Ca-Al-Si-O, Ca-Al-Si-P-O Table 8, Fig.
250 4B). Xenotime and monazite form accessory inclusions within these calcites.

251 The second assemblage (B), only found in one sample (MX99-3s), comprises gehlenite + grossular garnet
252 + CaTs clinopyroxene + spinel + wollastonite + plagioclase, with trace amounts of ellestadite (Fig. 4C).
253 This sample shows evidence for disequilibrium, such as patchy compositional zoning of garnets, and
254 spinel with rims of gehlenite followed by an outer rim of CaTs clinopyroxene. Patches of localised
255 equilibrium are shown by granular $\sim 120^\circ$ triple junctions in the gehlenite-dominant areas of the sample.

256 **Buchite**

257 These rare xenoliths (samples M13-04C, CS14, CS10) contain abundant (> 70 vol%) quartz (or SiO₂
258 polymorphs) with interstitial glass around the crystal borders, and minor small interstitial clinopyroxene,
259 plagioclase and wollastonite (Supplementary Fig. S1). Patches of clinopyroxene-rich glass are present,
260 similar to zone R4 of the magmatic skarn xenoliths. We have classified these samples as buchites
261 (pyrometamorphic glass-rich rocks), following the classification by Matthews *et al.* (1996) of texturally
262 similar xenoliths at Lascar volcano, Chile. Similar quartz-rich, partially melted xenoliths have also been
263 described from the Aeolian islands (e.g. Frezzotti *et al.*, 2004; Zanon and Nikogosian, 2004; Del Moro *et*
264 *al.*, 2011), Etna (Mollo *et al.*, 2017) and the Central Apennines (Melluso *et al.*, 2003). Although the
265 quartz-rich assemblage could be derived from a volcanoclastic protolith, the presence of wollastonite
266 suggests a carbonate or marl component. The rounded shape of the quartz crystals, separated by
267 interstitial glass, indicates that partial melting has occurred. The dissolution of quartz xenocrysts in arc
268 magmas was observed in products of the 1991 Pinatubo eruption, where highly silicic glass (~ 80 -85 wt.%
269 SiO₂) formed in reaction zones around the xenocrysts, pointing to possible compositional modifications of
270 the melt, at least on a micrometre scale (Borisova *et al.*, 2014). However, although the Merapi buchite
271 xenoliths are briefly mentioned here for completeness, details of their occurrence and potential
272 ramifications for melt chemistry at Merapi are beyond the scope of the current study and will not be
273 discussed further.

274 **RESULTS**

275 **Whole-Rock Major Element Chemistry**

276 Calculated major element compositions of individual zones in magmatic xenoliths are compared for two
277 selected samples to evaluate chemical changes (Fig. 5). There are distinct differences between the zones
278 and some systematic variations from the lava contact towards the xenolith cores point to a progressive
279 change from magmatic to calcic compositions (Fig. 5A; Supplementary Figs. S2, S3) (*c.f.* Troll *et al.*,

280 2012). CaO contents are lowest in the lavas and highest in the xenolith cores, whereas Al₂O₃ contents
281 show exactly the opposite behaviour. One xenolith (sample MX1) shows a systematic increase in CaO
282 from the contact towards the core, except for glass zone R4 that creates a distinct anomaly in the element
283 profiles, having higher SiO₂ and lower CaO than the adjacent zones. FeO is relatively enriched in zone
284 R1, decreasing towards the core, whereas SiO₂ is lowest in this zone. MgO shows only limited variation
285 and has the lowest contents in the innermost zone (R4) and in the core.

286 In terms of whole rock major element composition (Fig. 5B), magmatic skarn xenoliths fall within the
287 range of xenoliths analysed by Chadwick *et al.* (2007), which we believe classify as magmatic skarn
288 xenoliths in our grouping), forming diverging trends from basaltic-andesite compositions. Magmatic
289 skarn xenoliths have lower Al₂O₃ contents than lavas (< 16 wt%), while exoskarn xenoliths display Al₂O₃
290 contents comparable to lava values (18 to 25 wt%), although at a much lower SiO₂ content (33 to 45
291 wt%). All xenoliths have much higher CaO than the lavas, up to 36 wt%, but lower TiO₂ and K₂O
292 contents. FeO and MgO span the range of lava values, with FeO up to 10.0 wt%, and MgO up to 6.6 wt%.
293 Exoskarn xenoliths generally plot distinct from magmatic skarn xenoliths when considered with the
294 Chadwick *et al.* (2007) data (Fig. 5B). For instance, the exoskarn xenoliths have low SiO₂, TiO₂ and FeO,
295 relative to the magmatic skarn xenoliths, but form a linear trend of decreasing TiO₂ and FeO with
296 increasing SiO₂.

297 Mineral Chemistry

298 *Feldspar*

299 Feldspar compositions in the Merapi calc-silicate xenoliths are entirely plagioclase, but spanning a wide
300 compositional range (An₄₆₋₁₀₀) (Table 2). In magmatic skarn xenoliths, anorthite content progressively
301 increases towards the xenolith cores (Fig. 6A). Zoning is relatively insignificant compared to the
302 differences between zones. Magmatic skarn xenolith plagioclase comprises both microlites (An₄₆₋₅₉)
303 within the interstitial glass in zone R4, and interstitial plagioclase in the high-An cores (An₇₃₋₁₀₀). Where
304 analyses of the host lava attached to the xenolith were possible (An₂₉₋₈₁), plagioclase in zones R2 and R4
305 overlap magmatic plagioclase compositions, including the previously published data (Gertisser, 2001;
306 Preece, 2014; Erdmann *et al.*, 2016). In An-FeO space, xenolith core plagioclase compositions generally
307 fall within and extend the high FeO-An compositional ellipse of Merapi xenolith plagioclase from
308 Chadwick *et al.* (2007) (Fig. 6B). Plagioclase microlites within the zone R4 glass have strong FeO
309 enrichment (up to 1.7 wt% FeO), as is observed with the strong FeO enrichment of both clinopyroxene
310 and ferrobustamite overgrowths on wollastonite within this glass zone (see below). Exoskarn plagioclase
311 is essentially pure anorthite, with lower anorthite contents restricted to the lava contact (Table 2). FeO
312 concentrations in exoskarn anorthite are characteristically lower than those of magmatic plagioclase and
313 the majority of the magmatic skarn plagioclase data.

314 *Clinopyroxene*

315 Clinopyroxene compositions range from quadrilateral diopside-hedenbergite (Di-Hd) (Morimoto, 1988)
316 to high-Al diopside (Table 3). These high Al clinopyroxenes are enriched both in esseneite
317 ($\text{CaFe}^{3+}\text{AlSiO}_6$) and Calcium-Tschermak's (CaTs: CaAlAlSiO_6) components, demonstrated by the strong
318 correlation between Fe^{3+} and Al^{IV} ($R^2=0.88$, Fig. 7A), and Al^{IV} with Al^{VI} ($R^2=0.81$, not shown) across all
319 analysed crystals. Incorporation of Al^{IV} is accommodated by a strong reduction of Si in the tetrahedral
320 site. These clinopyroxenes are commonly generalised as fassaite [$\text{Ca}(\text{Mg},\text{Fe}^{3+},\text{Al})(\text{Si},\text{Al})_2\text{O}_6$] where Al^{IV}
321 > 0.25 ; Deer *et al.* (1997)]. As this is not a formal name (Morimoto, 1988) and the clinopyroxenes show
322 an enrichment in the CaTs component, we refer to these clinopyroxenes as CaTs-clinopyroxene in this
323 manuscript.

324 In magmatic skarn xenoliths, the clinopyroxene compositions are generally comparable to Merapi
325 magmatic clinopyroxenes in zone R1 (Fig. 7A-C), and progressively become more Ca/wollastonite-rich
326 until sitting along the diopside-hedenbergite (Di-Hd) join (Wo_{50}) in zones R3, R4 and in the core (Fig.
327 7C). There is a sharp compositional change at zone R4 and within the core, where the clinopyroxenes
328 closely follow the Di-Hd join and progressively become more Hd-rich (Fig. 7C). Xenolith core
329 clinopyroxenes can also be enriched in Al_2O_3 (up to 11.57 wt%, corresponding to 18 mol% CaTs),
330 bringing compositions above the DiHd join in the traditional clinopyroxene composition ternary
331 diagrams, although this is uncommon and only observed in sample CS16. These Al-rich clinopyroxenes
332 are strongly zoned, from this Al-rich core to weakly oscillatory Di-Hd zoned mantle and rim zones (Fig.
333 7E). Commonly however, magmatic skarn xenolith clinopyroxene zonation is restricted to the Di-Hd join
334 (Fig. 7C), with patchy, highly irregular resorption surfaces (Fig. 7F). Titanium is correlated well with Al^{IV}
335 across the magmatic skarn xenolith zones, excluding zone 3b, where CaTs-rich clinopyroxenes form with
336 low Ti, comparable to the compositionally distinct exoskarn xenolith clinopyroxene (Fig. 7B).

337 Exoskarn clinopyroxenes are highly Al enriched (Fig. 7A, B, D; Table 3), containing up to 22.3 wt%
338 Al_2O_3 , approaching the highest natural terrestrial values known to the authors (24.0 wt% in gehlenite-rich
339 skarns from the Carpathians, Romania; Pascal *et al.*, 2005). $\text{Fe}^{3+}/\Sigma\text{Fe}$ (calculated following Droop, 1987)
340 approaches unity (Fig. 7A). Clinopyroxene compositions at the exoskarn xenolith rim overlap magmatic
341 compositions, but then immediately jump to highly Al-rich compositions, usually lacking the gradual
342 progression observed in the magmatic skarn xenoliths (Fig. 7A-C).

343 *Pyroxenoids*

344 Wollastonite, present in all xenoliths, ranges from essentially pure CaSiO_3 to 5 mol% FeSiO_3 with < 1.5
345 mol% MnSiO_3 (Fig. 8A; Table 3). Wollastonite compositions from 17 to 21 mol% FeSiO_3 are attributed
346 to the ferrobustamite member of the wollastonite group rather than iron-rich wollastonite, as bustamite is
347 the stable crystal structure above ~ 12 mol% FeSiO_3 (Rutstein, 1971; Rutstein and White, 1971). The

348 ferrobustamite crystals are found as overgrowth crystals on wollastonite in the glass-bearing magmatic
349 skarn xenoliths, in rare inclusions in wollastonite in magmatic skarn xenoliths, and in accessory phases in
350 the calcite reaction rims in large calcite-bearing exoskarn xenoliths.

351 *Garnet*

352 Garnet is found predominantly in the exoskarn xenoliths as a main rock forming mineral, with magmatic
353 skarn xenolith garnet restricted to small interstitial patches in the cores or in zone R3b (Figs. 1, 2B).
354 Garnet compositions across all xenolith types closely follow the grossular ($\text{Ca}_3\text{Al}_2\text{Si}_3\text{O}_{12}$)–andradite
355 ($\text{Ca}_3\text{Fe}^{3+}_2\text{Si}_3\text{O}_{12}$) join, with only schorlomite ($\text{Ca}_3\text{Ti}_2\text{SiFe}^{3+}_2\text{O}_{12}$) being a notable additional component
356 (Fig. 8B; [Table 4](#)), increasing with andradite content (Sch_{0-76}). Pyrope ($\text{Mg}_3\text{Al}_2\text{Si}_3\text{O}_{12}$) and almandine
357 ($\text{Fe}_3\text{Al}_2\text{Si}_3\text{O}_{12}$) end members combined are < 6 mol%.

358 Magmatic skarn xenolith garnets exhibit a wide compositional range ($\text{Grs}_{0-66}\text{Adr}_{24-75}\text{Sch}_{0-76}$). In zone R3b,
359 these garnets are compositionally distinct ($\text{Grs}_{60-66}\text{Adr}_{31-37}\text{Sch}_{1-2}$) from interstitial garnets within the
360 wollastonite core ($\text{Grs}_{0-66}\text{Adr}_{24-75}\text{Sch}_{1-76}$). The interstitial garnets, in close spatial association with calcite,
361 cuspidine, gehlenite and a wadalite-like phase (see below), have inclusions of this wadalite-like phase,
362 possibly a result of similarities between the crystal structure between hydrogarnet and wadalite-mayenite
363 (e.g. Glasser, 1995; Grew *et al.*, 2013). Garnets with 76 mol% schorlomite
364 [$\text{Ca}_{3.0}(\text{Ti}_{1.5}\text{Fe}^{2+}_{0.1}\text{Fe}^{3+}_{0.2}\text{Mg}_{0.1})(\text{Si}_{1.8}\text{Al}_{0.6}\text{Fe}^{3+}_{0.6})\text{O}_{12}$] are found as rims around titanite, in close association
365 with perovskite. Ti gradients are found across rare wadalite-like phase-bearing garnet crystals (Sch_{3-21}).

366 Exoskarn xenolith garnets have a more restricted compositional range ([Table 4](#)), limited to higher
367 grossular contents ($\text{Grs}_{73-97}\text{Adr}_{3-24}\text{Sch}_{0-2}$). The highest grossular contents, up to Grs_{97} are found
368 exclusively within exoskarn A type xenoliths, around residual calcite crystals and their spurrite \pm larnite-
369 rich reaction rims.

370 *Melilite*

371 Melilite is only found in non-trace quantities in exoskarn assemblage B xenoliths. Melilite compositions
372 are gehlenite-rich, closely following the gehlenite–åkermanite join, with < 8 mol% Na-melilite and < 10
373 mol% Fe-åkermanite ($\text{Gh}_{43-91}\text{Ak}_{2-45}\text{Na-Mel}_{0-8}$) (Fig. 8C; [Table 5](#)). In exoskarn type B xenoliths, melilite
374 has three textural forms: surrounding spinel, intergrown with CaTs-clinopyroxene, and locally texturally
375 equilibrated with 120° grain boundaries (Fig. 4C). Melilite in association with spinel is richer in gehlenite
376 (Gh_{68-83}) than the clinopyroxene intergrowths (Gh_{57-58}) and well equilibrated types (Gh_{47-50}).

377 *Sulphur and Halogen-bearing Phases*

378 Pyrrhotite is found in both magmatic and exoskarn xenoliths, often touching or rimmed by anhydrite. In
379 magmatic skarn xenoliths, pyrrhotite is found in zone R2, as accessory inclusions in wollastonite and

380 CaTs-clinopyroxene, and as rare inclusions in melt inclusions in the core. Fe/S ranges from 83 to 85%,
381 and Cu concentrations range from 0.06 to 0.59 wt%. Pyrrhotite is sometimes found with near
382 stoichiometric cubanite (Table 6). The associated anhydrite is pure, with < 0.04 wt% BaO and < 0.1 wt%
383 SrO.

384 Cupridine is found as crystals within calcite (magmatic skarn xenoliths) or forming within the reaction
385 rim around calcite (exoskarn xenoliths) associated with stoichiometric spurrite \pm larnite and an
386 unidentified Ca-Si-Al-O phase. Fluorine a.p.f.u. approach the ideal 2 (1.937-2.035) indicating negligible
387 OH. Fluorite is a fine grained (< 20 μ m) accessory phase replacing calcite in both xenolith types, and
388 evidently nucleated at crystal borders or forming fine halos around vesicles in calcite.

389 Apatite is found in magmatic skarn xenolith zone R4, and contains 0.7 to 0.8 wt% Cl and no detectable
390 SO₃. Ellestadite is found as an accessory phase in exoskarn xenoliths with 7.2 to 10.0 wt% SO₃ and 0.7 to
391 1.2 wt% Cl. F was not analysed with EMPA, however ~2 wt% F was identified using SEM-EDS,
392 indicating that OH is minimal. Stoichiometric ellestadite (undetectable P₂O₅) with ~1.9 wt% Cl was
393 determined with SEM-EDS coexisting with anhydrite in sample M13-02, within the reaction rim around
394 large remnant calcite crystals.

395 Qualitative EDS analyses have identified trace quantities of small (< 5 μ m) baryte crystals in both
396 magmatic and exoskarn xenoliths, and additionally a crystal of cotunnite (PbCl₂) is present in the
397 magmatic skarn xenoliths.

398 There are unidentified Cl-bearing minerals, which may possibly be new minerals. Skarn xenoliths, such
399 as those from the Upper Chegem caldera, Russia, can be host to numerous new minerals (e.g. Galuskin *et*
400 *al.*, 2013), and this may additionally be the case at Merapi. A wadalite-like Ca-Al-Fe-Si-Cl mineral
401 compositionally similar to the wadalite-eltyubyuite mayenite solid solution (when normalised to 26
402 cations) is found in association with calcite, cupridine, garnet and gehlenite in magmatic skarn xenolith
403 MX1 (Table 7). These crystals however have compositions with Si a.p.f.u. 4.6-5.5, higher than the ideal
404 Si 4, and lack sufficient Mg to balance this increase in Si in wadalite (*c.f.* Galuskin *et al.*, 2015). Raman
405 spectra of this phase are included as supplementary Fig. S4.

406 A Ca-Al-Si-Cl-F mineral is found in exoskarn xenoliths CS11 and M-XCS in the rim around areas where
407 larnite and spurrite have replaced calcite. Concentrations of Cl and F in this mineral have only been
408 determined by SEM-EDS, and as it contains 10 wt% more CaO than the wadalite-like mineral, and lower
409 volatile contents (~7 wt%) we believe it to be a different mineral.

410 *Oxides, Other Silicates, and Accessory Minerals*

411 The dominant Fe-Ti oxide in the magmatic skarn xenoliths is magnetite, with 0.3 to 11.5 wt% TiO₂.
412 Magnetite within the xenolith cores is distinct (< 0.3 wt% TiO₂) from magnetite in the other zones (8.9-

413 11.5 wt% TiO₂). Ilmenite is present in zone R2 of one xenolith. Qualitative EDS analysis has identified
414 micrometre sized chromite in the xenolith cores. Hematite is the dominant oxide found in the exoskarn
415 xenoliths, with rare magnetite present as well. Perovskite is found as a 50 µm vermicular cluster
416 intergrown with wollastonite and plagioclase in one magmatic skarn xenolith (sample MX1) and is
417 essentially stoichiometric CaTiO₃. A Ca-Zr-Ti-O mineral (calzirtite?) is found in the same magmatic
418 skarn xenolith. Titanite across all xenolith types contains 1.04 to 2.51 wt% Al₂O₃ and 0.73 to 2.86 wt%
419 FeO. An unidentified Ca-Al-Si-P mineral is found in exoskarn A samples CS11 and MXCS,
420 approximating the formula Si_{3.1}Ti_{0.1}Al_{2.9}Ca_{3.0}P_{0.9}O₁₆ when assuming 16 oxygens. Xenotime and monazite
421 are very rare calcite inclusions in exoskarn A xenoliths. Spinel (Sp₈₃₋₈₉Her₁₁₋₁₇) is found exclusively in the
422 gehlenite-garnet-CaTs clinopyroxene-spinel exoskarn B xenolith (MX99-3s). These mineral analyses are
423 given in Table 8.

424 **Glass Chemistry**

425 Melt inclusions and interstitial glass are almost entirely restricted to magmatic skarn xenoliths, with melt
426 inclusions and glass only found in the exoskarn xenoliths within the clinopyroxene-rich reaction rim at
427 the host lava contact. Xenolith interstitial (zones R1, R2, R4 and core) and melt inclusion (zones R1, R3,
428 R4 and core) glass compositions show strong deviation from lava groundmass glass and melt inclusion
429 compositions, and also show compositional differences between zones (Fig. 9; [Table 9](#)). Melt inclusions
430 are compositionally more diverse than the interstitial glass. CaO concentrations in interstitial glass and
431 melt inclusions from zone R1 and some R2 analyses overlap lava glass CaO values (0.2 to 3.8 wt%). CaO
432 concentrations in the interstitial glass (0.9-6.5 wt%) and in melt inclusions (0.5-11.3 wt%) within the
433 xenolith zones R3, R4 and the core are elevated by up to ~4 wt% in the interstitial glasses in relation to
434 magmatic values and by up to 10 wt% in the melt inclusions. These glasses, especially the melt
435 inclusions, are also characterised by low Al₂O₃ and K₂O relative to lava glasses (Fig. 9), and smaller
436 variations from the lavas are observed in all other major and minor elements. Al₂O₃ concentrations are up
437 to 5 wt% lower than in the lavas, and up to 2 wt% lower in K₂O. Xenolith glass volatile concentrations
438 are broadly comparable to the lava glasses, with only a few analyses exceeding that of the lavas. Sulphur
439 exceeds lava groundmass concentrations in some zone R1 and zone R4 analyses, containing up to 510
440 ppm sulphur. Chlorine is typically within lava groundmass glass concentrations, and only exceeds lava
441 glass values in plagioclase-hosted melt inclusions in sample CS16 and interstitial glasses in MX99-4s.
442 The few analyses for F (< 1110 ppm) show that concentrations are within the wider range of lava values
443 (< 2637 ppm). Although the melt inclusion analyses for MX1 show negligible F, localised patches of
444 cuspidine and fluorite have been observed.

445 **Fluid Inclusions**

446 Fluid inclusions in the magmatic skarn xenoliths ($n=28$) are two phase vapour-rich inclusions in
447 wollastonite. The dominant fluid composition is CO₂, confirmed by instantaneous melting at -57.3 to -
448 56.1°C. The slight deviation from ideal melting at -56.6°C indicates the presence of a small percentage
449 other dissolved gases such as SO₂, N₂, which are not thought to have a significant effect on pressure
450 estimates (Frezzotti *et al.*, 2002). No H₂O is observed either as ice or clathrate. Homogenisation is to the
451 vapour phase at 12.9 to 29.9°C. These temperatures correspond to densities of 0.15 to 0.35 g/cm³,
452 indicating trapping pressures of 33 to 92 MPa, when assuming a formation temperature of 850°C (see
453 discussion), utilising the Hansteen and Klügel (2008) spreadsheet implementation of Sterner and Pitzer
454 (1994) and Span and Wagner (1996) density and equation of state models. An extreme temperature
455 estimate increase to 1200°C only increases pressure estimates by ~30 MPa. No inclusions for barometry
456 with resolvable homogenisation were found in the exoskarn xenoliths, but CO₂ melting was observed in
457 some inclusions.

458 **DISCUSSION**

459 In this section we discuss the processes during formation of the xenoliths, and the pressure, temperature
460 and f_{O_2} conditions that can be determined from the recorded mineral assemblages. We also discuss the
461 implications for the magmatic system at Merapi, such as magmatic contamination by xenolith phases,
462 metal transport and the CO₂ output by decarbonation reactions. Accurate determination of temperature in
463 the magmatic skarn xenoliths requires accurate estimates of the melt composition during xenolith
464 formation; therefore we first discuss the implications for any modification of melt inclusion compositions.

465 **Post-entrapment Modification of Melt Inclusions**

466 The abundance of melt inclusions in the magmatic skarn xenoliths allows for constraining the original
467 composition of the melt present during xenolith formation, and, potentially, application of
468 thermobarometric models (discussed below). Post-entrapment modification of melt inclusion
469 compositions however is a well-documented phenomenon, occurring via diffusive exchange of elements,
470 crystallisation of a host mineral boundary layer, or from crystallisation of daughter crystals
471 (e.g. Nakamura and Shimakita, 1998; Danyushevsky *et al.*, 2000; Nielsen, 2011). Therefore, assessment
472 of these effects is required before interpreting the inclusion compositions. Melt inclusions are found
473 within clinopyroxene, plagioclase and wollastonite hosts in the magmatic skarn xenoliths, all of which
474 have no universally accepted way to back-calculate the original composition. The interstitial glass within
475 the xenoliths provides a first order constraint on the original melt composition, showing that it is strongly
476 elevated in CaO compared to lava glass compositions (Fig. 9). We have not attempted correction of our

477 melt inclusions, and consider the wollastonite-hosted melt inclusions to be the best estimates of melt CaO
478 concentrations for the following reasons.

479 Examples of correcting for inclusion modification in clinopyroxene hosts include adding the host
480 clinopyroxene to the inclusion (e.g. Hartley *et al.*, 2018) until Fe-Mg partitioning between the inclusion
481 and clinopyroxene (KD_{Fe-Mg}^{cpx-MI}) approaches the widely accepted equilibrium value of 0.28 ± 0.08 (Putirka,
482 2008), and adding calculated equilibrium clinopyroxene back to the melt inclusion until the calculated
483 clinopyroxene has the same Mg# as the host (e.g. Preece *et al.*, 2014). A compilation of magma-carbonate
484 (both limestone and dolomite) interaction experimental data shows that $KD_{Fe-Mg}^{cpx-melt}$ in carbonate-
485 contaminated systems may strongly diverge from the magmatic-derived 0.28 ± 0.08 (Putirka, 2008) (Fig.
486 10A), suggesting that $KD_{Fe-Mg}^{cpx-melt}$ is redox-sensitive (see oxybarometry discussion below) and an Fe-Mg
487 partitioning equilibrium-based correction is not appropriate.

488 The difference between observed and predicted clinopyroxene diopside-hedenbergite (DiHd) components
489 (Δ DiHd: Putirka, 1999, 2008; Mollo *et al.*, 2013; Neave and Putirka, 2017) is more accurate at predicting
490 equilibrium (Fig. 10B), with 68% of magma-carbonate experimental equilibrium clinopyroxene-melt
491 pairs predicted to fall within model error (± 0.07 ; Mollo *et al.*, 2013). Applied to the Merapi xenoliths,
492 clinopyroxene-hosted melt inclusions within zones R3 and R4 have irregular embayed forms, suggesting
493 some sidewall crystal growth, and Δ DiHd values > 0.07 , indicating some potential modification of
494 trapped melt compositions. Melt inclusion-clinopyroxene pairs from zones R1 and R2 have Δ DiHd values
495 from 0 to 0.14, with an average of 0.05, indicating some may represent unmodified melt values. These
496 compositions overlap lava glass compositions, consistent with their proximity to the lava contact,
497 indicating a magmatic character.

498 An example of plagioclase-hosted melt inclusion correction is regressing the magmatic liquid line of
499 descent in TiO_2 - Al_2O_3 space, and adding plagioclase back until the inclusions lie on the liquid line of
500 descent (Hartley *et al.*, 2018). This cannot be applied here as our measured xenolith melt inclusion
501 compositions, evidenced by elevated CaO in xenolith interstitial glass compositions, are contaminated and
502 are not closed system magmatic values (see below), and therefore cannot be assumed to lie on a
503 regression line through the magmatic liquid line of descent. Moreover, a micron thick rim of Ab-rich
504 plagioclase is observed around the inclusion walls (Fig. 3E, G) and suggests some modification of
505 plagioclase inclusion compositions occurred as well.

506 Wollastonite-hosted melt inclusions are generally well formed and equant with a single shrinkage bubble,
507 and lack textural evidence of sidewall crystallisation and modification (Fig. 3D). Although Fe and Mn are
508 weakly compatible in wollastonite, traverses from inclusion contact to 20 μ m into the crystal do not show

509 any resolvable chemical gradients that would indicate diffusion and melt inclusion alteration. Therefore,
510 wollastonite-hosted inclusions are likely the best inclusions to represent original compositions.

511 The effect of post-entrapment crystallisation of a melt inclusion can be tested graphically. Fractionation
512 vectors in Fig. 9 show the effect of 10% subtraction (crystallisation) of clinopyroxene, plagioclase and
513 wollastonite on glass compositions. Taking the fractionation vectors for the CaO vs SiO₂ plot, Fig. 9
514 shows that that any post-entrapment crystallisation of the respective host phase would lower the CaO
515 concentration of the trapped melt, therefore our analyses must reflect minimum original CaO estimates,
516 regardless of inclusion sidewall crystallisation. Melt inclusion compositions instead follow the vector for
517 addition of calcite to the published melt compositions. As the current methods of correcting for post
518 entrapment crystallisation are not suitable for these compositions, no attempt has been made to account
519 for the effects of melt inclusion modification. Additionally, these compositions overlap the compositions
520 of Ca-contaminated interstitial glasses, and high CaO is present regardless of the host mineral phase. This
521 shows that although post-entrapment modification may have occurred, the very high CaO values may
522 reasonably represent minimum estimates of original melt compositions.

523 **Intensive Variables**

524 *Magmatic Skarn Xenolith Thermobarometry*

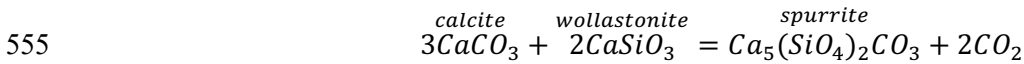
525 The abundance of glass and common mineral phases (clinopyroxene, plagioclase) allows for the
526 application of thermobarometric models to the xenoliths (Fig. 11). On the basis of the uncertainty in
527 mineral-melt equilibrium testing, and the results of testing thermobarometric models with experimental
528 carbonate assimilation data (see supplementary material), application of the glass-only equation 34 of
529 Putirka (2008) to the clinopyroxene-saturated interstitial glasses of the magmatic skarn xenoliths with
530 water contents estimated by difference from 100 wt% (Anderson, 1973, 1974; Devine *et al.*, 1995),
531 provides a temperature of $829 \pm 45^{\circ}\text{C}$ ($n=89$). Melt inclusions, in turn, reflect a slightly higher
532 temperature of $876 \pm 49^{\circ}\text{C}$ ($n=88$). These temperatures are consistent with the presence of ferrobustamite
533 overgrowths on the coexisting wollastonite, which is thought to be stable between $\sim 800\text{-}880^{\circ}\text{C}$ (Rutstein,
534 1971). A pressure of 50 MPa was assumed for thermometry, consistent with the results of fluid inclusion
535 barometry (our results: 34-92 MPa, and those of Clocchiatti *et al.* (1982): 67-109 MPa). Temperature
536 estimates are lowered by a negligible 5°C per 100 MPa. Temperatures estimated for glasses within any
537 lava attached to the xenolith, and lava interstitial glasses from the literature (with an assumed pressure of
538 200 MPa; *c.f.* Preece *et al.*, 2014; Erdmann *et al.*, 2016) are higher than that of the xenolith glasses, at 937
539 $\pm 43^{\circ}\text{C}$. Phase equilibria estimates of pre-eruptive temperatures for Merapi are $925\text{-}950^{\circ}\text{C}$ (Erdmann *et*
540 *al.*, 2016), which supports the higher lava glass temperature from our glass thermometry.

541 Additional constraints can be gained from comparison with experimental phase equilibria. The small
542 interstitial patches of garnet, plagioclase and wollastonite in sample MX1 are stable between $\sim 510\text{-}890^{\circ}\text{C}$,

543 with an $X_{CO_2} < 0.6$ at 100 to 200 MPa (Gordon and Greenwood, 1971; Tracy and Frost, 1991), consistent
 544 with temperatures from the glass thermometry. The R3b zone in sample MX1, comprising coexisting
 545 grossular-andradite garnet ($Adr_{0.3}$) and CaTs-clinopyroxene ($CaTs_{0.23}$) indicates temperatures of 900-
 546 950°C based on experimental phase equilibria (Huckenholz *et al.*, 1974; Gustafson, 1974).

547 *Exoskarn T-XCO₂*

548 Although the exoskarn xenoliths lack glass, many phases and assemblages in the exoskarn xenoliths can
 549 help constrain temperatures by comparison with experimental data and thermodynamic modelling.
 550 Spurrite + cuspidine ± larnite-bearing reaction rims between calcite and wollastonite + grossular +
 551 anorthite in samples CS11 and MXCS-0 allow temperature constraints, while additionally demonstrating
 552 the progressive interaction along a CaO-SiO₂-CO₂ system (e.g. Zharikov, 1969). The presence of spurrite
 553 and absence of evidence for lower temperature tilleyite-forming reactions indicate spurrite formation by
 554 either interaction between wollastonite and calcite

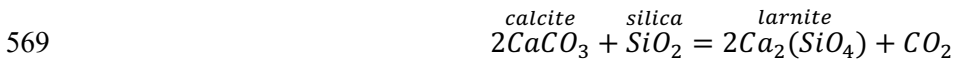
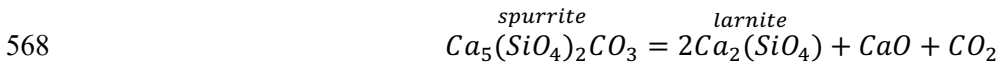
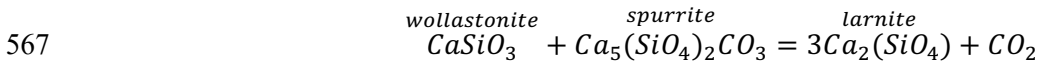


556 or calcite directly with SiO₂



558 The former reaction indicates temperatures of ~700-1000°C (Tuttle and Harker, 1957). Spurrite is stable
 559 as low as 430°C at low CO₂ partial pressure (Henmi and Henmi, 1978), but the proximity of tens of
 560 microns to a decarbonating calcite crystal and a significant proportion of voids suggests a high CO₂
 561 partial pressure. The latter reaction occurs at 910°C at 1 atm when in the presence of chlorine or fluorine
 562 (Bolio-Arceo and Glasser, 1990). Cuspidine and fluorite are found within tens of microns of the spurrite,
 563 confirming a reaction occurred with a fluorine-bearing fluid.

564 Larnite forms further from the calcite near the wollastonite contact (Deegan *et al.*, 2010 Fig. 10b) in
 565 sample MXCS-0, indicating temperatures of > 850°C (Wyllie and Haas Jr, 1965; Joesten, 1974; Treiman
 566 and Essene, 1983), following the potential reactions:



570 The dominant mineral assemblage in these large calcite-bearing xenoliths can be described in the SiO₂-
571 Al₂O₃-CaO system, comprising grossular garnet (Grs₇₈₋₉₆), wollastonite and anorthite. This assemblage is
572 stable between ~510-890°C at 50-200 MPa, with an increasingly restricted XCO₂ with pressure, varying
573 from > ~0.2 to 1 at 50 MPa, and from ~0.2 to 0.4 at 200 MPa (Gordon and Greenwood, 1971; Tracy and
574 Frost, 1991). Grossular with inclusions of calcite, wollastonite and anorthite is additionally found in the
575 CaTs-clinopyroxene bearing xenoliths, suggesting the following reaction has occurred:



577 The equilibration temperature of CaTs-clinopyroxene and grossular-andradite-bearing exoskarn xenoliths
578 is estimated as 900-950°C based on experimental data (Huckenholz *et al.*, 1974). Reactions involving
579 these phases were further investigated using Theriak-Domino software (build date 3-1-2012, de Capitani
580 and Petrakakis, 2010) using calculated whole-rock compositions in the system Si-Al-Fe-Mg-Ca-C. An
581 upper limit of temperature for the exoskarn xenoliths is ~910°C at 100 MPa, which represents the limit of
582 garnet stability (Fig. 12). Garnet reacts out just after melilite becomes stable at ~900°C. Exoskarn type A
583 xenoliths contain abundant garnet and trace amounts of gehlenite, constraining the temperature to this
584 narrow field between 900 and 910°C. The calculated high (30 mol%) CaTs contents at the melilite-in
585 boundary are in agreement with the high (up to 38 mol%) CaTs contents observed in these xenoliths, as
586 are modelled gehlenite contents (> 70 mol%) compared to the observed ones (74-94 mol%). The mineral
587 assemblage of the exoskarn type B xenolith is constrained by a slightly lower maximum temperature as
588 garnet becomes unstable at 860°C (Fig. (12). A minimum temperature estimate is given as ~780°C from
589 high clinopyroxene CaTs component (22-39 mol%). Conditions are further constrained to *a*_{CO₂} < 0.5 for
590 both xenolith types by the absence of meionite and calcite. The results closely match the temperatures
591 from previously cited experimental studies. These temperature estimates are similar to those estimated for
592 the magmatic skarn xenoliths by thermobarometry.

593 In summary, the comparison with experimental studies and results from modelling indicate exoskarn
594 formation temperatures up to ~910°C, with a lower limit at around 780°C for xenoliths with CaTs
595 clinopyroxene and 510°C for xenoliths without CaTs clinopyroxene. There is no evidence for low
596 temperature retrograde overprint, and these temperatures overlap the temperatures estimates for the
597 magmatic skarn xenoliths (~850°C). These temperature estimates extending to as low as 510°C,
598 combined with the petrological differences described above, indicate a metasomatic origin for the
599 exoskarn xenoliths instead of petrogenesis via magmatic crystallisation for the magmatic skarn/endoskarn
600 xenoliths.

601 *Oxygen Fugacity*

602 Estimates of oxygen fugacity (fO_2) are difficult due to the lack of mineral assemblages commonly used to
603 determine this variable. A first order estimate is obtained from the presence of magnetite in magmatic
604 skarn xenoliths compared to hematite in the exoskarn xenoliths, indicating more oxidising conditions in
605 the latter. Two single crystal clinopyroxene oxybarometers exist that use Fe^{3+} concentrations in
606 clinopyroxene to estimate oxygen fugacity (Cortés *et al.*, 2006; Simakin *et al.*, 2012). Although Fe^{3+}
607 concentrations in clinopyroxenes calculated by stoichiometry (e.g. Lindsley, 1983; Droop, 1987) have
608 been shown in some studies to have a weak correlation to measured clinopyroxene Fe^{3+} concentrations
609 (e.g. Sobolev *et al.*, 1999), a positive correlation between clinopyroxene Fe^{3+}/Fe_{total} and fO_2 has been
610 demonstrated from experimental data by Cortés *et al.* (2006) and Simakin *et al.* (2012). When taking a
611 much larger dataset (the Library of Experimental Phase Relations, Hirschmann *et al.*, 2008), with high
612 fO_2 experiments such as those from Mollo and Vona (2014) and Sugawara (2001) and normalise the data
613 to the NNO (nickel-nickel oxide) buffer (*c.f.* Cortés *et al.* 2006) using buffer equations from Frost (1991),
614 then a broad positive correlation is still observed, although with a large scatter ($R^2=0.44$). Fe^{3+}/Fe_{total} falls
615 short of unity at an fO_2 of air, and all Fe is Fe^{2+} at $\sim\Delta NNO-2$. When applied to this large experimental
616 dataset, the oxybarometer of Cortés *et al.* (2006) strongly overestimates fO_2 conditions, whilst Simakin *et al.*
617 *et al.* (2012) fails to recover experiments performed in air (Fig. 13).

618 We use a selection of data from experiments that span a wide fO_2 range to calibrate a new oxybarometer
619 that recovers high fO_2 conditions more accurately. We use the datasets of Whitaker *et al.* (2007), Freise *et al.*
620 *et al.* (2009), Feig *et al.* (2006), Feig *et al.* (2010), and Mollo and Vona (2014) (excluding Mollo and
621 Vona's relatively high Fe^{3+}/Fe_{total} NNO experiments). This calibration dataset spans a fO_2 between
622 $\Delta NNO-5$ to air, temperatures between 900 to 1280°C, 0 to 5 wt% H_2O , and 50-68 wt% SiO_2 and has a
623 high coefficient of determination ($R^2 = 0.80$). Although the dataset of Sugawara (2001) spans the widest
624 fO_2 range known to the authors (~ 13 log units), calculated Fe^3/Fe_{total} values have larger scatter than those
625 from other datasets, therefore we exclude these from the regression. Additionally, although Al^{IV} increases
626 in clinopyroxene with increasing fO_2 (e.g. Mollo and Vona, 2014), adding Al^{IV} to the models shows no
627 significant improvement on the model, therefore we only use Fe^3/Fe_{total} for prediction. There is also no
628 significant improvement in R^2 or the standard error when using a polynomial fit over a linear model,
629 however we use a polynomial fit to marginally improve the estimates at low fO_2 , as was shown by
630 Simakin *et al.* (2012). We additionally considered constructing a similar oxybarometer based on Fe^{3+} in
631 garnet as Fe^{3+} can be estimated accurately for garnet (Arai, 2010), however there is an insufficient range
632 of oxygen fugacity controlled experiments in the Library of Experimental Phase Relations (LEPR;
633 Hirschmann *et al.*, 2008) database to attempt building a similar single crystal oxybarometer for garnet.

634 For testing, we filtered the entire experimental database to clinopyroxenes equilibrated < 1 GPa, with Si
635 a.p.f.u. < 2 , Ca > 0.5 a.p.f.u., cation totals between 3.98 and 4.1, and $Na_2O < 1$ wt%. Our models recover

636 the calibration dataset with a residual standard error of 1.5 log units, the global database and additional
637 experimental data to 1.8 log units, compared to 2.1 for Cortés *et al.* (2006) and Simakín *et al.* (2012). The
638 improvements in the error are small, in part due to a lack of high fO_2 experiments and potential variable
639 data quality of the individual experiments in the LEPR database. However, the accuracy at high fO_2 is
640 improved, which is most relevant to our Merapi xenoliths. We obtain the following equation:

$$641 \quad \Delta NNO = 22.705 \left(\frac{Fe^{3+}}{\sum Fe} \right)^3 - 32.400 \left(\frac{Fe^{3+}}{\sum Fe} \right)^2 + 21.799 \left(\frac{Fe^{3+}}{\sum Fe} \right) - 3.066$$

642 where Fe^{3+} and $\sum Fe$ are Fe a.p.f.u. estimated from stoichiometry (e.g. Lindsley, 1983; Droop, 1987),
643 and ΔNNO is the deviation from the nickel - nickel oxide oxygen fugacity buffer in log units.

644 Application of our oxybarometric model shows a wide spread of fO_2 values for the xenoliths (Fig. 14A).
645 Magmatic skarn xenolith clinopyroxenes at the lava contact zone R1 and in zones R2, R3 and R4, have
646 values similar to the magmatic values both predicted by our model and published estimates (ΔNNO -0.2 to
647 +1.6 Gertisser, 2001; Erdmann *et al.*, 2014). Touching pyrrhotite and anhydrite crystals in zone R2 in a
648 small subset of magmatic skarn xenolith samples additionally indicate a near-magmatic fO_2 range
649 between ΔNNO +0.5 to +2.5 (Luhr, 2008; Parat *et al.*, 2011), consistent with other estimates. The R3b
650 zone in sample MX1 records higher oxygen fugacity conditions than the CaTs clinopyroxene + garnet
651 absent samples, at $\Delta NNO > +5$. Xenolith core clinopyroxenes are formed through a large range of oxygen
652 fugacity conditions. The higher values come from the CaTs-rich clinopyroxene cores of sample CS16
653 (Fig. 14B). Anhydrite crystals within these clinopyroxene cores (stable at $> \Delta NNO$ +1 Carroll and
654 Rutherford, 1987) provide further evidence for a relatively high fO_2 during early clinopyroxene
655 formation. Exoskarn xenolith clinopyroxene indicates formation under higher fO_2 than magmatic skarn
656 xenoliths, approaching that of air ($\sim \Delta NNO + 8$). While exoskarn type A xenoliths record a large range
657 from $NNO -1$ to +8, the exoskarn type B xenolith uniquely records conditions of exclusively $> \Delta NNO +$
658 5. The high fO_2 conditions recorded in the exoskarns are similar to that recorded in zone R3b of magmatic
659 skarn xenolith MX1.

660 High fO_2 in skarn systems is a result of CO_2 release from carbonate, and this CO_2 can impose a fO_2 equal
661 to or greater than the HM buffer (e.g. Nicholls, 1971; Wenzel *et al.*, 2002). The magnitude of fO_2 increase
662 is proportional to the freedom CO_2 has to leave the system. An open system continuous flux of CO_2
663 increases fO_2 higher than that of a closed system (Ganino *et al.*, 2008). The generally higher fO_2 observed
664 in the exoskarn xenoliths may thus be a result of prolonged open system flux of CO_2 , whereas the syn-
665 magmatic magmatic skarn xenoliths were rapidly processed within the magma. Magmatic skarn xenolith
666 zone R3b however records a high fO_2 , comparable to the exoskarns, and additionally mineral phases in
667 there, such as clinopyroxene, compositionally overlap exoskarn mineral compositions (Fig. 7). These
668 compositions may be in part due to a lack of melt in this region of the magmatic skarn xenolith, restricting

669 SiO₂ availability, and producing as a result silica-undersaturated mineral compositions such as CaTs
670 clinopyroxene.

671 **Xenolith Petrogenesis**

672 *Protolith*

673 An absence of Mg-rich skarn minerals within the xenoliths (olivine, periclase, merwenite, åkermanite)
674 and the abundance of wollastonite instead suggests a calcite-limestone protolith for the xenoliths. The
675 Merapi xenoliths do not match any mineral assemblages produced during magma-dolomite interaction
676 experiments, instead they closely resemble the results of magma-limestone experiments (e.g. Zarayskiy *et*
677 *al.*, 1987: wollastonite, clinopyroxene, garnet). Electron microprobe analyses of calcites (Whitley *et al.*,
678 2019) are pure calcites with < 0.2 wt% MgO + FeO + SrO, which additionally indicates a pure limestone
679 protolith in the absence of Mg-rich skarn minerals. Furthermore, local carbonate sampled from
680 Parangtritis (50 km south of Merapi) is limestone. The progressive chemical zonation within the xenoliths
681 from “magmatic” to calcic compositions (Fig. 5) shows that the Mg-Fe-Al-bearing phases source these
682 elements from the host magma, not from a dolomite or marl.

683 *Magmatic Skarn Xenoliths*

684 The abundance of Ca-rich melt inclusions and Ca-rich groundmass glass (Fig. 3) indicate crystallisation
685 of the main skarn mineralogy of clinopyroxene, plagioclase and wollastonite from a Ca-contaminated
686 magmatic melt, produced from dissolution of the carbonate protolith (Fig. 9) (*c.f.* Deegan *et al.*, 2010).
687 Calcic melt inclusions and matrix glasses were also described from volcanic products of the 2010
688 eruption of Merapi (Borisova *et al.*, 2013). Thermodynamic modelling suggests formation of Ca-rich
689 melts via a peritectic reaction of grossular-bearing calc-silicate material with the magma (Borisova *et al.*,
690 2016). The Ca-rich melt inclusions are spread randomly throughout their host crystals, or less commonly,
691 along crystal growth zones, showing a primary origin (Roedder, 1984; Goldstein, 2003). Clinopyroxene
692 compositions in these xenoliths are compositionally distinct from those in the exoskarn xenoliths, most
693 notably those from the glass zone R4 (Fig. 7), supporting formation from the Ca-rich melt instead of an
694 origin as incorporated xenocrysts from partially melted exoskarns. Fe-rich ferro-bustamite growths on
695 some wollastonite crystals is also consistent with crystallisation from this melt, as the glass and core
696 zones are characterised by FeO-enrichment (Figs. 6, 7). Melt inclusions in wollastonite are not
697 exclusively comprising CaO and SiO₂, but also contain other major element oxides such as K₂O, which
698 can only be derived from the magmatic melt as there no K-bearing phases found in any of the xenoliths
699 studied. The composition of these melt inclusions cannot be explained by dissolution of wollastonite but
700 supports the idea that wollastonite crystallized from a Ca-enriched melt. Experimental work at Merapi has
701 shown the contaminated melt takes up Sr and B from the carbonate protolith (Deegan *et al.*, 2010; 2016a),
702 which supports the idea of dynamic element exchange between carbonate and the surrounding melt. The

703 arrows in Fig. 9 show the addition of 10% CaO to the melt, indicating that the melt inclusions record
704 crystallisation from a melt with up to 20% CaO added. The groundmass glasses retain evidence for up to
705 10% added CaO, after crystallisation of wollastonite and other minerals. Although whole-rock
706 compositions at Merapi are basaltic to basaltic-andesite, the lava groundmass glasses, the melt
707 compositions in contact with the carbonate, and xenolith glasses, are distinctly more felsic (60-76 wt%
708 SiO₂). The melt inclusion CaO concentrations observed in our study (Fig. 9) far exceed (up to 11.3 wt%
709 CaO) those observed in glasses from calcite-saturated dacite-carbonate experiments of Carter and
710 Dasgupta (2016) (< 4.3 wt%), confirming their hypothesis that natural systems may be able to assimilate
711 more carbonate than their closed system experiments indicated.

712 Skarn minerals that contain melt inclusions and show evidence for crystallisation from a carbonate
713 contaminated magmatic melt, instead of through metasomatic transfer, are a rare but increasingly
714 recognised phenomenon (e.g. Fulignati *et al.*, 2001; Bin and Jin-song, 2016). Homogenisation
715 temperatures of these melt inclusions in the literature (Fulignati *et al.*, 2001; Bin and Jin-song, 2016)
716 indicate temperatures of 860-1200°C, which are in excess of those typically experienced during
717 metasomatic skarn formation in contact metamorphic aureoles (< c. 800°C; Meinert, 1992), indicating
718 direct interaction between a magmatic melt and carbonate. Trapping of melt inclusions in skarn minerals
719 precipitated from a calcite contaminated quartz diorite melt has been experimentally confirmed (Bin and
720 Jin-song, 2016), and dacite-carbonate interaction experiments (Carter and Dasgupta, 2016) have been
721 shown to crystallise wollastonite, in contrast to producing dominantly Ca-rich melt in experiments with
722 mafic melt compositions (Deegan *et al.*, 2010; Carter and Dasgupta, 2015).

723 As well as this rare and unique evidence for skarn mineral formation from carbonate contaminated melts,
724 and therefore exoskarn formation by this process, the magmatic skarn xenoliths also provide insights into
725 the morphology and cumulate-forming processes at the wall-rock contact at Merapi. Carbonate
726 assimilation has been shown to form and/or influence the mineralogy of cumulate assemblages; for
727 example, changes to the mineral chemistry of dunites at the Ioko-Dovyren Intrusion, Russia (Wenzel *et al.*,
728 2002), formation of clinopyroxenite xenoliths at Nisyros, Greece (Spandler *et al.*, 2012), and
729 olivine+clinopyroxene+spinel cumulate xenoliths at Colli Albani (Gaeta *et al.*, 2009; Di Rocco *et al.*,
730 2012). Reaction between carbonate and magmatic melt increases the stability of clinopyroxene and in
731 more evolved melts, plagioclase also (e.g. Mollo *et al.*, 2010). This results in a wallrock grading from a
732 cumulate zone adjacent to the magma body (endoskarn), to skarn assemblages at the limestone contact
733 (exoskarn). Skarn-derived Ca-rich melts are inferred (Wenzel *et al.*, 2002; Gaeta *et al.*, 2009) to be the
734 main source of carbonate components contaminating the magmatic melt. Our magmatic skarn xenoliths
735 are perfect examples of these processes. Zones R1 to R3 comprise the cumulate zone formed under the
736 influence of carbonate assimilation. Similar to cumulates at Ioko-Dovyren (Wenzel *et al.*, 2002) and Colli
737 Albani (Gaeta *et al.*, 2009), clinopyroxenes and plagioclase in these zones only show relatively subtle

738 variations in mineral chemistry from magmatic-derived mineral compositions that reveal their carbonate
739 contamination origin. The CaO-enriched glass-rich zone R4 captures the carbonate process of the
740 magmatic melt contamination, and the xenolith cores in some samples preserve very rare instances of the
741 actual calcite carbonate melt (see Whitley *et al.*, 2019). This carbonate melt has since only been inferred
742 to occur during other instances of carbonate assimilation (Wenzel *et al.*, 2002; Barnes *et al.*, 2005; Gaeta
743 *et al.*, 2009), whilst the magmatic skarns at Merapi preserve and demonstrate direct evidence for its
744 existence.

745 A syn-magmatic origin for these xenoliths, i.e. formation by direct magma-carbonate contact during
746 magmatic events such as eruptive periods, is consistent with the presence of glass and additionally the
747 low pressures of 37-93 MPa (corresponding to < 3.5 km) estimated from fluid inclusion barometry. These
748 pressures are similar to some pressure estimates derived from re-equilibrated melt inclusions in magmatic
749 clinopyroxenes at Merapi (Nadeau *et al.*, 2013b; Preece *et al.*, 2014), and they are lower than pressures
750 estimated for the main pre-eruptive magma chamber or reservoir at Merapi (100-400 MPa, corresponding
751 to depths of ~4-15 km; Commer *et al.*, 2006; Chadwick *et al.*, 2013; Costa *et al.*, 2013; Preece *et al.*,
752 2014; Erdmann *et al.*, 2016; Deegan *et al.*, 2016b). This indicates that the fluid inclusions have re-
753 equilibrated during ascent, or have been formed at very shallow crustal pressures. The lack of a 're-
754 equilibration tail' (Hansteen and Klügel 2008) and no evidence for pressures > 100 MPa in our fluid
755 inclusion dataset suggest re-equilibration is unlikely, and instead is indicative of fluid inclusion formation
756 in small ephemeral pre-eruptive reservoirs or during magmatic ascent during eruptive periods.

757 Patchy zoned clinopyroxenes with prominent irregular resorption surfaces (Fig. 7) show that this syn-
758 magmatic carbonate interaction is a dynamic process, under temporarily variable imposed oxygen
759 fugacity conditions caused by rapid CO₂ release (Fig. 14) (*c.f.* Mollo *et al.*, 2010). Variations in the ability
760 of this CO₂ to migrate from the reaction site (Ganino *et al.*, 2008; Blythe *et al.*, 2015) may cause the
761 variation in oxygen fugacity across texturally similar samples, and even within xenolith zones. Al, Fe³⁺-
762 rich clinopyroxene cores and andraditic-rich garnet indicate high initial oxygen fugacity conditions (Figs.
763 7, 14; Meinert, 2005; Mollo and Vona, 2014), whilst diopside-rich cores indicate high initial carbonate-
764 derived Ca activity in the melt (Zarayskiy *et al.*, 1987). Increasing CO₂ release causes clinopyroxene Fe-
765 enrichment in the mantle and rims (Zarayskiy *et al.*, 1987) to higher than observed in magmatic
766 clinopyroxenes in later stages of xenolith formation (Fig. 7). Fe is additionally concentrated in plagioclase
767 as An concentrations decrease (Fig. 6).

768 Although we propose that the magmatic skarn xenoliths reflect crystallisation from a Ca-contaminated
769 melt, it is interesting to note that their mineralogical zonation still bears strong resemblance to contact
770 metamorphic zoned bimetasomatic skarns and experimental reconstructions of these, such as produced
771 during granodiorite-calcite interaction experiments (Zarayskiy *et al.*, 1987). Magmatic skarn xenolith

772 samples with a garnet + CaTs clinopyroxene zone (zone R3b in Fig. 1) represent the exo/endoskarn
773 transition in natural skarns, where carbonate-derived elements are transferred to the magmatic system
774 (clinopyroxene + plagioclase endoskarns, zones R1-R3). In turn, certain magma-derived elements are
775 transferred to the carbonate protolith forming garnet + wollastonite + Di-Hd/CaTs clinopyroxene
776 exoskarns (zone R3b and the xenolith cores), reflected also in the chemistry of the individual zones (Fig.
777 5).

778 Dissolution of carbonate in high temperature mafic magmatic melts has been experimentally confirmed to
779 operate on the order of hours (Deegan *et al.*, 2010; Jolis *et al.*, 2013), but mineral equilibration is slower
780 (*c.f.* Carter and Dasgupta, 2016). First order constraints on the timescales of carbonate interaction at
781 Merapi can be tentatively placed using the growth rate of xenolith mineral phases such as clinopyroxenes.
782 Experimental and measured growth rates for euhedral clinopyroxenes in basaltic to andesitic magmatic
783 systems are on the order of 10^9 to 10^7 cm/s (e.g. Kouchi *et al.*, 1983; Simakin *et al.*, 2003; Orlando *et al.*,
784 2008; Kilgour *et al.*, 2014). Assuming similar growth rates for the clinopyroxenes in the xenoliths, a
785 typical 300 μ m clinopyroxene in zone R4, which has an entirely different composition to the Merapi
786 magmatic clinopyroxenes (Fig. 7) and therefore formed uniquely during magma-carbonate interaction,
787 could have formed in 3.5 to 347 days. Measurements of the growth rate of skarn formation between
788 granodiorite and calcite, and quartz and brucite marble, in experiments of Zarayskiy *et al.* (1987) indicate
789 similar timescales. Although clinopyroxene growth rates are poorly constrained, especially in magma-
790 carbonate systems, it is conceivable that the xenoliths could have formed on shorter timescales, e.g. in the
791 lead up to and during eruptive periods. The associated CO₂ release may then be able to influence eruption
792 dynamics (*c.f.* Troll *et al.*, 2012). Future work utilising diffusive timescales would potentially increase the
793 accuracy of these timescale estimates and aid hazard assessment at Merapi.

794 In summary, we propose that the magmatic skarn xenoliths are syn-magmatic in origin, forming as a
795 result of limestone dissolution into a magmatic melt, from which skarn minerals precipitate (Fig. 15).
796 Localised changes in oxygen fugacity caused by the CO₂ released to the fluid phase influenced the
797 composition of the minerals formed. Variable transfer of Ca from limestone, and magma-derived
798 elements, form zonations similar to those observed in metasomatic skarns, but at above solidus
799 temperatures. The composition of the zones is controlled by element transfer between magma and
800 limestone and the stability and abundance of the major minerals that form in the respective zones. Our
801 evidence of syn-magmatic magma-carbonate interaction is in agreement with previous studies on Merapi
802 magma-carbonate interaction (Deegan *et al.*, 2010, 2016a; Troll *et al.*, 2012), at Vesuvius (Blythe *et al.*,
803 2015; Jolis *et al.*, 2015) and at Colli Albani (Iacono-Marziano *et al.*, 2007; Freda *et al.*, 2011), which all
804 note the likely very rapid, syn-eruptive timescales of carbonate dissolution and CO₂ liberation. If correct,
805 this process has the potential to enhance eruption explosivity due to external CO₂ additions.

806 *Exoskarn Xenoliths*

807 Exoskarn xenoliths contain dominantly Al+Si+Ca-bearing phases, and < 10 wt% FeO+MgO based on
808 calculated whole rock compositions. Although the high Al could be indicative of a marl protolith, we
809 believe these samples come from a calcite-bearing protolith with input from magmatically derived
810 elements, on the basis of calcite oxygen isotopes showing evidence of interaction with magmatic fluids
811 (Whitley *et al.*, 2019), and the presence of F-Cl-S-rich phases most likely derived from magmatic
812 volatiles.

813 The exoskarn xenoliths lack the interstitial glass, melt inclusions and mineralogical zonation of the
814 magmatic skarn xenoliths, with only a clinopyroxene \pm plagioclase reaction rim at the lava contact. Melt
815 inclusion compositions within these rim clinopyroxenes are indistinguishable from the lava groundmass
816 glasses (Fig. 9). The core assemblage (garnet + CaTs clinopyroxene + wollastonite + anorthite \pm
817 gehlenite) is distinct from the magmatic skarn xenoliths (wollastonite \pm glass \pm DiHd clinopyroxene \pm
818 garnet \pm anorthite). The much higher fO_2 conditions recorded in the clinopyroxenes (Fig. 14) indicate that
819 these xenoliths experienced a longer period of CO₂ flushing than the magmatic skarn xenoliths (*c.f.*
820 Ganino *et al.*, 2008). This, coupled with the distinct mineralogy, a lack of glass and a lack of
821 mineralogical zonation, suggests that the exoskarn xenoliths originate from a contact metamorphic
822 aureole (exoskarn) around the upper crustal Merapi magma reservoir system (Fig. 15). The dominance of
823 high temperature anhydrous mineral assemblages indicates that they are sourced proximal to the magma
824 reservoir. Contact metamorphic aureoles can be extensive in size (Aarnes *et al.*, 2010), therefore we
825 expect low-temperature distal skarn assemblages to be present at Merapi, but these may not have been
826 frequently sampled during this study, possibly because of the high temperature 'skarn shell' (*c.f.* Fulignati
827 *et al.*, 2001; Jolis *et al.*, 2015) being overrepresented in our dataset.

828 The presence of spinel, as observed in one of our samples (MX99-3s), has been noted in several case
829 studies on magma-carbonate interaction (e.g. Wenzel *et al.*, 2002; Gaeta *et al.*, 2009; Spandler *et al.*,
830 2012). For instance, hercynitic spinel is widespread in skarns from the Italian volcanic provinces. Skarns
831 from the Colli Albani Volcanic District (Italy) contain Al-rich spinel in textural equilibrium with glass,
832 which was interpreted to reflect melting of calcite and mixing of this melt with the host magma (Gaeta *et*
833 *al.*, 2009). Metasomatic development through leaching was invoked to explain the occurrence of banded
834 forsterite-spinel skarns in ejecta from the 1631 Vesuvius eruption (Pascal *et al.*, 2009). Experimental
835 work on magma-carbonate interaction with andesitic (Carter and Dasgupta, 2016) and basanitic (Conte *et*
836 *al.*, 2009) magmas also produced aluminous spinel. Clearly, the presence of aluminous spinel is a
837 common characteristic of carbonate assimilation. None of these studies, however, shows the unique
838 texture and association with gehlenite as in sample MX99-3s, and we classify this sample as exoskarn
839 (type B) based on the lack of glass and the mineralogical differences to the more common magmatic
840 skarns at Merapi.

842 **Volatiles and Metal Transport**

843 The numerous F-Cl-S phases identified in the xenoliths record evidence of interaction with a magmatic-
844 derived volatile phase (MVP; *c.f.* Nadeau *et al.*, 2010; Preece *et al.*, 2014) during formation of the
845 xenoliths. Although F-Cl-S-bearing phases indicate the presence of an aqueous fluid, there is no clear
846 evidence of the role of H₂O during xenolith formation. Silicate magma has a limited capacity to dissolve
847 the excess liberated crustal-derived CO₂ and any increase in melt CO₂ would strongly reduce the
848 solubility of H₂O (e.g. Tamic *et al.*, 2001), increasing the free H₂O available during magma-carbonate
849 interaction. The xenoliths however contain anhydrous mineral assemblages, and fluid inclusions are two
850 phase liquid CO₂ + vapour CO₂ with only very rare small fluid inclusions containing unidentified
851 daughter crystals. Excess CO₂ in the magma causes the typical wollastonite-forming reaction $\text{SiO}_2 +$
852 $\text{CaCO}_3 \rightarrow \text{CaSiO}_3 + \text{CO}_2$ to favour the reactants and promote skarn mineral formation.

853 F-Cl-S-bearing phases are found within both magmatic and exoskarn xenoliths, however they are not
854 found in every magmatic skarn xenolith sample. In the magmatic skarn xenoliths, they are found in zone
855 R2 (anhydrite surrounding pyrrhotite ± cubanite), zone R3b (ellestadite) and as interstitial patches the
856 wollastonite-dominant cores. These patches contain cuspidine, fluorite and the wadalite-like mineral,
857 whilst anhydrite, apatite, and cotunnite (PbCl₂) are found as accessory phases elsewhere in the cores.
858 Pyrrhotite, cubanite, Fe-oxides and apatite are sometimes found as daughter crystals in melt inclusions.
859 The presence of fluorine-bearing phases in sample MX1 is closely related to calcite with a melt-like
860 texture, consistent with fluorine lowering the melting temperature of calcite (Jago and Gittins, 1991;
861 Gorzkowska *et al.*, 1988a, 1988b; see Whitley *et al.*, 2019 for more detail). Chlorine and limited data for
862 F in the Ca-rich xenolith core interstitial glass and melt inclusions do not show elevated concentrations
863 compared to the lavas. This suggests that the volatile-rich minerals are unlikely to have precipitated
864 directly from the melt, like the wollastonite, clinopyroxene and plagioclase, but are instead the result of
865 interaction with this magmatic-derived volatile phase. In sample MX1, the melt-like calcite is in places
866 replaced by the wadalite-like mineral, which retains the calcite texture (Fig. 3). Instances where garnet is
867 replaced by this wadalite-like phase may be from reaction with magmatic HCl (e.g. Fujita *et al.*, 2001).
868 Calcite additionally reacts with fluorine to form fluorite as distinct crystal phases, and as radial growths
869 around a vesicle touching calcite (Fig. 3A-B), suggesting fluorine is an important component of the
870 volatile phase.

871 The exoskarn xenoliths additionally contain phases enriched in magmatic-derived volatiles. For instance,
872 ellestadite is found throughout the xenoliths, and rare pyrrhotite and anhydrite are present in some
873 samples, but the majority of volatile-rich phases (cuspidine, anhydrite, ellestadite, fluorite, spurrite) are
874 concentrated in the reaction rims around residual large calcite crystals. A magmatic fluid source for these

875 mineral phases is evidenced by calcite oxygen isotopic shifts towards magmatic values (Whitley *et al.*,
876 2019) and elevated trace element LREE/HREE in these calcites compared to marine limestone
877 (Supplementary Fig. S5; Supplementary Table S1).

878 The presence of the magmatic-derived volatile phase within the xenoliths indicates potential for economic
879 metal mineralisation beneath Merapi and similar carbonate-hosted arc volcanoes in the region. Oxidised
880 silicic calc-alkaline arc intrusions are frequently associated with porphyry Cu, Zn, Pb and Fe deposits
881 (Meinert, 2005). Ubiquitous calc-silicate xenoliths at Merapi provide evidence for skarn formation, and
882 garnet and clinopyroxene compositions in these xenoliths overlap those characteristic of Cu, Zn and Fe
883 skarns (Meinert, 1992). Although these economic metals are rare in our studied xenoliths, our data
884 suggest that ongoing mineralisation may occur at depth beneath Merapi within the upper part of the
885 plumbing system, during the later stages of magmatic evolution at Merapi.

886 Sulphur-bearing arc magmas are important sources of Cu, and Cu transport has been noted across the
887 Sunda arc (Nadeau *et al.*, 2010; Agangi and Reddy, 2016). Globules of Cu-rich sulphide melt are found in
888 the Merapi lavas recording evidence of Cu-rich sulphide melts exsolving from primitive magma, which
889 are later dissolved in the magmatic-derived volatile phase and distributed through more evolved magmas,
890 and potentially into the host-rock system (Nadeau *et al.*, 2010, 2013a). As previously discussed, the
891 xenoliths are evidence of interaction between this Cu-S-enriched fluid phase and carbonate. In the
892 magmatic skarn xenoliths, Cu is found as cubanite and as a minor constituent in pyrrhotite in zone R2,
893 which are generally surrounded by anhydrite. Disproportionation of SO₂ into sulphide and sulphate is a
894 potential mineralisation process in carbonate and calcium-bearing rocks, and can occur in the timescale of
895 hours (Mavrogenes and Blundy, 2017), and may have formed the coexisting pyrrhotite + cubanite +
896 anhydrite in the xenoliths. Within the magmatic skarn xenolith cores, Cu is rare, only found as a cubanite
897 inclusion in a plagioclase hosted melt inclusion, and as a minor constituent in pyrrhotite inclusions within
898 CaTs-rich clinopyroxene cores. The relative abundance of Cu in zone R2 compared to the core (and
899 exoskarn xenoliths) shows limited transfer of the magmatic-derived volatile phase into the xenolith cores,
900 and/or conditions unfavourable for Cu deposition. Oxygen fugacity is estimated to be similar to typical
901 oxidised arc magma conditions in zone R2 ($\sim \Delta \text{NNO} + 1$), producing favourable conditions for sulphur
902 transport and deposition (e.g. Hattori, 2018). The higher oxygen fugacity estimated in some xenolith cores
903 by the presence of anhydrite and CaTs clinopyroxene cores ($\leq \Delta \text{NNO} + 4$) is potentially too high for Cu
904 transfer, as an upper limit to mineralisation at the hematite-magnetite ($\sim \Delta \text{NNO} + 4$) buffer may exist for
905 porphyry copper deposition (Sun *et al.*, 2013). The large volumes of CO₂ released during decarbonation
906 of the original carbonate which causes this f_{O_2} increase, combined with magmatic CO₂, strongly reduces
907 Cu solubility in the fluid phase (van Hinsberg *et al.*, 2016; Kokh *et al.*, 2017). Vesicles are found within
908 zones proximal to the host lava and the core, suggesting that a high XCO₂ in zone R2 may promote the
909 deposition of Cu before it can be transferred fully into the xenolith core. Xenolith formation temperatures

910 are additionally higher than those estimated for the bulk of Cu and Au deposition in copper porphyry
911 systems (starting < 700°C and dominantly < 400°C) where fluid immiscibility produces coexisting
912 vapour-rich and saline fluid inclusions (Sillitoe, 2010), which are not observed in the xenoliths studied
913 here.

914 Our model, where carbonate is assimilated into a melt from which skarn minerals precipitate (magmatic
915 skarns), has been discussed as a process occurring in many Chinese Cu-Fe-Au-deposits (e.g. Bin and Jin-
916 song, 2016). The xenoliths of this study demonstrate that Cu-Fe sulphides can be formed during this
917 process, and may be capable, at least in part, of producing metal sulphide deposits. Magnetite, hematite
918 and Fe-enrichment in some silicate phases may additionally indicate iron oxide ore potential. Whilst we
919 only have xenoliths that show Cu deposition proximal to the Merapi magma reservoir (no low
920 temperature hydrous skarn phases observed), Cu deposition may occur at greater distances into the
921 contact aureole. Percolation of a Cu-bearing magmatic volatile phase through the carbonate over a longer
922 period of time, on cooling when large amounts of magmatic fluids are released, has potential to promote
923 sulphide and Fe-oxide deposition, enhancing ore forming potential such as observed in copper porphyry
924 systems (e.g. Landtwing *et al.*, 2005; Sillitoe, 2010).

925 **Implications of Carbonate Interaction for the Merapi Magmatic** 926 **System**

927 *Xenocryst Cargo*

928 Calc-silicate xenoliths are ubiquitous in Merapi eruptive deposits, showing that magma-carbonate
929 interaction is an on-going process at Merapi. The amount of interaction is debated in the literature, with
930 estimates of mixing up to 40% recorded in some samples on the basis of isotopic modelling (Troll *et al.*,
931 2013, Borisova *et al.*, 2013, 2016). Although our study cannot elaborate on estimating the volume of
932 carbonate that interacts with Merapi magmas, our data suggests that calc-silicate derived crystals
933 (xenocrysts) may be more difficult to recognise in erupted magmatic deposits than previously appreciated,
934 as we discuss below.

935 Incorporation of skarn-derived minerals into the Merapi magmatic system has been shown previously
936 (Chadwick *et al.* 2007; Deegan *et al.*, 2010; Borisova *et al.*, 2016; Deegan *et al.*, 2016b). Chadwick *et al.*
937 (2007) suggested that 6 to 12 % of crystalline material at Merapi may be crustal derived based on elevated
938 $^{87}\text{Sr}/^{86}\text{Sr}$ plagioclase compositions and distinct major element plagioclase chemistry. Similarly,
939 thermodynamic-geochemical models for the 2010 Merapi eruption are consistent with the incorporation
940 of 18% of crustal calc-silicate material (Borisova *et al.*, 2016). Based on a detailed oxygen isotope study,
941 Borisova *et al.* (2016) were even able to distinguish two stages of magma-crust interaction, resulting in
942 distinct xenocryst plagioclase $\delta^{18}\text{O}$ values related to either high-T altered crustal rocks depleted in ^{18}O or
943 ^{18}O -enriched assimilated carbonate material. . Our data show that both plagioclase and clinopyroxene

944 compositions are produced during magma carbonate interaction in zones R1 and R2 that completely
945 overlap magmatic compositions in respect to major elements (Figs. 6, 7). These minerals are formed as a
946 result of Ca transfer from carbonate to the melt, such as occurs within endoskarns. Increased stability of
947 clinopyroxene and plagioclase in carbonate contaminated melts has been experimentally confirmed across
948 a range of magmatic compositions (e.g. Iacono-Marziano *et al.*, 2007; Mollo *et al.*, 2010; Carter and
949 Dasgupta, 2016), and with rhyoliteMELTS (version 1.2; Gualda *et al.*, 2012; Ghiorso, 2016) which
950 successfully reproduced Ca-contaminated xenolith glass and basaltic andesite compositions. Mineral
951 compositions that are distinct from those found in the magma occur from zone R3 to the xenolith core,
952 but to our knowledge, no highly CaTs-enriched, skarn derived clinopyroxenes have yet been detected in
953 the magmatic products. Although Al-rich clinopyroxenes (up to 8 wt%) are discussed in Costa *et al.*
954 (2013), and were attributed to higher pressure magmatic crystallisation, we have found none in our
955 literature data synthesis that compositionally match our specific skarn clinopyroxenes. Clinopyroxene
956 compositions matching zones R3 and R4, which lie on the DiHd join and are volumetrically more
957 abundant, are also exceedingly rare in the lavas, with only 3 out of 431 analyses reported in Preece (2014)
958 overlapping these compositions. A lack of these compositions may be due to a combination of a
959 volumetrically smaller amount of 'exotic' compositions in the xenolith cores compared to magmatic-type
960 compositions in the xenolith endoskarn rims. Alternatively, dissolution into the magma, and/or re-
961 equilibration with the magma might also be an option. Indeed, Carter and Dasgupta (2016) showed that in
962 carbonate assimilation experiments, within 48 hours, initially compositionally variable clinopyroxenes
963 had equilibrated to a diopsidic composition. Some crystals that are a result of magma-carbonate
964 interaction may therefore be 'cryptic' and distinguishable from magmatic crystals only on the basis of
965 their isotope or trace element chemistry (e.g. Chadwick *et al.*, 2007; Borisova *et al.*, 2016). Another
966 consequence of this finding is that clinopyroxene thermobarometry may include carbonate-interaction
967 pressures and temperatures in their output. Although *in situ* oxygen isotope evidence for magma-
968 carbonate interaction in Merapi clinopyroxene shows limited crustal additions to the bulk of the crystals
969 (Deegan *et al.*, 2016b), a small number of the clinopyroxenes analysed by Deegan *et al.* (2016b) have
970 anomalously high oxygen isotope ratios ($\delta^{18}\text{O}$ values of up to c. 7 ‰), which may be a result of magma-
971 carbonate interaction. Furthermore, studies utilising *in situ* isotope analysis of other mineral phases such
972 as plagioclase for Sr (Chadwick *et al.*, 2007) and oxygen (Borisova *et al.*, 2016) have demonstrated the
973 presence of xenocrysts and contaminated mineral zones, consistent with the usually shallow
974 crystallisation of intermediate plagioclase (e.g. Chadwick *et al.*, 2013). Whilst our plagioclase data for the
975 glass-rich zone R4 have high-FeO that overlaps some literature values for plagioclase in lavas, and
976 therefore may suggest that high-FeO plagioclase in lavas might be xenocrystic, this is more likely to be a
977 result of disequilibria due to quenching of the xenolith glass. For example, FeO in plagioclase increases
978 with cooling rate, producing plagioclase with up to 2.33 wt% FeO in 15°C/min experiments (Mollo *et al.*,
979 2011). The zone R4 plagioclase crystals contain up to 1.7 wt% FeO, and similarly wollastonite crystals in

980 zone R4 have thin Fe-rich ferro-bustamite overgrowths, indicating that cooling rate may have the more
981 pronounced impact on Fe-rich mineral rims in the xenoliths.

982 *Magma Composition*

983 Much of the experimental work on magma-carbonate interaction focuses on reproducing the highly
984 potassic, silica-undersaturated compositions erupted at volcanoes such as Vesuvius and Colli Albani
985 (e.g. Iacono-Marziano *et al.*, 2007; Mollo *et al.*, 2010; Jolis *et al.*, 2013). Strong silica-undersaturation
986 from carbonate assimilation in Italian volcanoes is a result of the increased stability of clinopyroxene
987 taking up SiO₂, coupled with the redissolution of olivine, which drives melts towards silica
988 undersaturation (e.g. Mollo *et al.*, 2010). Recent Merapi lava whole rock compositions range from ~50 to
989 68 wt% SiO₂, and the interstitial glasses within these record pre-eruptive melts with 60-75 wt% SiO₂ (Fig.
990 9). These would not be driven to silica-undersaturation by an increase in clinopyroxene or plagioclase
991 precipitation due to these minerals containing lower SiO₂ concentrations. Whole-rock compositions
992 instead traverse a differentiation vector defined by that of the typical arc magma plagioclase and
993 clinopyroxene differentiation assemblage (Fig. 9; *c.f.* Handley *et al.*, 2014), although at a slightly elevated
994 CaO. It is interesting to note however, that while the overall major element chemistry at Merapi is not
995 dominated by a carbonate assimilation signature, very rare, highly localised phonolitic leucite-bearing
996 silica-undersaturated melts have been identified in some Merapi calc-silicate xenoliths by Brouwer (1928,
997 1945). These demonstrate that these exotic compositions can be formed at Merapi during very localised
998 periods of extremely high levels of carbonate interaction, but the quantities of melt generated are
999 volumetrically negligible.

1000 In addition to the effects of crystal fractionation on the major element chemistry, lower temperature, high-
1001 SiO₂ melts such as those represented by the groundmass lava glass compositions at Merapi have a lower
1002 capacity to assimilate material than hotter mafic melts (e.g. Wenzel *et al.*, 2002; Barnes *et al.*, 2005;
1003 Gaeta *et al.*, 2009; Jolis *et al.*, 2015), and instead favour formation of skarn minerals (e.g. wollastonite)
1004 that cause only small apparent changes to melt compositions (Spandler *et al.*, 2012; Carter and Dasgupta,
1005 2016). These minerals may become trapped as a cumulate or exoskarn layer (see above, e.g. Gaeta *et al.*,
1006 2009; Di Rocco *et al.*, 2012) at the wall rock contact, and only have a small impact on the melt
1007 composition during skarn recycling and xenocryst incorporation (e.g. Di Rocco *et al.*, 2012; Jolis *et al.*,
1008 2015). A discrepancy between limited whole-rock major element evidence for magma-carbonate
1009 interaction (*c.f.* Costa *et al.*, 2013; Handley *et al.*, 2014) and high levels of interaction recorded in
1010 multiple isotope systems (Chadwick *et al.*, 2007; Troll *et al.*, 2013; Borisova *et al.*, 2013, 2016), may thus
1011 be due a combination of the lower capacity of the magmatic melt to incorporate carbonate material, and a
1012 relatively limited mobility of Ca in these relatively low temperature, high SiO₂ Merapi pre-eruptive melts
1013 compared to the higher mobilities usually displayed by isotopes of trace elements (e.g. Sr, B). This
1014 decoupling has been observed in high temperature (1200°C) carbonate interaction experiments (Deegan *et*

1015 *al.*, 2010, 2016a; Blythe *et al.*, 2015). Moreover, quantitative modelling of magma-carbonate interaction
1016 demonstrated that low-to-moderate amounts of carbonate assimilation cause only limited changes to the
1017 major element chemistry of the magma (Spandler *et al.*, 2012). Whereas there is no doubt that magma-
1018 carbonate interaction is an important petrogenetic process at Merapi, the degree of major element
1019 compositional change may not be prominent enough to distinguish the modified magma from the overall
1020 spectrum of Merapi magmas (*c.f.* Spandler *et al.*, 2012).

1021 *Merapi Volatile Budget*

1022 Carbonate assimilation at Merapi has been shown to have a strong impact on the composition of the gases
1023 released to the atmosphere. Release of crustal derived CO₂ has been proposed by identification of
1024 elevated $\delta^{13}\text{C}$ and He isotopes in fumarole gases (Troll *et al.*, 2012, 2013 and references therein). An
1025 increase in these isotopic tracers has additionally been observed during eruptive periods, attributed to a
1026 positive feedback loop of wall rock fracturing during eruption, and increased CO₂ liberation from magma-
1027 carbonate interaction on this increased surface area (Deegan *et al.*, 2011; Troll *et al.*, 2012; Carr *et al.*,
1028 2018). Our work shows that the magmatic skarn xenoliths may represent snapshots of this syn-magmatic
1029 carbonate interaction, and therefore eruptive flare-ups could potentially be influenced by temporal
1030 increases in carbonate interaction (*c.f.* Troll *et al.*, 2012; Carr *et al.*, 2018). The 2010 eruption was
1031 preceded by an influx of hotter volatile-rich magma that exceeded the capacity of the shallow storage
1032 system (Costa *et al.*, 2013; Preece *et al.*, 2016; Carr *et al.*, 2020). This increased heat and volume would
1033 have caused both increased thermal decarbonation and fracturing, which could penetrate deeper into the
1034 bedrock. A positive feedback would then occur, where increased decarbonation promotes a decrease in
1035 water solubility, producing bubbles and more explosive behaviour, promoting more fracturing, resulting
1036 in temporal increases in carbonate interaction (Deegan *et al.*, 2011; Troll *et al.*, 2012; Carr *et al.*, 2018;
1037 2020). Dome instability from weakened fractured/alterd wall-rock could also contribute to magmatic
1038 overpressure through increasing fracturing, and a resulting larger surface area of the carbonate available
1039 to react (Mollo *et al.*, 2012). In the magmatic skarn xenoliths, residual calcite is only present in trace
1040 quantities, and the $\delta^{13}\text{C}$ composition of these calcites are exceptionally negative (down to -29 ‰),
1041 demonstrating extremely efficient decarbonation in the magmatic skarn xenoliths (Whitley *et al.*, 2019). It
1042 is unlikely that this is exclusive to Merapi, and indeed, temporal increases in carbonate assimilation
1043 increasing explosivity has been proposed elsewhere e.g. at Colli Albani (Freda *et al.*, 2011) and Vesuvius
1044 (Jolis *et al.*, 2015). CO₂ release is not restricted to just syn-magmatic carbonate interaction, and
1045 decarbonation reactions in the exoskarn additionally add to the CO₂ budget. The current CO₂ output at
1046 Merapi compared to estimated contact metamorphic aureole volumes around a Merapi reservoir
1047 demonstrate that this CO₂ release is rapid, on the timescales of just thousands of years (Whitley *et al.*,
1048 2019). When considering volcanoes that interacted with crustal carbonate, at present and in the geological

1049 past (*c.f.* Mason *et al.*, 2017; Carter and Dasgupta, 2018), CO₂ release such as evidenced at Merapi may
1050 have the potential to modify long term climatic trends.

1051 **CONCLUSIONS**

1052 A detailed mineralogical, petrological and geochemical study of a range of calc-silicate (skarn-type)
1053 xenoliths from Merapi volcano shows that two distinct types of xenoliths are present; magmatic skarn
1054 xenoliths that record syn-magmatic magma-carbonate interaction that preserves abundant CaO-rich glass,
1055 and fragments of the metasomatic exoskarn aureole around the Merapi magma reservoir, respectively.
1056 Thermobarometry indicates that the CaO-rich glass-bearing magmatic skarn xenoliths formed at ~850°C.
1057 Fluid inclusions record shallow pressures of < 100 MPa, corresponding to depths < 3.7 km. These
1058 xenoliths are the physical representation of carbonate entrained during eruptive events, which we interpret
1059 to increase eruption intensity during rapid decarbonation. The disaggregated nature of some of these
1060 xenoliths, and the similarity in the geochemistry of lava and some xenolith minerals, indicate that skarn-
1061 derived xenocrysts may be difficult to recognise at Merapi. Experimental comparisons and
1062 thermodynamic modelling indicate formation temperatures of 510 to 910°C for the range of mineralogies
1063 shown in the metasomatic exoskarn xenoliths. A newly developed oxybarometric model indicates a wide
1064 range of fO_2 conditions during xenolith formation. Magmatic skarn xenoliths are predominantly formed
1065 around the NNO buffer, similar to magmatic values, whilst the cores of these xenoliths can reach values
1066 above the HM buffer in the presence of an increased amount of newly released CO₂. Protracted periods of
1067 CO₂ flushing caused conditions predominantly above the NNO buffer during exoskarn formation,
1068 covering the full range between NNO and air. High fO_2 in both xenolith types promoted formation of
1069 andradite garnet and highly aluminous clinopyroxene compositions. A magmatic volatile phase present at
1070 Merapi reacts with the xenoliths to form rare Ca-Al-Si-F-Cl phases such as cuspidine, ellestadite and
1071 wadalite-like phases. Evidence of xenolith formation during eruptive timescales demonstrates that
1072 magma-carbonate interaction and subsequent CO₂ release could affect eruption intensity, as recently
1073 suggested for Merapi and similar carbonate-hosted volcanoes elsewhere. In addition, copper and
1074 occasionally Fe (and likely other associated elements of economic value such as Zn) are carried within
1075 this fluid and are found concentrated in the outer shells of some of the xenoliths, indicating potential for
1076 ongoing skarn-type mineralisation at depth beneath Merapi and similar volcanoes within carbonate
1077 basement worldwide.

1078 **ACKNOWLEDGEMENTS**

1079 We thank Barbara Mader and Peter Appel (Kiel University) for assistance with microprobe analyses,
1080 Petra Herms (Kiel University) for advice about fluid inclusion analysis, Vladimir Zholobenko (Keele

1081 University) for assistance with Raman analysis and Luke Hepworth for additional calcite EMPA analyses.
1082 Peter Greatbatch's and David Wilde's (Keele University) thin section preparation skills are greatly
1083 appreciated. We also thank Dorota Środek (University of Silesia) for discussion about the unusual skarn
1084 minerals. Massimio d'Antonio and Anastassia Borisova are thanked for providing constructive reviews
1085 that helped to improve the manuscript, and we also thank Gerhard Wörner for editorial handling.
1086 Financial support from NERC (grant IMF620/0517), Keele University, the Keele Postgraduate
1087 Association, and the Swedish Research Council is gratefully acknowledged.

1088 REFERENCES

- 1089 Aarnes, I., Svensen, H., Connolly, J. A. D. & Podladchikov, Y. Y. (2010). How contact metamorphism
1090 can trigger global climate changes: Modelling gas generation around igneous sills in sedimentary basins.
1091 *Geochimica et Cosmochimica Acta* **74**, 7179–7195.
- 1092 Agangi, A. & Reddy, S. M. (2016). Open-system behaviour of magmatic fluid phase and transport of
1093 copper in arc magmas at Krakatau and Batur volcanoes, Indonesia. *Journal of Volcanology and*
1094 *Geothermal Research* **327**, 669–686.
- 1095 Aiuppa, A., Fischer, T. P., Plank, T., Robidou, P. & Di Napoli, R. (2017). Along-arc, inter-arc and arc-
1096 to-arc variations in volcanic gas CO₂/S_T ratios reveal dual source of carbon in arc volcanism. *Earth-*
1097 *Science Reviews* **168**, 24–47.
- 1098 Anderson, A. (1973). The before-eruption water content of some high-alumina magmas. *Bulletin*
1099 *Volcanologique* **37**, 530–552.
- 1100 Anderson, A. T. (1974). Evidence for a picritic, volatile-rich magma beneath Mt. Shasta, California.
1101 *Journal of Petrology* **15**, 243–267.
- 1102 Andreastuti, S., Alloway, B. & Smith, I. (2000). A detailed tephrostratigraphic framework at Merapi
1103 Volcano, Central Java, Indonesia: implications for eruption predictions and hazard assessment. *Journal of*
1104 *Volcanology and Geothermal Research* **100**, 51–67.
- 1105 Arai, H. (2010). A function for the R programming language to recast garnet analyses into end-members:
1106 Revision and porting of Muhling and Griffin's method. *Computers & Geosciences* **36**, 406–409.
- 1107 Barnes, C. G., Prestvik, T., Sundvoll, B. & Surratt, D. (2005). Pervasive assimilation of carbonate and
1108 silicate rocks in the Hortavær igneous complex, north-central Norway. *Lithos* **80**, 179–199.
- 1109 Berndt, J., Koepke, J. & Holtz, F. (2005). An experimental investigation of the influence of water and
1110 oxygen fugacity on differentiation of MORB at 200 MPa. *Journal of Petrology* **46**, 135–167.
- 1111 Bin, Z. & Jin-song, Z. (2016). The main features of magmatic skarns and their formation mechanism.
1112 *AshEse Journal of Engineering* **2**, 22–65.
- 1113 Blythe, L. S., Deegan, F. M., Freda, C., Jolis, E. M., Masotta, M., Misiti, V., Taddeucci, J. & Troll, V. R.
1114 (2015). CO₂ bubble generation and migration during magma–carbonate interaction. *Contributions to*
1115 *Mineralogy and Petrology* **169**, 1–16.

- 1116 Bolio-Arceo, H. & Glasser, F. P. (1990). Formation of spurrite, $\text{Ca}_5(\text{SiO}_4)_2\text{CO}_3$. *Cement and Concrete*
1117 *Research* **20**, 301–307.
- 1118 Borisova, A. Y., Gurenko, A. A., Martel, C., Kouzmanov, K., Cathala, A., Bohrsen, W. A., Pratomo, I. &
1119 Sumarti, S. (2016). Oxygen isotope heterogeneity of arc magma recorded in plagioclase from the 2010
1120 Merapi eruption (Central Java, Indonesia). *Geochimica et Cosmochimica Acta* **190**, 13–34.
- 1121 Borisova, A. Y., Martel, C., Gouy, S., Pratomo, I., Sumarti, S., Toutain, J.-P., Bindeman, I. N., de
1122 Parseval, P. & Métaxian, J.-P. (2013). Highly explosive 2010 Merapi eruption: evidence for shallow-level
1123 crustal assimilation and hybrid fluid. *Journal of Volcanology and Geothermal Research* **261**, 193–208.
- 1124 Borisova, A. Y., Toutain, J.-P., Dubessy, J., Pallister, J., Zwick, A. & Salvi, S. (2014). H_2O - CO_2 -S fluid
1125 triggering the 1991 Mount Pinatubo climactic eruption (Philippines). *Bulletin of Volcanology* **76**, 800.
- 1126 Brouwer, H. (1928). Production of Trachyte and Phonolite from Pyroxene Andesitic Magma Associated
1127 with Limestone. *The Journal of Geology* **36**, 545–548.
- 1128 Brouwer, H.A. (1945). The association of alkali rocks and metamorphic limestone in a block ejected by
1129 the volcano Merapi (Java). Koninklijke Nederlandse Akademie van Wetenschappen.
- 1130 Büttner, S.H. (2012). Rock Maker: an MS Excel™ spreadsheet for the calculation of rock compositions
1131 from proportional whole rock analyses, mineral compositions, and modal abundance. *Mineralogy and*
1132 *Petrology* **104**, 129–135.
- 1133 Camus, G., Gourgaud, A., Mossand-Berthommier, P.-C. & Vincent, P.-M. (2000). Merapi (Central Java,
1134 Indonesia): an outline of the structural and magmatological evolution, with a special emphasis to the
1135 major pyroclastic events. *Journal of Volcanology and Geothermal Research* **100**, 139–163.
- 1136 Carr, B.B., Clarke, A.B. & de' Michieli Vitturi, M. (2018). Earthquake induced variations in extrusion
1137 rate: A numerical modeling approach to the 2006 eruption of Merapi Volcano (Indonesia). *Earth and*
1138 *Planetary Science Letters* **482**, 377–387.
- 1139 Carr, B. B., Clarke, A. B. & de' Michieli Vitturi, M. (2020). Volcanic conduit controls on effusive-
1140 explosive transitions and the 2010 eruption of Merapi Volcano (Indonesia). *Journal of Volcanology and*
1141 *Geothermal Research* **392**, 106767.
- 1142 Carroll, M. R. & Rutherford, M. J. (1987). The stability of igneous anhydrite: experimental results and
1143 implications for sulfur behavior in the 1982 El Chichon trachyandesite and other evolved magmas.
1144 *Journal of Petrology* **28**, 781–801.
- 1145 Carter, L. B. & Dasgupta, R. (2018). Decarbonation in the Ca-Mg-Fe carbonate system at mid-crustal
1146 pressure as a function of temperature and assimilation with arc magmas—Implications for long-term
1147 climate. *Chemical Geology* **492**, 30–48.
- 1148 Carter, L. B. & Dasgupta, R. (2015). Hydrous basalt–limestone interaction at crustal conditions:
1149 Implications for generation of ultracalcic melts and outflux of CO_2 at volcanic arcs. *Earth and Planetary*
1150 *Science Letters* **427**, 202–214.
- 1151 Carter, L. B. & Dasgupta, R. (2016). Effect of melt composition on crustal carbonate assimilation:
1152 Implications for the transition from calcite consumption to skarnification and associated CO_2 degassing.
1153 *Geochemistry, Geophysics, Geosystems* **17**, 3893–3916.

- 1154 Chadwick, J. P., Troll, V. R., Ginibre, C., Morgan, D., Gertisser, R., Waight, T. E. & Davidson, J. P.
1155 (2007). Carbonate assimilation at Merapi Volcano, Java, Indonesia: insights from crystal isotope
1156 stratigraphy. *Journal of Petrology* **48**, 1793–1812.
- 1157 Chadwick, J. P., Troll, V. R., Waight, T. E., van der Zwan, F. M. & Schwarzkopf, L. M. (2013).
1158 Petrology and geochemistry of igneous inclusions in recent Merapi deposits: a window into the sub-
1159 volcanic plumbing system. *Contributions to Mineralogy and Petrology* **165**, 259–282.
- 1160 Charlu, T. V., Newton, R. C. & Kleppa, O. J. (1981). Thermochemistry of synthetic $\text{Ca}_2\text{Al}_2\text{SiO}_7$
1161 (gehlenite)- $\text{Ca}_2\text{MgSi}_2\text{O}_7$ (åkermanite) melilites. *Geochimica et Cosmochimica Acta* **45**, 1609–1617.
- 1162 Clocchiatti, R., Joron, J. L., Kerinec, F. & Treuil, M. (1982). Quelques données préliminaires sur la lave
1163 du dôme actuel du volcan Mérapi (Java, Indonésie) et sur ses enclaves. *Comptes rendus de l'Académie
1164 des Sciences Paris* **295**, 817–822.
- 1165 Commer, M., Helwig, S. L., Hördt, A., Scholl, C. & Tezkan, B. (2006). New results on the resistivity
1166 structure of Merapi Volcano (Indonesia), derived from three-dimensional restricted inversion of long-
1167 offset transient electromagnetic data. *Geophysical Journal International* **167**, 1172–1187.
- 1168 Conte, A. M., Dolfi, D., Gaeta, M., Misiti, V., Mollo, S. & Perinelli, C. (2009). Experimental constraints
1169 on evolution of leucite-basanite magma at 1 and 10^{-4} GPa: implications for parental compositions of
1170 Roman high-potassium magmas. *European Journal of Mineralogy* **21**, 763–782.
- 1171 Cortés, J.A., Wilson, M., Condliffe, E. & Francalanci, L. (2006). The occurrence of forsterite and highly
1172 oxidizing conditions in basaltic lavas from Stromboli volcano, Italy. *Journal of Petrology* **47**, 1345–1373.
- 1173 Costa, F., Andreastuti, S., Bouvet de Maisonneuve, C. & Pallister, J. S. (2013). Petrological insights into
1174 the storage conditions, and magmatic processes that yielded the centennial 2010 Merapi explosive
1175 eruption. *Journal of Volcanology and Geothermal Research* **261**, 209–235.
- 1176 Danyushevsky, L., Della-Pasqua, F. & Sokolov, S. (2000). Re-equilibration of melt inclusions trapped by
1177 magnesian olivine phenocrysts from subduction-related magmas: petrological implications. *Contributions
1178 to Mineralogy and Petrology* **138**, 68–83.
- 1179 de Capitani, C. & Petrakakis, K. (2010). The computation of equilibrium assemblage diagrams with
1180 Theriak/Domino software. *American Mineralogist* **95**, 1006–1016.
- 1181 Deegan, F. M., Troll, V. R., Freda, C., Misiti, V. & Chadwick, J. P. (2011). Fast and furious: crustal CO_2
1182 release at Merapi volcano, Indonesia. *Geology Today* **27**, 63–64.
- 1183 Deegan, F. M., Troll, V. R., Freda, C., Misiti, V., Chadwick, J. P., McLeod, C. L. & Davidson, J. P.
1184 (2010). Magma–carbonate interaction processes and associated CO_2 release at Merapi Volcano,
1185 Indonesia: insights from experimental petrology. *Journal of Petrology* **51**, 1027–1051.
- 1186 Deegan, F. M., Troll, V. R., Whitehouse, M. J., Jolis, E. M. & Freda, C. (2016a). Boron isotope
1187 fractionation in magma via crustal carbonate dissolution. *Scientific Reports* **6**, 30774.
- 1188 Deegan, F. M., Whitehouse, M. J., Troll, V. R., Budd, D. A., Harris, C., Geiger, H. & Hålenius, U.
1189 (2016b). Pyroxene standards for SIMS oxygen isotope analysis and their application to Merapi volcano,
1190 Sunda arc, Indonesia. *Chemical Geology* **447**, 1–10.

- 1191 Deer, W. A., Howie, R. A. & Zussman, J. (1997). Rock-Forming Minerals. Single-Chain silicates,
1192 volume 2A, 2nd edition. The Geological Society, London, 680 pp.
- 1193 Del Moro, S., Renzulli, A. & Tribaudino, M. (2011). Pyrometamorphic processes at the magma–
1194 hydrothermal system interface of active volcanoes: Evidence from buchite ejecta of Stromboli (Aeolian
1195 Islands, Italy). *Journal of Petrology* **52**, 541–564.
- 1196 Devine, J. D., Gardner, J. E., Brack, H. P., Laynet, G. D. & Rutherford, M. J. (1995). Comparison of
1197 microanalytical methods for estimating H₂O contents of silicic volcanic glasses. *American Mineralogist*
1198 **80**, 319–328.
- 1199 Di Rocco, T., Freda, C., Gaeta, M., Mollo, S. & Dallai, L. (2012). Magma chambers emplaced in
1200 carbonate substrate: petrogenesis of skarn and cumulate rocks and implications for CO₂ degassing in
1201 volcanic areas. *Journal of Petrology* **53**, 2307–2332.
- 1202 Droop, G. (1987). A general equation for estimating Fe³⁺ concentrations in ferromagnesian silicates and
1203 oxides from microprobe analyses, using stoichiometric criteria. *Mineralogical Magazine* **51**, 431–435.
- 1204 Erdmann, S., Martel, C., Pichavant, M., Bourdier, J.-L., Champallier, R., Komorowski, J.-C. & Cholik, N.
1205 (2016). Constraints from phase equilibrium experiments on pre-eruptive storage conditions in mixed
1206 magma systems: a case study on crystal-rich basaltic andesites from Mount Merapi, Indonesia. *Journal of*
1207 *Petrology* **57**, 535–560.
- 1208 Erdmann, S., Martel, C., Pichavant, M. & Kushnir, A. (2014). Amphibole as an archivist of magmatic
1209 crystallization conditions: problems, potential, and implications for inferring magma storage prior to the
1210 paroxysmal 2010 eruption of Mount Merapi, Indonesia. *Contributions to Mineralogy and Petrology* **167**,
1211 1016.
- 1212 Feig, S. T., Koepke, J. & Snow, J. E. (2006). Effect of water on tholeiitic basalt phase equilibria: an
1213 experimental study under oxidizing conditions. *Contributions to Mineralogy and Petrology* **152**, 611–
1214 638.
- 1215 Feig, S. T., Koepke, J. & Snow, J. E. (2010). Effect of oxygen fugacity and water on phase equilibria of a
1216 hydrous tholeiitic basalt. *Contributions to Mineralogy and Petrology* **160**, 551–568.
- 1217 Freda, C., Gaeta, M., Giaccio, B., Marra, F., Palladino, D. M., Scarlato, P. & Sottili, G. (2011). CO₂-
1218 driven large mafic explosive eruptions: the Pozzolane Rosse case study from the Colli Albani Volcanic
1219 District (Italy). *Bulletin of Volcanology* **73**, 241–256.
- 1220 Freise, M., Holtz, F., Nowak, M., Scoates, J. S. & Strauss, H. (2009). Differentiation and crystallization
1221 conditions of basalts from the Kerguelen large igneous province: an experimental study. *Contributions to*
1222 *Mineralogy and Petrology* **158**, 505.
- 1223 Frezzotti, M.-L., Andersen, T., Neumann, E.-R. & Simonsen, S. L. (2002). Carbonatite melt–CO₂ fluid
1224 inclusions in mantle xenoliths from Tenerife, Canary Islands: a story of trapping, immiscibility and fluid–
1225 rock interaction in the upper mantle. *Lithos* **64**, 77–96.
- 1226 Frezzotti, M.-L., Peccerillo, A., Zanon, V. & Nikogosian, I. (2004). Silica-rich melts in quartz xenoliths
1227 from Vulcano Island and their bearing on processes of crustal anatexis and crust–magma interaction
1228 beneath the Aeolian Arc, Southern Italy. *Journal of Petrology* **45**, 3–26.

- 1229 Frost, B.R. (1991). Introduction to oxygen fugacity and its petrologic importance. *Reviews in Mineralogy*
1230 *and Geochemistry* **25**, 1–9.
- 1231 Fujita, S., Suzuki, K., Ohkawa, M., Shibasaki, Y. & Mori, T. (2001). Reaction of hydrogrossular with
1232 hydrogen chloride gas at high temperature. *Chemistry of Materials* **13**, 2523–2527.
- 1233 Fulignati, P., Kamenetsky, V. S., Marianelli, P. & Sbrana, A. (2013). PIXE mapping on multiphase fluid
1234 inclusions in endoskarn xenoliths of AD 472 eruption of Vesuvius (Italy). *Periodico di Mineralogia* **82**,
1235 291–297.
- 1236 Fulignati, P., Kamenetsky, V. S., Marianelli, P., Sbrana, A. & Mernagh, T. P. (2001). Melt inclusion
1237 record of immiscibility between silicate, hydrosaline, and carbonate melts: Applications to skarn genesis
1238 at Mount Vesuvius. *Geology* **29**, 1043–1046.
- 1239 Fulignati, P., Marianelli, P., Santacroce, R. & Sbrana, A. (2004). Probing the Vesuvius magma chamber–
1240 host rock interface through xenoliths. *Geological Magazine* **141**, 417–428.
- 1241 Gaeta, M., Rocco, T.D. & Freda, C. (2009). Carbonate assimilation in open magmatic systems: the role of
1242 melt-bearing skarns and cumulate-forming processes. *Journal of Petrology* **50**, 361–385.
- 1243 Galuskin, E. V., Galuskina, I. O., Bailau, R., Prusik, K., Gazeev, V. M., Zadov, A. E., Pertsev, N. N.,
1244 Ježak, L., Gurbanov, A. G. & Dubrovinsky, L. (2013). Eltyubyuite, $\text{Ca}_{12}\text{Fe}^{3+}_{10}\text{Si}_4\text{O}_{32}\text{Cl}_6$ –the Fe^{3+}
1245 analogue of wadalite: a new mineral from the Northern Caucasus, Kabardino-Balkaria, Russia. *European*
1246 *Journal of Mineralogy* **25**, 221–229.
- 1247 Galuskin, E. V., Gfeller, F., Galuskina, I. O., Armbruster, T., Bailau, R. & Sharygin, V. V. (2015).
1248 Mayenite supergroup, part I: Recommended nomenclature. *European Journal of Mineralogy* **27**, 99–111.
- 1249 Ganino, C., Arndt, N. T., Zhou, M.-F., Gaillard, F. & Chauvel, C. (2008). Interaction of magma with
1250 sedimentary wall rock and magnetite ore genesis in the Panzhihua mafic intrusion, SW China.
1251 *Mineralium Deposita* **43**, 677.
- 1252 Gertisser, R. (2001). Gunung Merapi (Java, Indonesien): Eruptionsgeschichte und magmatische Evolution
1253 eines Hochrisiko-Vulkans (PhD thesis). University of Freiburg, Freiburg, Germany.
- 1254 Gertisser, R., Charbonnier, S. J., Keller, J. & Quidelleur, X. (2012). The geological evolution of Merapi
1255 volcano, Central Java, Indonesia. *Bulletin of Volcanology* **74**, 1213–1233.
- 1256 Gertisser, R., Charbonnier, S. J., Troll, V. R., Keller, J., Preece, K., Chadwick, J., Barclay, J. & Herd, R.
1257 (2011). Merapi (Java, Indonesia): anatomy of a killer volcano. *Geology Today* **27**, 57–62.
- 1258 Gertisser, R. & Keller, J. (2003a). Temporal variations in magma composition at Merapi Volcano
1259 (Central Java, Indonesia): magmatic cycles during the past 2000 years of explosive activity. *Journal of*
1260 *Volcanology and Geothermal Research* **123**, 1–23.
- 1261 Gertisser, R. & Keller, J. (2003b). Trace element and Sr, Nd, Pb and O isotope variations in medium-K
1262 and high-K volcanic rocks from Merapi Volcano, Central Java, Indonesia: evidence for the involvement
1263 of subducted sediments in Sunda arc magma genesis. *Journal of Petrology* **44**, 457–489.
- 1264 Ghiorso, M.S. (2016). Modeling carbonate assimilation into crustal magmas: Quantifying overpressure
1265 and eruption triggers. Goldschmidt Conference Abstracts 934, Yokohama, Japan.

- 1266 Glasser, F. (1995). Comments on wadalite, $\text{Ca}_6\text{Al}_5\text{Si}_2\text{O}_{16}\text{Cl}_3$, and the structures of garnet, mayenite and
1267 calcium chlorosilicate. Addendum. *Acta Crystallographica Section C: Crystal Structure Communications*
1268 **51**, 340–340.
- 1269 Goff, F., Love, S. P., Warren, R. G., Counce, D., Obenholzner, J., Siebe, C. & Schmidt, S. C. (2001).
1270 Passive infrared remote sensing evidence for large, intermittent CO_2 emissions at Popocatepetl volcano,
1271 Mexico. *Chemical Geology* **177**, 133–156.
- 1272 Goldstein, R. H. (2003). Petrographic analysis of fluid inclusions, in: Samson, I., Anderson, A., Marshall,
1273 D. (Eds.), *Fluid Inclusions: Analysis and Interpretation*, Mineral Association of Canada Short Course.
1274 Mineralogical Association of Canada Vancouver, pp. 9–53.
- 1275 Gordon, T. M. & Greenwood, H. J. (1971). The Stability of Grossularite in $\text{H}_2\text{O}-\text{CO}_2$ Mixtures.
1276 *American Mineralogist* **56**, 1674–1688.
- 1277 Gorzkowska, I., Maciejewski, M. & Rudnicki, R. (1988a). Thermal decomposition of CaCO_3 in the
1278 presence of calcium fluoride. *Journal of Thermal Analysis and Calorimetry* **33**, 983–990.
- 1279 Gorzkowska, I., Maciejewski, M. & Rudnicki, R. (1988b). Application of DTA and TG to studies of the
1280 CaCO_3 - CaF_2 phase diagram. *Journal of Thermal Analysis and Calorimetry* **33**, 991–995.
- 1281 Grew, E. S., Locock, A. J., Mills, S. J., Galuskina, I. O., Galuskin, E. V. & Hålenius, U. (2013).
1282 Nomenclature of the garnet supergroup. *American Mineralogist* **98**, 785–811.
- 1283 Gualda, G. A., Ghiorso, M. S., Lemons, R. V. & Carley, T. L. (2012). Rhyolite-MELTS: a modified
1284 calibration of MELTS optimized for silica-rich, fluid-bearing magmatic systems. *Journal of Petrology* **53**,
1285 875–890.
- 1286 Gustafson, W.I. (1974). The stability of andradite, hedenbergite, and related minerals in the system Ca-
1287 Fe-Si-O-H. *Journal of Petrology* **15**, 455–496.
- 1288 Handley, H. K., Blichert-Toft, J., Gertisser, R., Macpherson, C. G., Turner, S. P., Zaennudin, A. &
1289 Abdurrachman, M. (2014). Insights from Pb and O isotopes into along-arc variations in subduction inputs
1290 and crustal assimilation for volcanic rocks in Java, Sunda arc, Indonesia. *Geochimica et Cosmochimica*
1291 *Acta* **139**, 205–226.
- 1292 Hansteen, T.H. & Klügel, A. (2008). Fluid inclusion thermobarometry as a tracer for magmatic processes.
1293 *Reviews in Mineralogy and Geochemistry* **69**, 143–177.
- 1294 Hartley, M. E., Bali, E., MacLennan, J., Neave, D. A. & Halldórsson, S. A. (2018). Melt inclusion
1295 constraints on petrogenesis of the 2014–2015 Holuhraun eruption, Iceland. *Contributions to Mineralogy*
1296 *and Petrology* **173**, 1.
- 1297 Hattori, K. (2018). Porphyry copper potential in Japan based on magmatic oxidation state. *Resource*
1298 *Geology* **68**, 126–137.
- 1299 Henmi, C. & Henmi, K. (1978). Synthesis of spurrite and tilleyite at low CO_2 partial pressure.
1300 *Mineralogical Journal* **9**, 106–110.
- 1301 Hirschmann, M., Ghiorso, M., Davis, F., Gordon, S., Mukherjee, S., Grove, T., Krawczynski, M.,
1302 Medard, E. & Till, C. (2008). Library of Experimental Phase Relations (LEPR): A database and Web

- 1303 portal for experimental magmatic phase equilibria data. *Geochemistry, Geophysics, Geosystems* **9**,
1304 Q03011.
- 1305 Holland, T. J. B. & Powell, R. (1998). An internally consistent thermodynamic data set for phases of
1306 petrological interest. *Journal of Metamorphic Geology* **16**, 309–343.
- 1307 Huckenholz, H., Lindhuber, W. & Springer, J. (1974). The join $\text{CaSiO}_3\text{-Al}_2\text{O}_3\text{-Fe}_2\text{O}_3$ of the CaO-
1308 $\text{Al}_2\text{O}_3\text{-Fe}_2\text{O}_3\text{-SiO}_2$ quaternary system and its bearing on the formation of granditic garnets and fassaitic
1309 pyroxenes. *Neues Jahrbuch für Mineralogie, Abhandlungen* **121**, 160–207.
- 1310 Iacono-Marziano, G., Gaillard, F. & Pichavant, M. (2007). Limestone assimilation and the origin of CO_2
1311 emissions at the Alban Hills (Central Italy): constraints from experimental petrology. *Journal of*
1312 *Volcanology and Geothermal Research* **166**, 91–105.
- 1313 Iacono-Marziano, G., Gaillard, F. & Pichavant, M. (2008). Limestone assimilation by basaltic magmas:
1314 an experimental re-assessment and application to Italian volcanoes. *Contributions to Mineralogy and*
1315 *Petrology* **155**, 719–738.
- 1316 Innocenti, S., del Marmol, M.-A., Voight, B., Andreastuti, S. & Furman, T. (2013). Textural and mineral
1317 chemistry constraints on evolution of Merapi Volcano, Indonesia. *Journal of Volcanology and*
1318 *Geothermal Research* **261**, 20–37.
- 1319 Jago, B. C. & Gittins, J. (1991). The role of fluorine in carbonatite magma evolution. *Nature* **349**, 56–58.
- 1320 Joesten, R. (1974). Local equilibrium and metasomatic growth of zoned calc-silicate nodules from a
1321 contact aureole, Christmas Mountains, Big Bend region, Texas. *American Journal of Science* **274**, 876–
1322 901.
- 1323 Jolis, E. M., Freda, C., Troll, V. R., Deegan, F. M., Blythe, L. S., McLeod, C. L. & Davidson, J. P.
1324 (2013). Experimental simulation of magma–carbonate interaction beneath Mt. Vesuvius, Italy.
1325 *Contributions to Mineralogy and Petrology* **166**, 1335–1353.
- 1326 Jolis, E., Troll, V., Harris, C., Freda, C., Gaeta, M., Orsi, G. & Siebe, C. (2015). Skarn xenolith record
1327 crustal CO_2 liberation during Pompeii and Pollena eruptions, Vesuvius volcanic system, central Italy.
1328 *Chemical Geology* **415**, 17–36.
- 1329 Kerinec, F. (1982). Le Mérapî, volcan actif d'arc insulaire (Java): Pétrographie et géochimie des
1330 matériaux solides; implications géotectoniques (PhD thesis). Université Paris-Sud, Orsay, France.
- 1331 Kilgour, G. N., Saunders, K. E., Blundy, J. D., Cashman, K. V., Scott, B. J. & Miller, C. A. (2014).
1332 Timescales of magmatic processes at Ruapehu volcano from diffusion chronometry and their comparison
1333 to monitoring data. *Journal of Volcanology and Geothermal Research* **288**, 62–75.
- 1334 Kokh, M. A., Akinfiev, N. N., Pokrovski, G. S., Salvi, S. & Guillaume, D. (2017). The role of carbon
1335 dioxide in the transport and fractionation of metals by geological fluids. *Geochimica et Cosmochimica*
1336 *Acta* **197**, 433–466.
- 1337 Komorowski, J.-C., Jenkins, S., Baxter, P. J., Picquout, A., Lavigne, F., Charbonnier, S., Gertisser, R.,
1338 Preece, K., Cholik, N. & Budi-Santoso, A. (2013). Paroxysmal dome explosion during the Merapi 2010
1339 eruption: processes and facies relationships of associated high-energy pyroclastic density currents.
1340 *Journal of Volcanology and Geothermal Research* **261**, 260–294.

- 1341 Kouchi, A., Sugawara, Y., Kashima, K. & Sunagawa, I. (1983). Laboratory growth of sector zoned
1342 clinopyroxenes in the system $\text{CaMgSi}_2\text{O}_6\text{-CaTiAl}_2\text{O}_6$. *Contributions to Mineralogy and Petrology* **83**,
1343 177–184.
- 1344 Landtwing, M. R., Pettke, T., Halter, W. E., Heinrich, C. A., Redmond, P. B., Einaudi, M. T. & Kunze, K.
1345 (2005). Copper deposition during quartz dissolution by cooling magmatic–hydrothermal fluids: the
1346 Bingham porphyry. *Earth and Planetary Science Letters* **235**, 229–243.
- 1347 Lindsley, D. H. (1983). Pyroxene thermometry. *American Mineralogist* **68**, 477–493.
- 1348 Luhr, J. F. (2008). Primary igneous anhydrite: Progress since its recognition in the 1982 El Chichón
1349 trachyandesite. *Journal of Volcanology and Geothermal Research* **175**, 394–407.
- 1350 Mason, E., Edmonds, M. & Turchyn, A. V. (2017). Remobilization of crustal carbon may dominate
1351 volcanic arc emissions. *Science* **357**, 290–294.
- 1352 Matthews, S., Marquillas, R., Kemp, A., Grange, F. & Gardeweg, M. (1996). Active skarn formation
1353 beneath Lascar Volcano, northern Chile: a petrographic and geochemical study of xenoliths in eruption
1354 products. *Journal of Metamorphic Geology* **14**, 509–530.
- 1355 Mavrogenes, J. & Blundy, J. (2017). Crustal sequestration of magmatic sulfur dioxide. *Geology* **45**, 211–
1356 214.
- 1357 Meinert, L. D. (1992). Skarns and skarn deposits. *Geoscience Canada* **19**, 145–162.
- 1358 Meinert, L. D., Dipple, G. M. & Nicolescu, S. (2005). World skarn deposits. In: Hedenquist, J. W.,
1359 Thompson, J. F. H., Goldfarb, R. J. & Richards, J. P. (eds.) *Economic Geology One Hundredth*
1360 *Anniversary Volume*. Littleton, Colorado, pp. 299–336.
- 1361 Melluso, L., Conticelli, S., D'Antonio, M., Mirco, N. P. & Saccani, E. (2003). Petrology and mineralogy
1362 of wollastonite-and melilite-bearing paralavas from the Central Apennines, Italy. *American Mineralogist*
1363 **88**, 1287–1299.
- 1364 Mollo, S., Blundy, J. D., Giacomoni, P., Nazzari, M., Scarlato, P., Coltorti, M., Langone, A. &
1365 Andronico, D. (2017). Clinopyroxene-melt element partitioning during interaction between trachybasaltic
1366 magma and siliceous crust: Clues from quartzite enclaves at Mt. Etna volcano. *Lithos* **284**, 447–461.
- 1367 Mollo, S., Gaeta, M., Freda, C., Di Rocco, T., Misiti, V. & Scarlato, P. (2010). Carbonate assimilation in
1368 magmas: a reappraisal based on experimental petrology. *Lithos* **114**, 503–514.
- 1369 Mollo, S., Putirka, K., Iezzi, G., Del Gaudio, P. & Scarlato, P. (2011). Plagioclase–melt (dis) equilibrium
1370 due to cooling dynamics: implications for thermometry, barometry and hygrometry. *Lithos* **125**, 221–235.
- 1371 Mollo, S., Heap, M. J., Iezzi, G., Hess, K. U., Scarlato, P. & Dingwell, D. B. (2012). Volcanic edifice
1372 weakening via decarbonation: A self-limiting process? *Geophysical Research Letters*, **39**, L15307.
- 1373 Mollo, S., Putirka, K., Misiti, V., Soligo, M. & Scarlato, P. (2013). A new test for equilibrium based on
1374 clinopyroxene–melt pairs: clues on the solidification temperatures of Etnean alkaline melts at post-
1375 eruptive conditions. *Chemical Geology* **352**, 92–100.

- 1376 Mollo, S. & Vona, A. (2014). The geochemical evolution of clinopyroxene in the Roman Province: A
1377 window on decarbonation from wall-rocks to magma. *Lithos* **192**, 1–7.
- 1378 Morimoto, N. (1988). Nomenclature of pyroxenes. *Mineralogy and Petrology* **39**, 55–76.
- 1379 Muhling, J.R. & Griffin, B.J. (1991). On recasting garnet analyses into end-member molecules—revisited
1380 short note. *Computers & Geosciences* **17**, 161–170.
- 1381 Nadeau, O., Stix, J. & Williams-Jones, A. E. (2013a). The behavior of Cu, Zn and Pb during magmatic–
1382 hydrothermal activity at Merapi volcano, Indonesia. *Chemical Geology* **342**, 167–179.
- 1383 Nadeau, O., Williams-Jones, A. E. & Stix, J. (2013b). Magmatic-hydrothermal evolution and
1384 devolatilization beneath Merapi volcano, Indonesia. *Journal of Volcanology and Geothermal Research*
1385 **261**, 50–68.
- 1386 Nadeau, O., Williams-Jones, A.E. & Stix, J. (2010). Sulphide magma as a source of metals in arc-related
1387 magmatic hydrothermal ore fluids. *Nature Geoscience* **3**, 501–505.
- 1388 Nakamura, M. & Shimakita, S. (1998). Dissolution origin and syn-entrapment compositional change of
1389 melt inclusion in plagioclase. *Earth and Planetary Science Letters* **161**, 119–133.
- 1390 Neave, D. A. & Putirka, K. (2017). A new clinopyroxene-liquid barometer, and implications for magma
1391 storage pressures under Icelandic rift zones. *American Mineralogist* **102**, 777–794.
- 1392 Newhall, C., Bronto, S., Alloway, B., Banks, N., Bahar, I., Marmol, M. D., Hadisantono, R., Holcomb,
1393 R., McGeehin, J. & Miksic, J. (2000). 10,000 Years of explosive eruptions of Merapi Volcano, Central
1394 Java: archaeological and modern implications. *Journal of Volcanology and Geothermal Research* **100**, 9–
1395 50.
- 1396 Nicholls, I. (1971). Calcareous inclusions in lavas and agglomerates of Santorini volcano. *Contributions*
1397 *to Mineralogy and Petrology* **30**, 261–276.
- 1398 Nielsen, R. L. (2011). The effects of re-homogenization on plagioclase hosted melt inclusions.
1399 *Geochemistry, Geophysics, Geosystems* **12**, Q0AC17.
- 1400 Orlando, A., D’Orazio, M., Armienti, P. & Borrini, D. (2008). Experimental determination of plagioclase
1401 and clinopyroxene crystal growth rates in an anhydrous trachybasalt from Mt Etna (Italy). *European*
1402 *Journal of Mineralogy* **20**, 653–664.
- 1403 Parat, F., Holtz, F. & Streck, M. J. (2011). Sulfur-bearing magmatic accessory minerals. *Reviews in*
1404 *Mineralogy and Geochemistry* **73**, 285–314.
- 1405 Pascal, M.-L., Di Muro, A., Fonteilles, M. & Principe, C. (2009). Zirconolite and calzirtite in banded
1406 forsterite-spinel-calcite skarn ejecta from the 1631 eruption of Vesuvius: inferences for magma-wallrock
1407 interactions. *Mineralogical Magazine* **73**, 333–356.
- 1408 Pascal, M.-L., Katona, I., Fonteilles, M. & Verkaeren, J. (2005). Relics of high-temperature
1409 clinopyroxene on the join di-cats with up to 72 mol.% Ca(Al,Fe³)AlSiO₆ in the skarns of Ciclova and
1410 Magureaua Vatei, Carpathians, Romania. *The Canadian Mineralogist* **43**, 857–881.

- 1411 Povoden, E., Horacek, M. & Abart, R. (2002). Contact metamorphism of siliceous dolomite and impure
1412 limestones from the Werfen formation in the eastern Monzoni contact aureole. *Mineralogy and Petrology*
1413 **76**, 99–120.
- 1414 Preece, K. (2014). Transitions between effusive and explosive activity at Merapi volcano, Indonesia: a
1415 volcanological and petrological study of the 2006 and 2010 eruptions. (PhD thesis). University of East
1416 Anglia, Norwich, UK.
- 1417 Preece, K., Gertisser, R., Barclay, J., Berlo, K. & Herd, R. A. (2014). Pre-and syn-eruptive degassing and
1418 crystallisation processes of the 2010 and 2006 eruptions of Merapi volcano, Indonesia. *Contributions to*
1419 *Mineralogy and Petrology* **168**, 1–25.
- 1420 Preece, K., Gertisser, R., Barclay, J., Charbonnier, S. J., Komorowski, J.-C. & Herd, R. A. (2016).
1421 Transitions between explosive and effusive phases during the cataclysmic 2010 eruption of Merapi
1422 volcano, Java, Indonesia. *Bulletin of Volcanology* **78**, 54.
- 1423 Putirka, K. (2008). Thermometers and barometers for volcanic systems. *Reviews in Mineralogy and*
1424 *Geochemistry* **69**, 61–120.
- 1425 Putirka, K. (1999). Clinopyroxene+liquid equilibria to 100 kbar and 2450 K. *Contributions to Mineralogy*
1426 *and Petrology* **135**, 151–163.
- 1427 Putirka, K., Johnson, M., Kinzler, R., Longhi, J. & Walker, D. (1996). Thermobarometry of mafic
1428 igneous rocks based on clinopyroxene-liquid equilibria, 0-30 kbar. *Contributions to Mineralogy and*
1429 *Petrology* **123**, 92–108.
- 1430 Reagan, M., Handley, H., Gertisser, R., Turner, M., Berlo, K. & Preece, K. (2017). U-series evidence for
1431 ongoing skarnification beneath Merapi Volcano, Indonesia, in: IAVCEI 2017 Conference Abstracts.
1432 Portland, Oregon, USA, p. 883.
- 1433 Roedder, E., 1984. *Fluid Inclusions*. Reviews in Mineralogy volume 12. Mineralogical Society of
1434 America, Washington.
- 1435 Rutstein, M. S. (1971). Re-examination of the wollastonite-hedenbergite (CaSiO₃-CaFeSi₂O₆) equilibria.
1436 *American Mineralogist* **56**, 2040–2052.
- 1437 Rutstein, M. S. & White, W. B. (1971). Vibrational spectra of high-calcium pyroxenes and pyroxenoids.
1438 *American Mineralogist* **56**, 877-887.
- 1439 Schwarzkopf, L., Schmincke, H.-U. & Troll, V. (2001). Pseudotachylite on impact marks of block
1440 surfaces in block-and-ash flows at Merapi volcano, Central Java, Indonesia. *International Journal of*
1441 *Earth Sciences* **90**, 769–775.
- 1442 Sillitoe, R. H. (2010). Porphyry copper systems. *Economic Geology* **105**, 3–41.
- 1443 Simakin, A. G., Salova, T. P. & Armienti, P. (2003). Kinetics of clinopyroxene growth from a hydrous
1444 hawaiite melt. *Geochemistry International* **41**, 1165–1175.
- 1445 Simakin, A., Salova, T. & Bondarenko, G. (2012). Experimental study of magmatic melt oxidation by
1446 CO₂. *Petrology* **20**, 593–606.

- 1447 Smyth, H., Hall, R., Hamilton, J. & Kinny, P. (2005). East Java: Cenozoic basins, volcanoes and ancient
1448 basement.
- 1449 Sobolev, V. N., McCammon, C. A., Taylor, L. A., Snyder, G. A. & Sobolev, N. V. (1999). Precise
1450 Moessbauer milliprobe determination of ferric iron in rock-forming minerals and limitations of electron
1451 microprobe analysis. *American Mineralogist* **84**, 78-85.
- 1452 Span, R. & Wagner, W. (1996). A new equation of state for carbon dioxide covering the fluid region from
1453 the triple-point temperature to 1100 K at pressures up to 800 MPa. *Journal of Physical and Chemical*
1454 *Reference Data* **25**, 1509–1596.
- 1455 Spandler, C., Martin, L.H. & Pettke, T. (2012). Carbonate assimilation during magma evolution at
1456 Nisyros (Greece), South Aegean Arc: Evidence from clinopyroxene xenoliths. *Lithos* **146**, 18–33.
- 1457 Sterner, S. M. & Pitzer, K. S. (1994). An equation of state for carbon dioxide valid from zero to extreme
1458 pressures. *Contributions to Mineralogy and Petrology* **117**, 362–374.
- 1459 Sugawara, T. (2001). Ferric iron partitioning between plagioclase and silicate liquid: thermodynamics and
1460 petrological applications. *Contributions to Mineralogy and Petrology* **141**, 659–686.
- 1461 Sun, W., Liang, H., Ling, M., Zhan, M., Ding, X., Zhang, H., Yang, X., Li, Y., Ireland, T. R., Wei, Q. &
1462 Fan, W. (2013). The link between reduced porphyry copper deposits and oxidized magmas. *Geochimica*
1463 *et Cosmochimica Acta* **103**, 263–275.
- 1464 Surono, M., Jousset, P., Pallister, J., Boichu, M., Fabrizia, M., Buongiorno, A. B., Rodriguez, F. C.,
1465 Andreastuti, S., Prata, F. & Schneider, D. (2012). The 2010 explosive eruption of Java's Merapi volcano-
1466 a '100-year' event. *Journal of Volcanology and Geothermal Research* **241–242**, 121–135.
- 1467 Tamic, N., Behrens, H. & Holtz, F. (2001). The solubility of H₂O and CO₂ in rhyolitic melts in
1468 equilibrium with a mixed CO₂-H₂O fluid phase. *Chemical Geology*, **174**, 333-347.
- 1469 Tracy, R. J. & Frost, B. R. (1991). Phase equilibria and thermobarometry of calcareous, ultramafic and mafic rocks, and iron
1470 formations. *Reviews in Mineralogy and Geochemistry* **26**, 207–289.
- 1471 Treiman, A. H. & Essene, E. J. (1983). Phase equilibria in the system CaO-SiO₂-CO₂. *American Journal*
1472 *of Science* **283**, 97–120.
- 1473 Troll, V. R., Deegan, F. M., Jolis, E. M., Harris, C., Chadwick, J. P., Gertisser, R., Schwarzkopf, L. M.,
1474 Borisova, A. Y., Bindeman, I. N. & Sumarti, S. (2013). Magmatic differentiation processes at Merapi
1475 Volcano: inclusion petrology and oxygen isotopes. *Journal of Volcanology and Geothermal Research*
1476 **261**, 38–49.
- 1477 Troll, V. R., Hilton, D. R., Jolis, E. M., Chadwick, J. P., Blythe, L. S., Deegan, F. M., Schwarzkopf, L. M.
1478 & Zimmer, M. (2012). Crustal CO₂ liberation during the 2006 eruption and earthquake events at Merapi
1479 volcano, Indonesia. *Geophysical Research Letters* **39**, L11302.
- 1480 Tuttle, O. F. & Harker, R. I. (1957). Synthesis of spurrite and the reaction wollastonite+calcite ⇌
1481 spurrite+carbon dioxide. *American Journal of Science* **255**, 226–234.
- 1482 van Bemmelen, R. W. (1949). *The Geology of Indonesia*. Government Printing Office, The Hague.

- 1483 van Hinsberg, V. J., Berlo, K., Migdisov, A. A. & Williams-Jones, A. E. (2016). CO₂-fluxing collapses
1484 metal mobility in magmatic vapour. *Geochemical Perspectives Letters* **2**, 169-177.
- 1485 Voight, B., Constantine, E. K., Siswoidjoyo, S. & Torley, R. (2000). Historical eruptions of Merapi
1486 volcano, central Java, Indonesia, 1768–1998. *Journal of Volcanology and Geothermal Research* **100**, 69–
1487 138.
- 1488 Wenzel, T., Baumgartner, L. P., Brüggmann, G. E., Konnikov, E. G. & Kislov, E. V.(2002). Partial
1489 melting and assimilation of dolomitic xenoliths by mafic magma: the Ioko-Dovyren intrusion (North
1490 Baikal Region, Russia). *Journal of Petrology* **43**, 2049–2074.
- 1491 Whitaker, M. L., Nekvasil, H., Lindsley, D. H. & Di Francesco, N. J. (2007). The Role of Pressure in
1492 Producing Compositional Diversity in Intraplate Basaltic Magmas. *Journal of Petrology* **48**, 365–393.
- 1493 Whitley, S., Gertisser, R., Halama, R., Preece, K., Troll, V. R. & Deegan, F. M. (2019). Crustal CO₂
1494 contribution to subduction zone degassing recorded through calc-silicate xenoliths in arc lavas. *Scientific*
1495 *Reports* **9**, 8803.
- 1496 Wölbern, I. & Rümpker, G. (2016). Crustal thickness beneath Central and East Java (Indonesia) inferred
1497 from P receiver functions. *Journal of Asian Earth Sciences* **115**, 69–79.
- 1498 Wyllie, P. J. & Haas Jr, J. L. (1965). The system CaO-SiO₂-CO₂-H₂O: 1. Melting relationships with
1499 excess vapor at 1 kilobar pressure. *Geochimica et Cosmochimica Acta* **29**, 871–892.
- 1500 Zanon, V. & Nikogosian, I. (2004). Evidence of crustal melting events below the island of Salina
1501 (Aeolian arc, southern Italy). *Geological Magazine* **141**, 525–540.
- 1502 Zarayskiy, G. P., Zharikov, V. A., Stoyanovskaya, F. M. & Balashov, V. N. (1987). The experimental
1503 study of bimetasomatic skarn formation. *International Geology Review* **29**, 629–758.
- 1504 Zharikov, V. A. (1969). High temperature mineral equilibria in the system CaO-SiO₂-CO₂. *Geochemistry*
1505 *International* **6**, 853–869.

1507 **FIGURES**

1508

1509 *Fig. 1: Zoning in sample MX1 (thin section) and idealised diagram for zoning patterns in the magmatic*
 1510 *skarn xenoliths. Highlighted zones (a) and (d) correspond to the respective panels in Fig. 2. See Table 1*
 1511 *for all mineral abbreviations used. Gls: interstitial Ca-rich glass.*

1512

1513 *Fig. 2: Examples of the respective zones in magmatic skarn xenoliths. A) Host lava contact and zones R1*
 1514 *to R4. Note the progressive darkening of the clinopyroxene colour due to changing composition to iron*
 1515 *enrichment. Sample MX1. B) Normally zoned diopside-hedenbergite clinopyroxene within glass dominant*
 1516 *zone R4. Also present are plagioclase microlites and wollastonite. Sample CS2. C) Wollastonite-dominant*
 1517 *xenolith core with vesicles and accessory calcite. Sample MX5. D) Zone R3b, showing garnet + CaTs*
 1518 *clinopyroxene formation where there is no glass zone R4 between the core and zone R2. Sample MX1. See*
 1519 *Table 1 for mineral abbreviations. Gls: interstitial Ca-rich glass.*

1520

1521 *Fig. 3: Magmatic skarn accessory minerals and melt inclusions. All images are from sample MX1, apart*
 1522 *from panels E and G, which are from sample CS16. A-B) Accessory gehlenite, fluorite, calcite and the*
 1523 *wadalite-like mineral in the xenolith core. C-G) Examples of wollastonite, clinopyroxene and*
 1524 *plagioclase-hosted melt inclusions, showing variable abundance and textural forms. Mineral*
 1525 *abbreviations as in Table 1. Gls: interstitial Ca-rich glass.*

1526

1527 *Fig. 4: Typical textures in exoskarn xenoliths. A) CaTs-cpx + Wo + An + Grs in exoskarn type A xenolith*
 1528 *MX99-5s. B) Large residual calcite crystals in exoskarn type A xenolith CS11. Expanded image shows the*
 1529 *complex decarbonation textures and reactions occurring influenced by a F-rich fluid. A Ca-Si-O phase is*
 1530 *present with low analytical totals (~65 wt%). C) Exoskarn B xenolith MX99-3s shows a unique*
 1531 *assemblage of spinel, gehlenite, CaTs-cpx, grossular, with accessory wollastonite and anorthite. Spinel is*
 1532 *rimmed by gehlenite followed by CaTs-cpx. For mineral abbreviations, see Table 1.*

1533

1534 Fig. 5: Xenolith whole-rock geochemistry (calculated from mineral modes and mineral chemistry,
1535 corrected for mineral densities using data from Deer et al. (1997) and the Rock-Maker spreadsheet
1536 (Büttner, 2012)). A) Profiles through the distinct zones of two magmatic xenoliths. B) Calculated whole-
1537 rock compositions of bulk xenoliths compared to published lava and xenolith data. Published volcanic
1538 whole-rock data are from Nadeau et al. (2013b), Borisova et al. (2013), Costa et al. (2013), Innocenti et
1539 al. (2013) and the GEOROC database (<http://georoc.mpch-mainz.gwdg.de/georoc/>, accessed 03/2019).
1540 Published Merapi calc-silicate xenoliths from Chadwick et al. (2007).

1541
1542 Fig. 6: Merapi xenolith and magmatic feldspar compositions. A) Anorthite content histograms showing
1543 (left) published data from Merapi lavas (grey), enclaves (dark blue) and plutonic xenoliths (green) for
1544 comparison with xenolith and host lava feldspar data (right, key below). B) An vs FeO plot showing the
1545 different xenolith plagioclase compositions compared to Merapi lava plagioclase. Ellipse of xenolith and
1546 xenocryst plagioclase compositions from Chadwick et al. (2007). Notably, plagioclase from zones R1 and
1547 R2 overlaps with the lava compositions, although they are formed from magma-carbonate interaction.
1548 Published lava feldspar data from Gertisser (2001), Preece (2014) and Erdmann et al. (2016). Enclave
1549 and plutonic xenolith data from Chadwick et al. (2013).

1550
1551 Fig. 7: Clinopyroxene compositions. A) Fe^{3+}/Fe_{total} versus Al^{IV} plot showing a good correlation
1552 ($R^2=0.88$). The fassaitic boundary ($Al^{IV} \geq 0.25$) is from Deer et al. (1997). B) Ti versus Al^{IV} plot. Exoskarn
1553 clinopyroxene plot distinct from magmatic skarn clinopyroxenes. Zone 3b plots with the exoskarn data,
1554 showing a metamorphic character to this zone. C) Ternary Wo-En-Fs components for magmatic skarn
1555 clinopyroxene. Two partial ternary diagrams shown for clarity, with ternary location shown on inset
1556 figure. Clinopyroxenes in zones 1 to 3 progressively become more Wo-rich, diverging from magmatic
1557 compositions. The remaining zones follow the Di-Hd join or plot above due to the large amount of Al. D)
1558 Partial ternary Wo-En-Fs components for exoskarn clinopyroxenes. E) Al and Mg# traverse along a
1559 magmatic skarn clinopyroxene (sample CS16). Al and Mg-rich cores progressively grade to low Al-high
1560 Fe compositions. F) Al and Mg# traverse in magmatic skarn clinopyroxene from sample CS2. These
1561 crystals do not have an Al-rich core, and compositions instead follow the Di-Hd join. Published data
1562 sources as in Fig. 6 and additionally Deegan et al. (2016b).

1563

1564

1565

1566 *Fig. 8: Additional rock-forming mineral compositions. A) Wollastonite and ferrobustamite. B) Garnet. C)*
1567 *Melilite. Note the different ternary scales for each plot. Arrows indicate truncated scales. Mineral*
1568 *abbreviations as in Table 1.*

1569

1570 *Fig. 9: Interstitial and melt inclusion glass compositions. All values are normalised to 100 wt% volatile*
1571 *free. Published data for whole rock, glass and melt inclusions at Merapi are shown for comparison.*
1572 *Published data from Nadeau et al. (2013b), Borisova et al. (2013), Costa et al. (2013), Innocenti et al.*
1573 *(2013) and the GEOROC database (accessed 03/2019). Arrows show the effect of adding 10% calcite,*
1574 *and subtracting 10% clinopyroxene, wollastonite or plagioclase. Mineral abbreviations as in Table 1.*

1575

1576 *Fig. 10: A) Box plots of $KD_{Fe-Mg}^{cpx-melt}$ values from carbonate assimilation experiments. Black circles*
1577 *represent outliers calculated as 1.5 x interquartile range from the third quartile. Experiments with*
1578 *carbonate added have a general increase in $KD_{Fe-Mg}^{cpx-melt}$ values. Experiments by Carter and Dasgupta*
1579 *(2016) and Carter and Dasgupta (2018) use more evolved andesite and dacite compositions, compared to*
1580 *the remaining basaltic experiments, which were less affected by carbonate interaction. The extremely*
1581 *high values from Mollo and Vona (2014) are likely the result of very high experimental fO_2 conditions (up*
1582 *to air), which would strongly affect Fe^{2+}/Fe^{3+} partitioning between clinopyroxene and melt. B)*
1583 *Comparison between measured clinopyroxene Diopside-Hedenbergite (DiHd) components and predicted*
1584 *ones, using the iterative approach of Neave and Putirka (2017). Light grey data are calculated from*
1585 *clinopyroxenes in the Library of Experimental Phase Relations (LEPR, Hirschmann et al., 2008)*
1586 *database.*

1587

1588 *Fig. 11: Stacked histogram results of thermometry estimates for the magmatic skarn xenoliths and host*
1589 *lava glasses using equation 34 of Putirka (2008). Xenolith glasses produce temperatures of $829 \pm 45^\circ C$*
1590 *($n=89$). Melt inclusions have a slightly higher temperature of $876 \pm 49^\circ C$ ($n=89$). These temperatures*
1591 *are slightly below the thermometry estimates for published lava glass analyses, at $937 \pm 43^\circ C$. Published*
1592 *glass data are from Preece et al. (2014) and Erdmann et al. (2016).*

1593

1594

1595

1596 *Fig. 12: Theriak-Domino (de Capitani and Petrakakis, 2010) T-XCO₂ modelling of exoskarn xenoliths.*
1597 *Isobaric sections at 100 MPa. Green contours show the gehlenite mole fraction. Red contours show the*
1598 *CaTs mole fractions. The exoskarn A xenolith (MX99-5s) formed in a narrow temperature range between*
1599 *~900 to 910°C, and XCO₂ < 0.5. The exoskarn B xenolith (MX99-3s) mineral assemblage records*
1600 *temperatures between 680 and 860°C at a XCO₂ < ~0.5. Abbreviations as in Table 1. Additional*
1601 *abbreviations: Grt - garnet (andradite-grossular), Me - meionite, Ol – olivine.*

1602

1603 *Fig. 13: Clinopyroxene-only single crystal oxybarometer model testing. Experiments used for the*
1604 *calibration of the new oxybarometer are highlighted (Feig et al., 2006, 2010; Berndt et al., 2005;*
1605 *Whitaker et al., 2007; Mollo and Vona, 2014). Sugawara (2001)'s experiments which cover 13 log units,*
1606 *and the results of applying the oxybarometers to the filtered Library of Experimental Phase Relations*
1607 *(LEPR Hirschmann et al., 2008) are also shown. A) Results of the Cortés et al. (2006) oxybarometer*
1608 *applied to the experimental clinopyroxenes. B) Results of the Simakin et al. (2012) oxybarometer applied*
1609 *to the experimental clinopyroxenes. C) Results of the model calibrated in this study applied to the*
1610 *experimental clinopyroxenes. The model error is shown in the top left.*

1611

1612 *Fig. 14: fO₂ estimates from clinopyroxenes across all zones and traverses. A) Violin density plots of*
1613 *oxygen fugacity estimates for xenolith clinopyroxenes. The model error has been applied as the*
1614 *smoothing bandwidth. The light grey field shows published estimates of Merapi magma fO₂ from other*
1615 *independent methods (Δ NNO -0.2 to 1.6. Gertisser, 2001; Erdmann et al., 2014). Application of our*
1616 *model to the literature clinopyroxene dataset detailed in Fig. 7 is shown for comparison to past literature*
1617 *estimates. The solid dashed line is the magnetite-hematite oxygen fugacity buffer. The results show*
1618 *xenolith rims (zones R1-3) formed in fO₂ similar to magmatic conditions, whilst the cores and exoskarn*
1619 *xenoliths formed at much higher fO₂, up to that of air. B) Results of application of the oxybarometer to*
1620 *the core to rim traverse of the same clinopyroxene from sample CS16 as shown in Fig. 7E. The results*
1621 *show an initial period of high fO₂ during initial clinopyroxene formation and vigorous carbonate-magma*
1622 *interaction, then a progressive decline as the carbonate-contaminated melt precipitates mineral phases*
1623 *and CO₂ migrates from the reaction zone.*

1624

1625 *Fig. 15: Summary of the processes occurring during magma carbonate interaction at Merapi. Carbonate*
1626 *is rapidly digested forming a Ca-rich contaminated melt, from which wollastonite and other phases*
1627 *precipitate, forming the magmatic skarn xenoliths. Proximal to the magmatic melt, clinopyroxene and*
1628 *plagioclase form from Ca transfer to the melt from the carbonate. The abundance of melt in the xenoliths*
1629 *allows disaggregation and disperses xenolith crystals into the magma (e.g. Deegan et al., 2010). The*
1630 *magmatic volatile phase (MVP c.f. Nadeau et al., 2010; Preece et al., 2014) infiltrates the xenoliths*
1631 *forming rare halogen and sulphur-bearing minerals. At the wall-rock contact, abundant clinopyroxene*
1632 *forms, partially insulating the carbonate and skarn. Magma-derived elements are transferred to the wall-*
1633 *rock, influenced by the increasing oxygen fugacity caused by CO₂ flushing, forming the exoskarn*
1634 *mineralogy. Regions of main magma crystallisation from Chadwick et al. (2013), Preece et al. (2014) and*
1635 *Erdmann et al. (2016). Moho depth from Wölbern and Rumpker (2016). Description of the lower crust*
1636 *from van Bemmelen (1949).*

1637

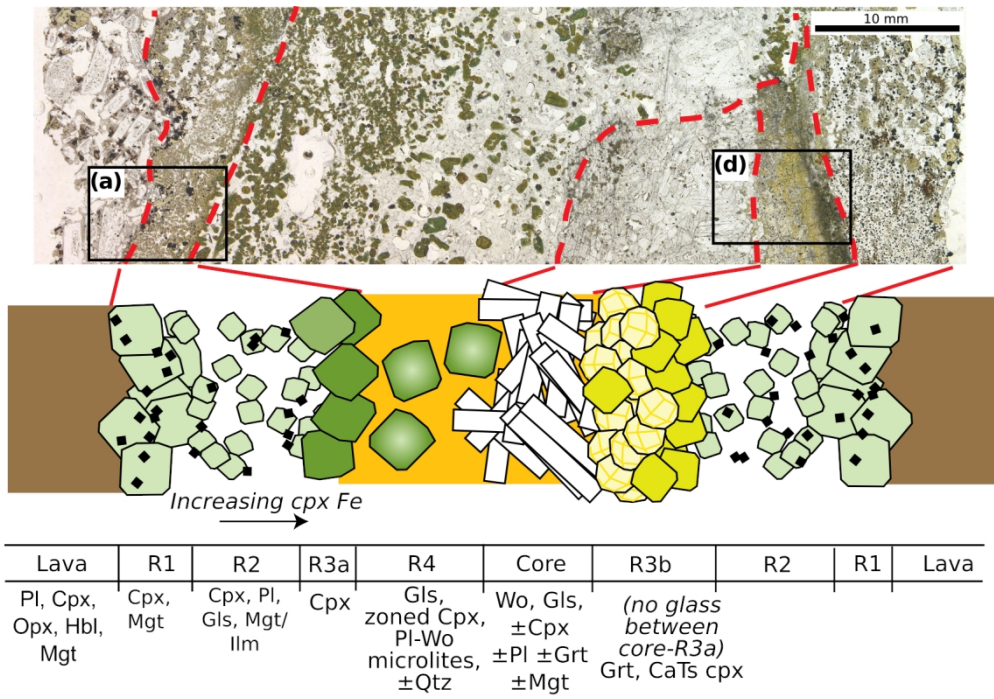


Fig. 1: Zoning in sample MX1 (thin section) and idealised diagram for zoning patterns in the magmatic skarn xenoliths. Highlighted zones A and D correspond to the respective panels in Fig. 2. See Table 1 for all mineral abbreviations used.

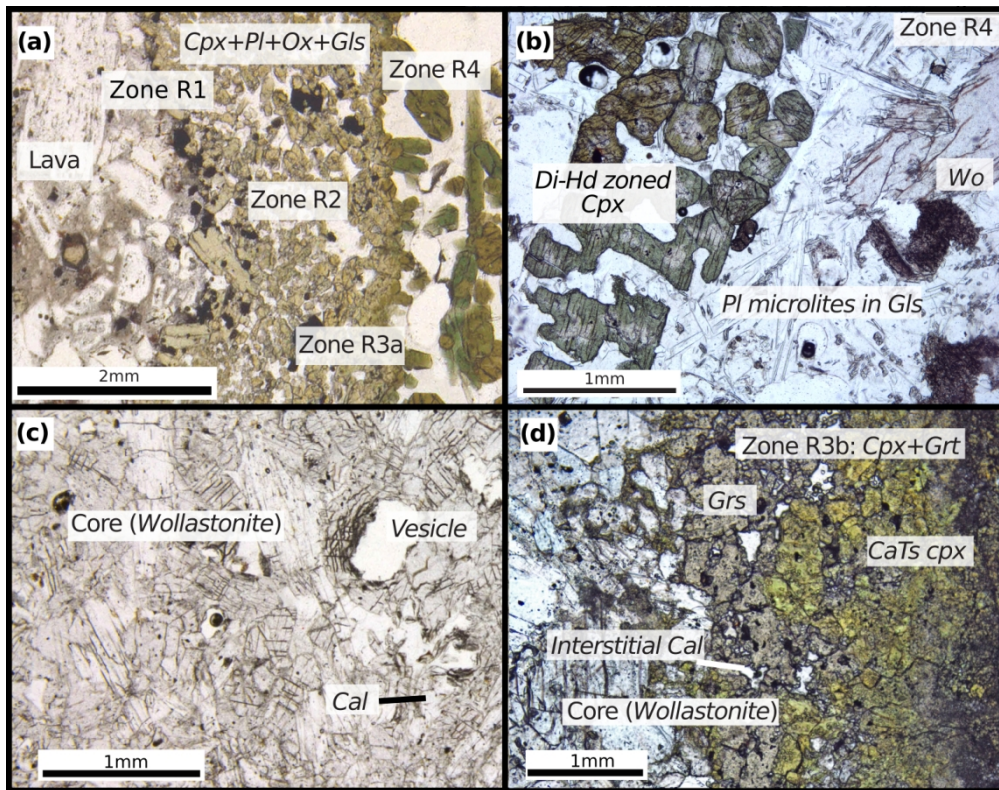


Fig. 2: Examples of the respective zones in magmatic skarn xenoliths. A) Host lava contact and zones R1 to R4. Note the progressive darkening of the clinopyroxene colour due to changing composition to iron enrichment. Sample MX1. B) Normally zoned diopside-hedenbergite clinopyroxene within glass dominant zone R4. Also present are plagioclase microlites and wollastonite. Sample CS2. C) Wollastonite-dominant xenolith core with vesicles and accessory calcite. Sample MX5. D) Zone R3b, showing garnet + CaTs clinopyroxene formation where there is no glass zone R4 between the core and zone R2. Sample MX1. See Table 1 for mineral abbreviations.

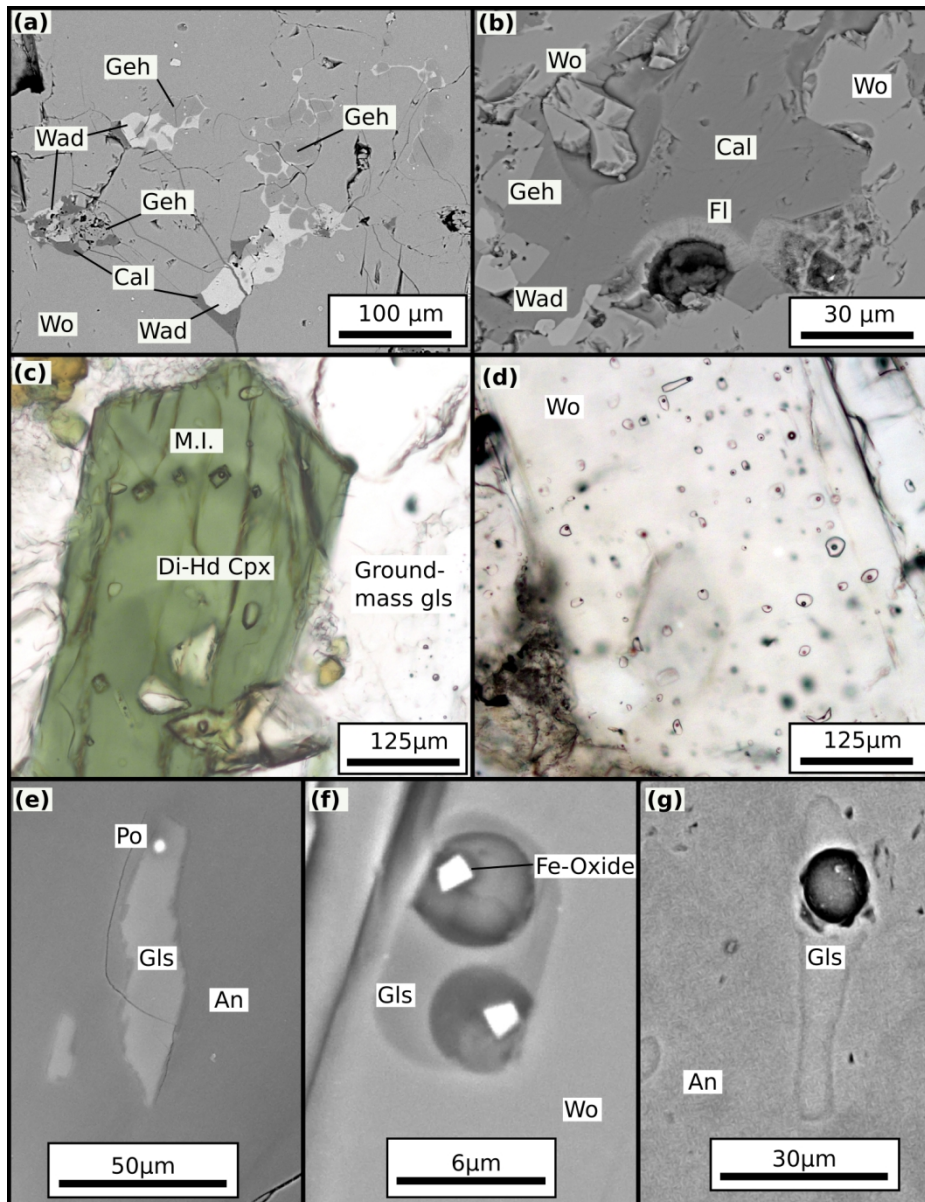


Fig. 3: Magmatic skarn accessory minerals and melt inclusions. All images are from sample MX1, apart from panels E and G, which are from sample CS16. A-B) Accessory gehlenite, fluorite, calcite and the wadalite-like mineral in the xenolith core. C-G) Examples of wollastonite, clinopyroxene and plagioclase-hosted melt inclusions, showing variable abundance and textural forms. Abbreviations as in Table 1

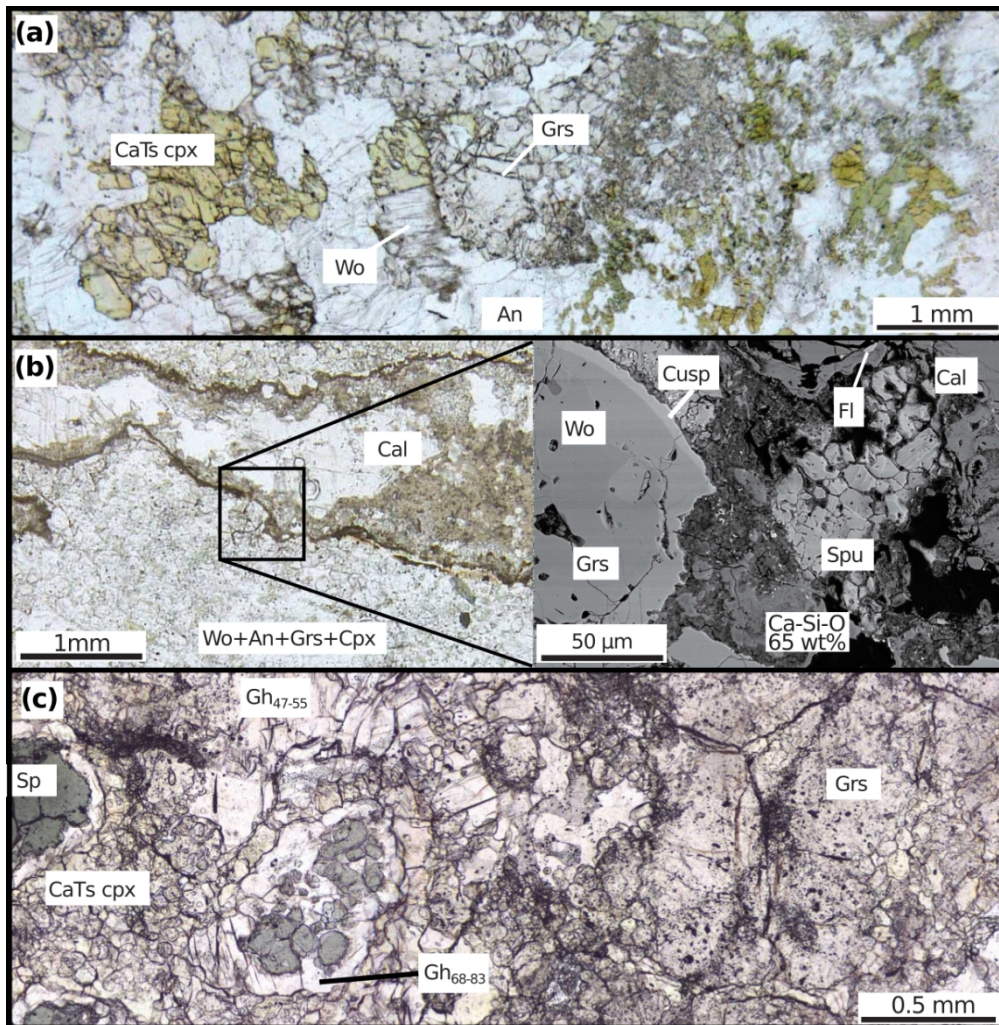


Fig. 4: Typical textures in exoskarn xenoliths. A) CaTs-cpx + Wo + An + Grs in exoskarn type A xenolith MX99-5s. B) Large residual calcite crystals in exoskarn type A xenolith CS11. Expanded image shows the complex decarbonation textures and reactions occurring influenced by a F-rich fluid. A Ca-Si-O phase is present with low analytical totals (~65 wt%). C) Exoskarn B xenolith MX99-3s shows a unique assemblage of spinel, gehlenite, CaTs-cpx, grossular, with accessory wollastonite and anorthite. Spinel is rimmed by gehlenite followed by CaTs-cpx. For mineral abbreviations, see Table 1.

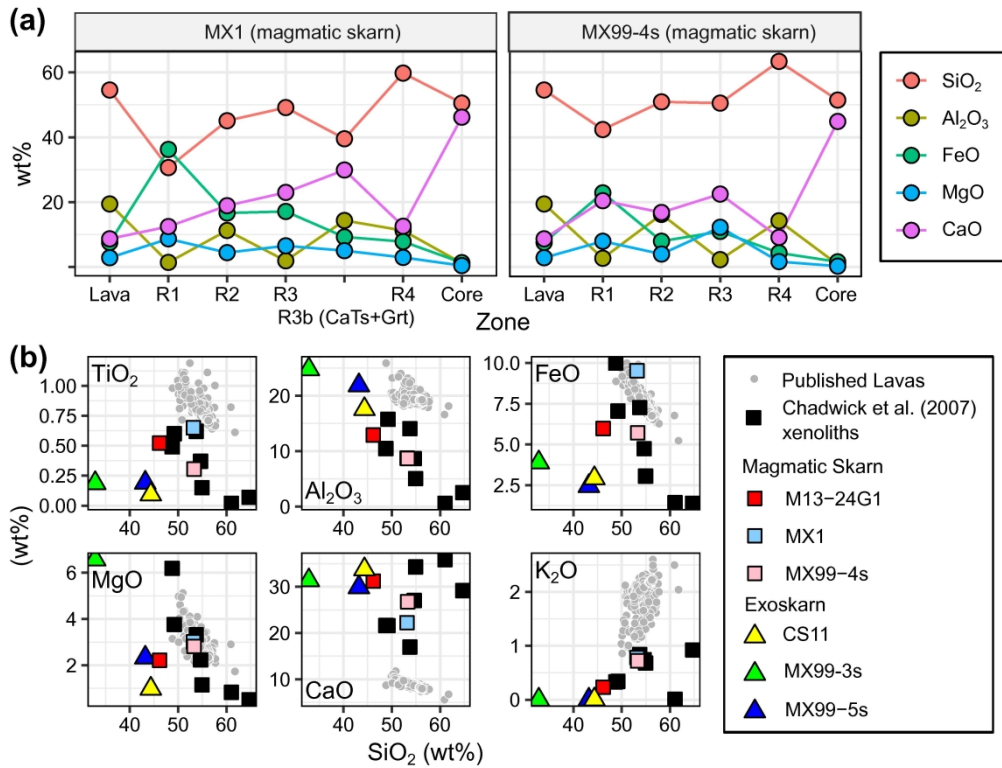


Fig. 5: Xenolith whole-rock geochemistry (calculated from mineral modes and mineral chemistry, corrected for mineral densities using data from Deer et al. (1997) and the Rock-Maker spreadsheet (Büttner, 2012)). A) Profiles through the distinct zones of two magmatic xenoliths. B) Calculated whole-rock compositions of bulk xenoliths compared to published lava and xenolith data. Published volcanic whole-rock data are from Nadeau et al. (2013b), Borisova et al. (2013), Costa et al. (2013), Innocenti et al. (2013) and the GEOROC database (<http://georoc.mpch-mainz.gwdg.de/georoc/>, accessed 03/2019). Published Merapi calc-silicate xenoliths from Chadwick et al. (2007).

162x123mm (600 x 600 DPI)

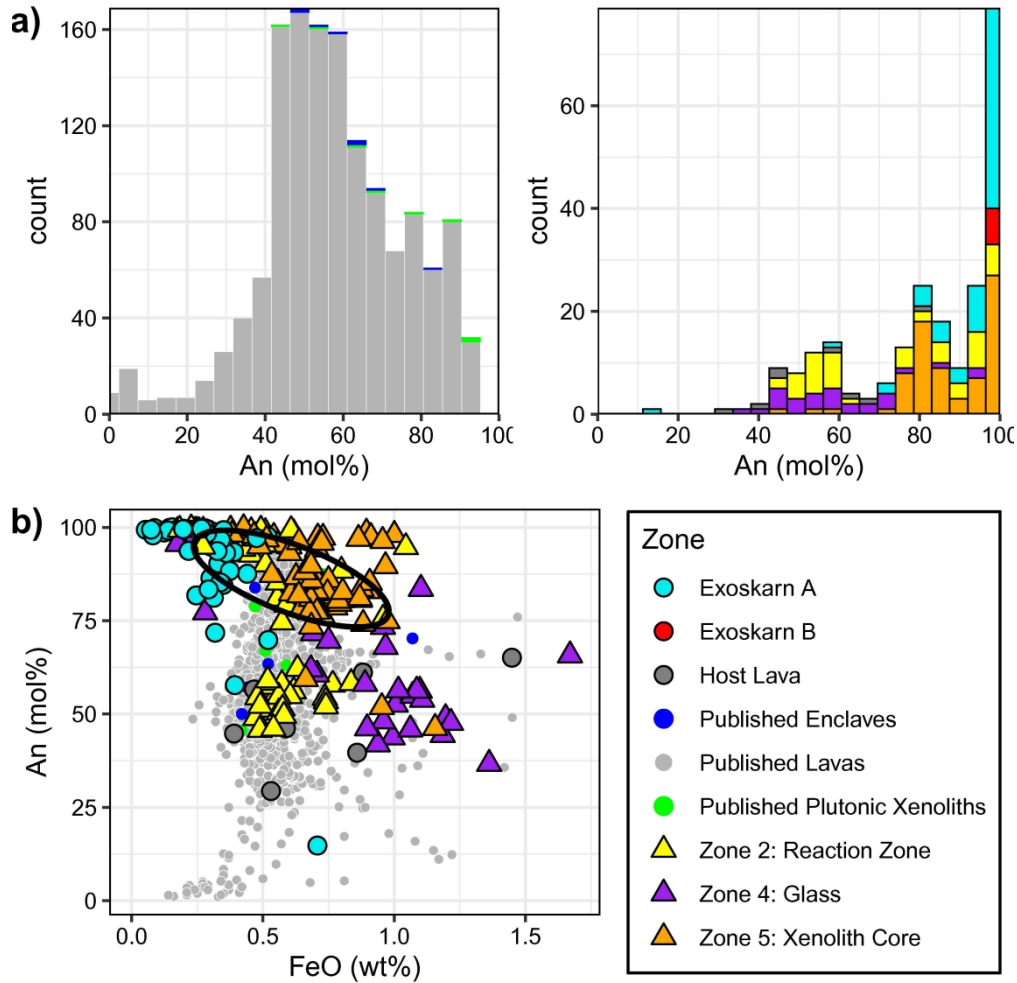


Fig. 6: Merapi xenolith and magmatic feldspar compositions. A) Anorthite content histograms showing (left) published data from Merapi lavas (grey), enclaves (dark blue) and plutonic xenoliths (green) for comparison with xenolith and host lava feldspar data (right, key below). B) An vs FeO plot showing the different xenolith plagioclase compositions compared to Merapi lava plagioclase. Ellipse of xenolith and xenocryst plagioclase compositions from Chadwick et al. (2007). Notably, plagioclase from zones R1 and R2 overlaps with the lava compositions, although they are formed from magma-carbonate interaction. Published lava feldspar data from Gertisser (2001), Preece (2014) and Erdmann et al. (2016). Enclave and plutonic xenolith data from Chadwick et al. (2013).

139x139mm (600 x 600 DPI)

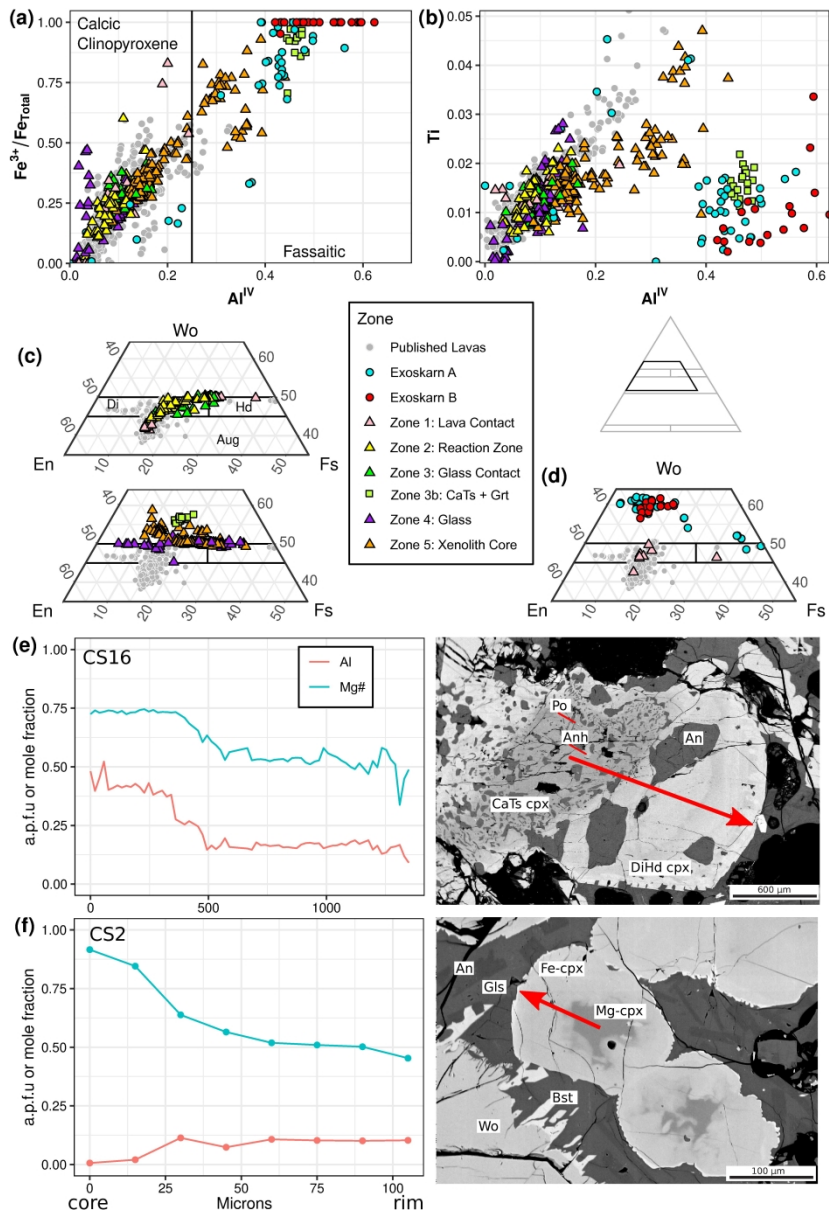


Fig. 7: Clinopyroxene compositions. A) Fe^{3+}/Fe_{total} versus Al^{IV} plot showing a good correlation ($R^2=0.88$). The fassaitic boundary ($Al^{IV} \geq 0.25$) is from Deer et al. (1997). B) Ti versus Al^{IV} plot. Exoskarn clinopyroxene plot distinct from magmatic skarn clinopyroxenes. Zone 3b plots with the exoskarn data, showing a metamorphic character to this zone. C) Ternary Wo-En-Fs components for magmatic skarn clinopyroxene. Two partial ternary diagrams shown for clarity, with ternary location shown on inset figure. Clinopyroxenes in zones 1 to 3 progressively become more Wo-rich, diverging from magmatic compositions. The remaining zones follow the Di-Hd join or plot above due to the large amount of Al. D) Partial ternary Wo-En-Fs components for exoskarn clinopyroxenes. E) Al and Mg# traverse along a magmatic skarn clinopyroxene (sample CS16). Al and Mg-rich cores progressively grade to low Al-high Fe compositions. F) Al and Mg# traverse in magmatic skarn clinopyroxene from sample CS2. These crystals do not have an Al-rich core, and compositions instead follow the Di-Hd join. Published data sources as in Fig. 6 and additionally Deegan et al. (2016b).

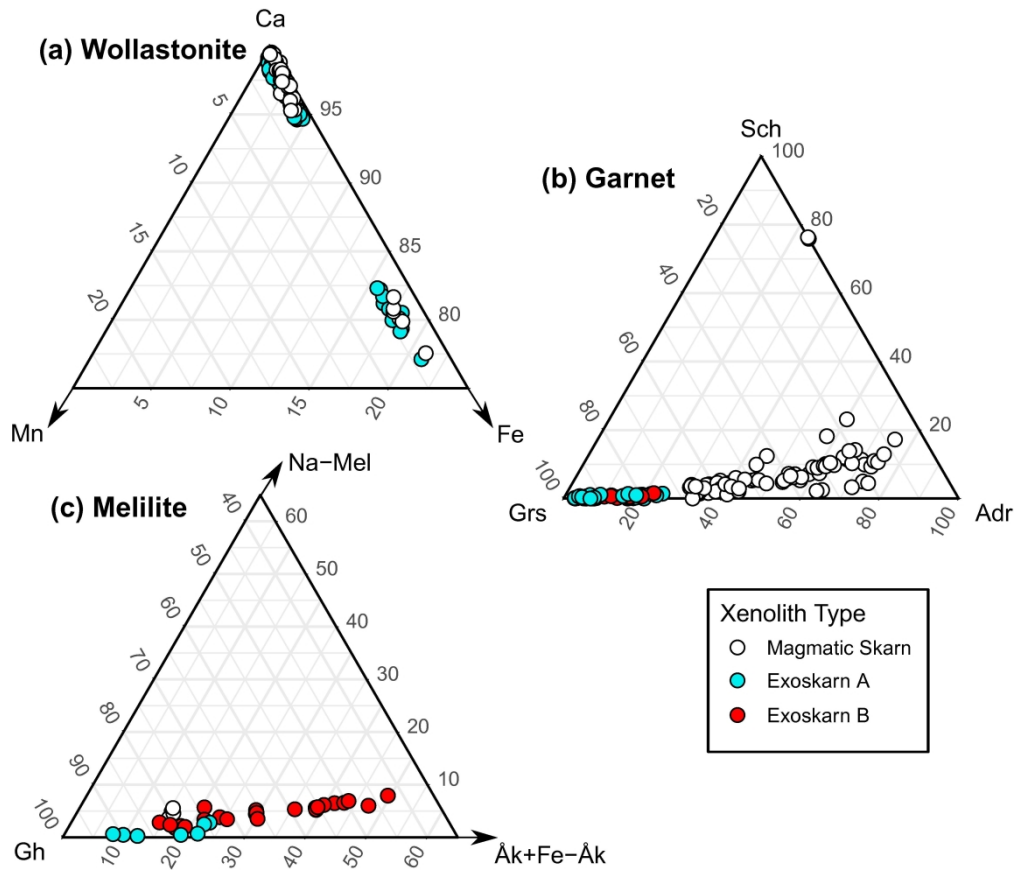


Fig. 8: Additional rock-forming mineral compositions. A) Wollastonite and ferrobustamite. B) Garnet. C) Melilite. Note the different ternary scales for each plot. Arrows indicated truncated scales. Abbreviations as in Table 1.

176x151mm (600 x 600 DPI)

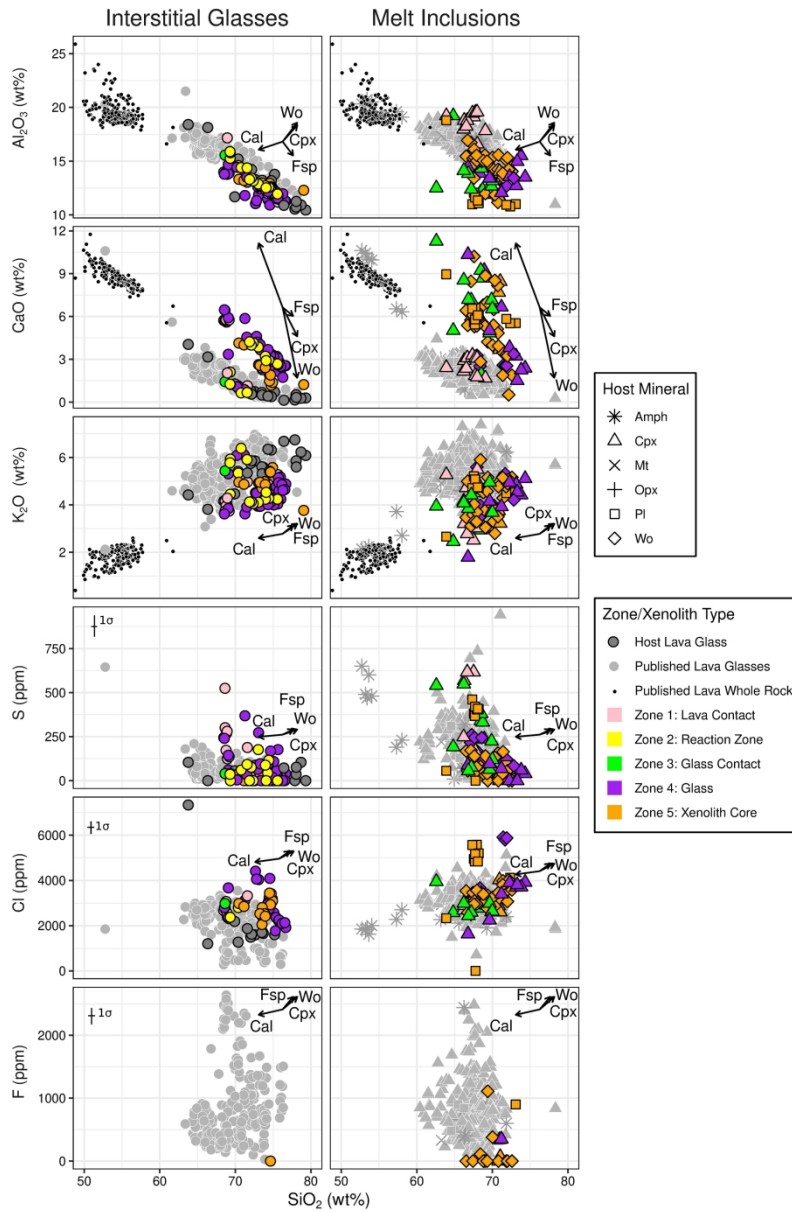


Fig. 9: Interstitial and melt inclusion glass compositions. All values are normalised to 100 wt% volatile free. Published data for whole rock, glass and melt inclusions at Merapi are shown for comparison. Published data from Nadeau et al. (2013b), Borisova et al. (2013), Costa et al. (2013), Innocenti et al. (2013) and the GEOROC database (accessed 03/2019). Arrows show the effect of adding 10% calcite, and subtracting 10% clinopyroxene, wollastonite or plagioclase. Mineral abbreviations as in Table 1.

197x300mm (300 x 300 DPI)

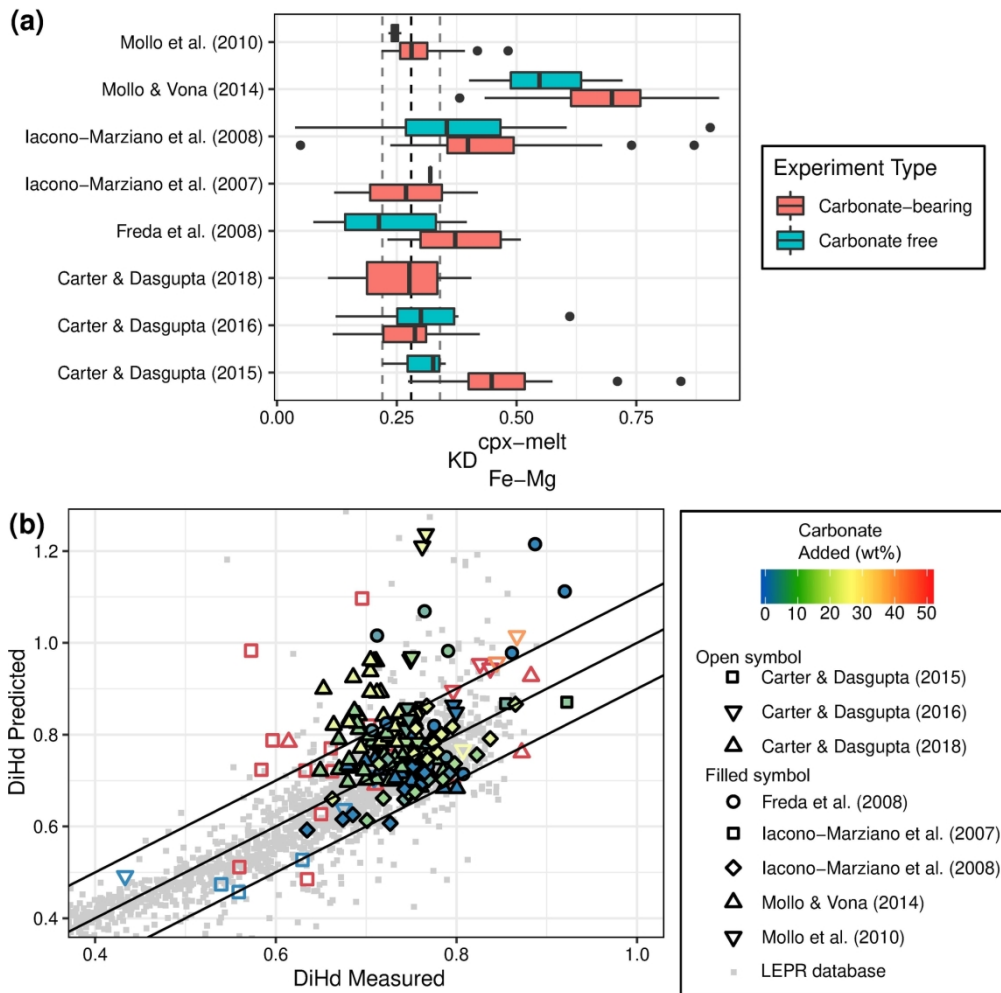


Fig. 10: A) Box plots of $KD_{(Fe-Mg)}^{(cpx-melt)}$ values from carbonate assimilation experiments. Black circles represent outliers calculated as $1.5 \times$ interquartile range from the third quartile. Experiments with carbonate added have a general increase in $KD_{(Fe-Mg)}^{(cpx-melt)}$ values. Experiments by Carter and Dasgupta (2016) and Carter and Dasgupta (2018) use more evolved andesite and dacite compositions, compared to the remaining basaltic experiments, which were less affected by carbonate interaction. The extremely high values from Mollo and Vona (2014) are likely the result of very high experimental fO_2 conditions (up to air), which would strongly affect Fe^{2+}/Fe^{3+} partitioning between clinopyroxene and melt. B) Comparison between measured clinopyroxene Diopside-Hedenbergite ($DiHd$) components and predicted ones, using the iterative approach of Neave and Putirka (2017). Light grey data are calculated from clinopyroxenes in the Library of Experimental Phase Relations (LEPR, Hirschmann et al., 2008) database.

176x174mm (300 x 300 DPI)

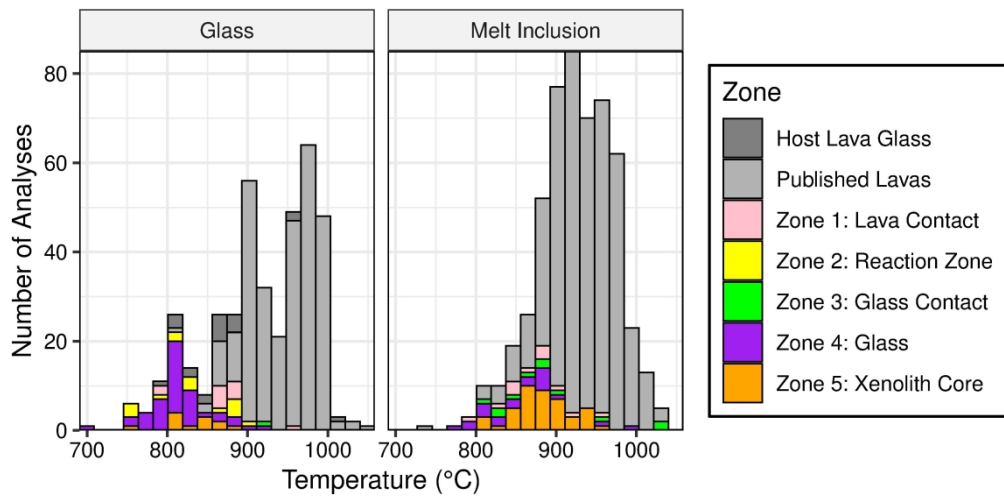


Fig. 11: Stacked histogram results of thermometry estimates for the magmatic skarn xenoliths and host lava glasses using equation 34 of Putirka (2008). Xenolith glasses produce temperatures of $829 \pm 45^\circ\text{C}$ ($n=89$). Melt inclusions have a slightly higher temperature of $876 \pm 49^\circ\text{C}$ ($n=89$). These temperatures are slightly below the thermometry estimates for published lava glass analyses, at $937 \pm 43^\circ\text{C}$. Published glass data are from Preece et al. (2014) and Erdmann et al. (2016).

149x72mm (600 x 600 DPI)

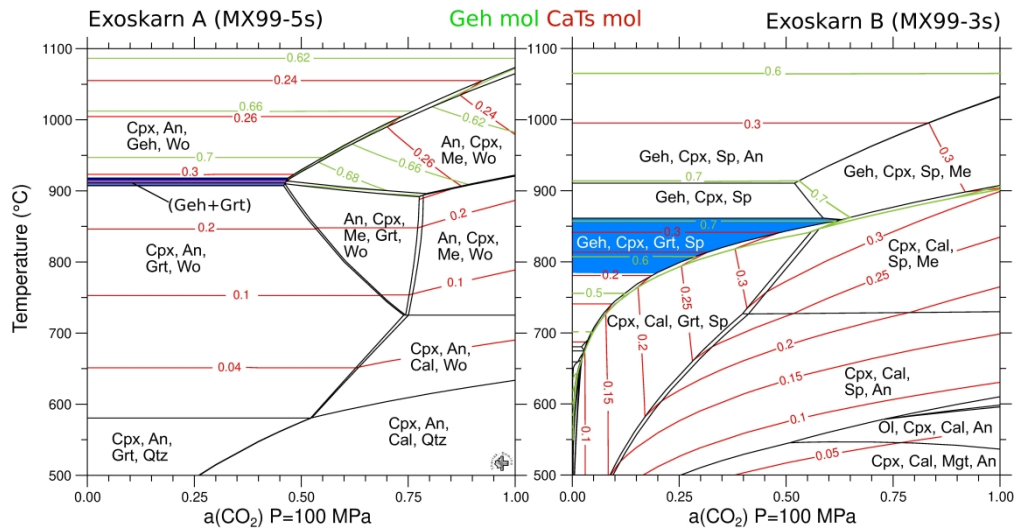


Fig. 12: Theriak-Domino (de Capitani and Petrakakis, 2010) T-XCO₂ modelling of exoskarn xenoliths. Isobaric sections at 100 MPa. Green contours show the gehlenite mole fraction. Red contours show the CaTs mole fractions. The exoskarn A xenolith (MX99-5s) formed in a narrow temperature range between ~900 and 910°C, and XCO₂ < 0.5. The exoskarn B xenolith (MX99-3s) mineral assemblage records temperatures between 680 and 860°C at a XCO₂ <~ 0.5. Abbreviations as in Table 1. Additional abbreviations: Grt - garnet (andradite-grossular), Me - meionite, Ol - olivine

263x136mm (600 x 600 DPI)

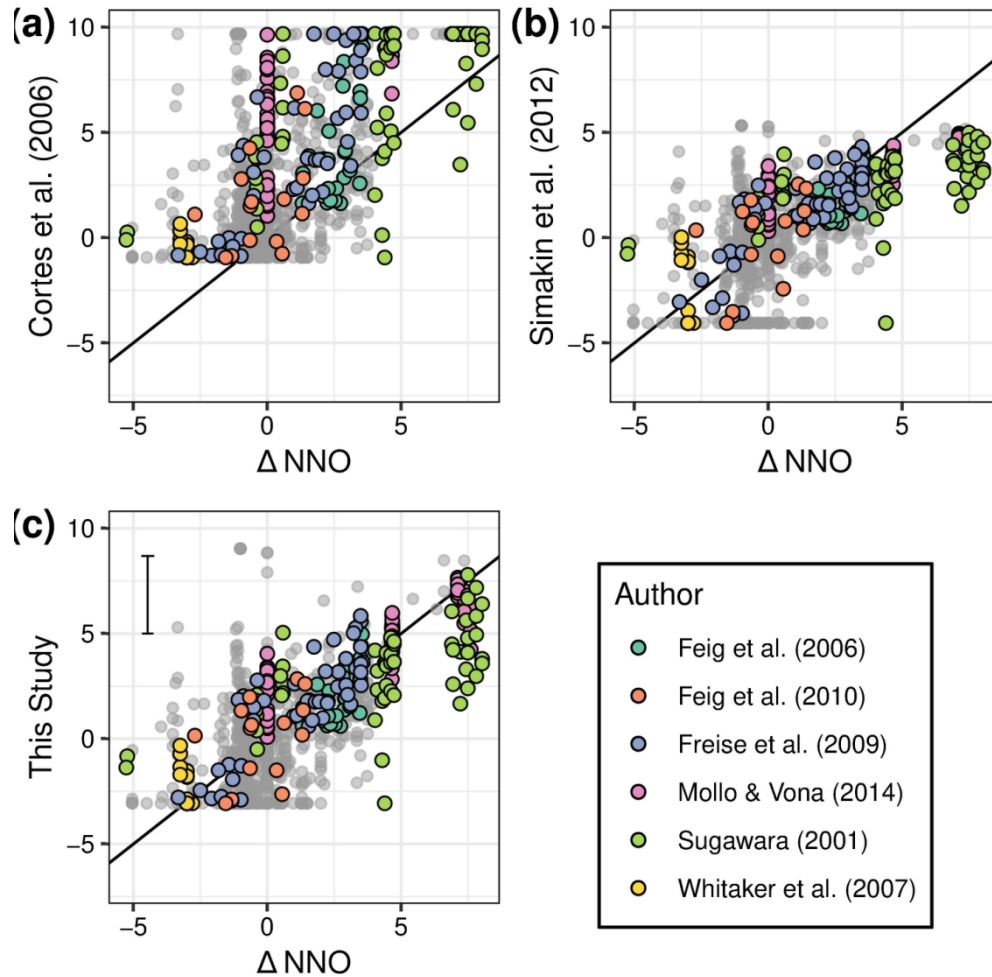


Fig. 13: Clinopyroxene-only single crystal oxybarometer model testing. Experiments used for the calibration of the new oxybarometer are highlighted (Feig et al., 2006, 2010; Berndt et al., 2005; Whitaker et al., 2007; Mollo and Vona, 2014). Sugawara (2001)'s experiments which cover 13 log units, and the results of applying the oxybarometers to the filtered Library of Experimental Phase Relations (LEPR Hirschmann et al., 2008) are also shown. A) Results of the Cortés et al. (2006) oxybarometer applied to the experimental clinopyroxenes. B) Results of the Simakina et al. (2012) oxybarometer applied to the experimental clinopyroxenes. C) Results of the model calibrated in this study applied to the experimental clinopyroxenes. The model error is shown in the top left.

127x127mm (300 x 300 DPI)

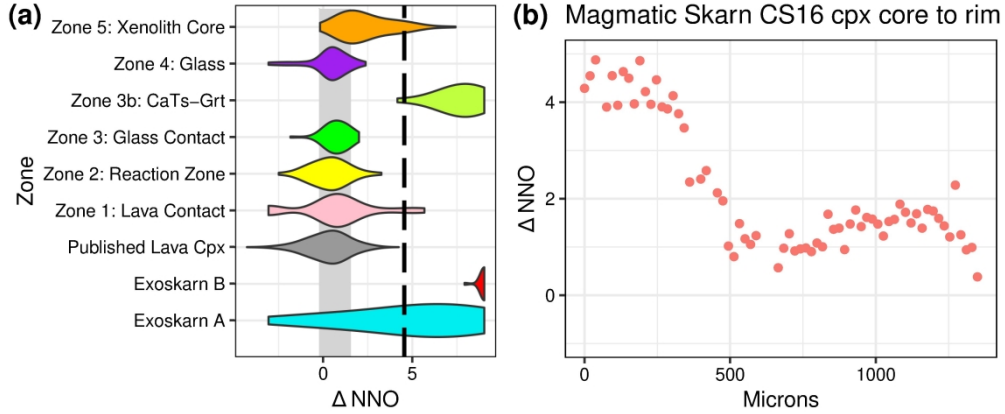


Fig. 14: fO_2 estimates from clinopyroxenes across all zones and traverses. A) Violin density plots of oxygen fugacity estimates for xenolith clinopyroxenes. The model error has been applied as the smoothing bandwidth. The light grey field shows published estimates of Merapi magma fO_2 from other independent methods (ΔNNO -0.2 to 1.6. Gertisser, 2001; Erdmann et al., 2014). Application of our model to the literature clinopyroxene dataset detailed in Fig. 7 is shown for comparison to past literature estimates. The solid dashed line is the magnetite-hematite oxygen fugacity buffer. The results show xenolith rims formed in fO_2 similar to magmatic conditions, whilst the cores and exoskarn xenoliths formed at much higher fO_2 , up to that of air. B) Core to rim calculated fO_2 traverse of the same clinopyroxene from sample CS16 as shown in Fig. 7E, showing high fO_2 during initial clinopyroxene formation

177x76mm (600 x 600 DPI)

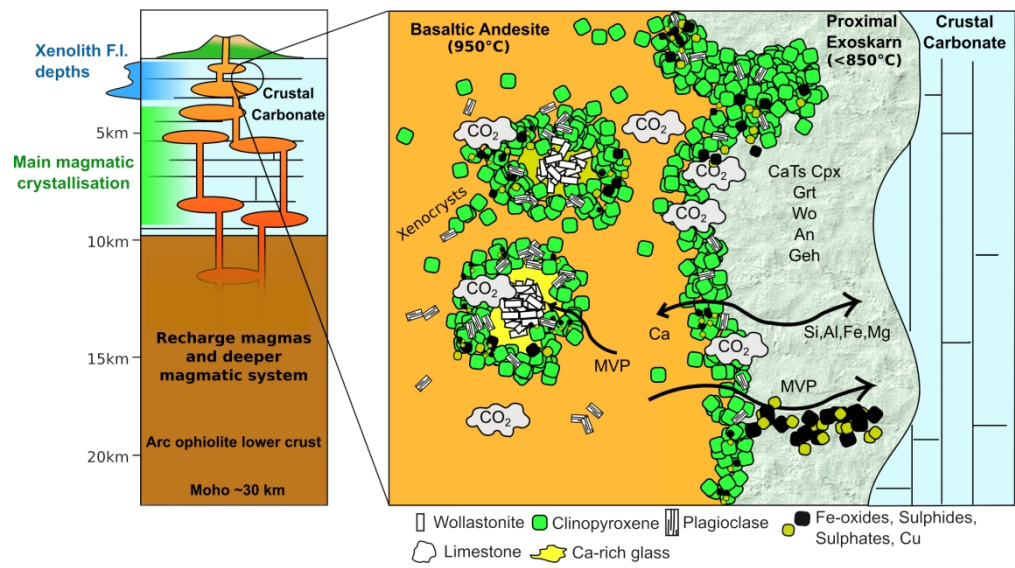


Fig. 15: Summary of the processes occurring during magma carbonate interaction at Merapi. Carbonate is rapidly digested forming a Ca-rich contaminated melt, from which wollastonite and other phases precipitate, forming the magmatic skarn xenoliths. Proximal to the magmatic melt, clinopyroxene and plagioclase form from Ca transfer to the melt from the carbonate. The abundance of melt in the xenoliths allows disaggregation and disperses xenolith crystals into the magma (e.g. Deegan et al., 2010). The magmatic volatile phase (MVP c.f. Nadeau et al., 2010; Preece et al., 2014) infiltrates the xenoliths forming rare halogen and sulphur-bearing minerals. At the wall-rock contact, abundant clinopyroxene forms, partially insulating the carbonate and skarn. Magma-derived elements are transferred to the wall-rock, influenced by the increasing oxygen fugacity caused by CO₂ flushing, forming the exoskarn mineralogy. Regions of main magma crystallisation from Chadwick et al. (2013), Preece et al. (2014) and Erdmann et al. (2016). Moho from Wölbern and Rümpler (2016). Description of the lower crust from van Bemmelen (1949).

1 *Table 1: Mineral phases identified within the Merapi calc-silicate xenoliths in this study, and*
 2 *abbreviations used throughout the text. The minerals are grouped alphabetically within three general*
 3 *groupings.*

Mineral	Abbreviation	Formula	Mag	Exo A	Exo B
<i>Rock-forming and their endmembers</i>					
Clinopyroxene	Cpx	Ca(Fe,Mg)Si ₂ O ₆	M		
–Calcium Tschermak’s Pyroxene	CaTs	CaAlAlSiO ₆	m	M	M
–Esseneite (Clinopyroxene)	Ess	CaFe ³⁺ AlSiO ₆	m	M	M
Garnet	Grt	Ca ₃ (Fe ³⁺ ,Al,Ti) ₂ Si ₃ O ₁₂	m	M	M
–Andradite	Adr	Ca ₃ Fe ³⁺ ₂ Si ₃ O ₁₂	m	M	m
–Grossular	Grs	Ca ₃ Al ₂ Si ₃ O ₁₂	m	M	M
–Schorlomite	Sch	Ca ₃ Ti ₂ Si ₃ O ₁₂	m		
Melilite					
–Åkermanite	Åk	Ca ₂ MgSi ₂ O ₇	m	m	M
–Fe-Åkermanite	Fe-Åk	Ca ₂ FeSi ₂ O ₇	m	m	M
–Gehlenite	Gh	Ca ₂ Al ₂ SiO ₇	m	m	M
–Na-Melilite	Na-Mel	CaNaAl ₂ SiO ₇			
Plagioclase	Pl	(Ca,Na)(Al,Si) ₄ O ₈	M	M	m
–Anorthite	An	CaAl ₂ Si ₂ O ₈	M	M	m
Wollastonite	Wo	CaSiO ₃	M	M	m
–Ferrobustamite	Bst	Ca(Fe ²⁺ ,Ca,Mn ²⁺)Si ₂ O ₆	m	m	
<i>Sulphur and Halogen-bearing</i>					
Anhydrite	Anh	CaSO ₄	m	m	
Apatite	Ap	Ca ₅ (PO ₄) ₃ (OH,F,Cl)	m		
Baryte	Ba	BaSO ₄	m		
Cotunnite*	Cot	PbCl ₂	m		
Cubanite	Cu	CuFe ₂ S ₃	m		
Cuspidine	Cusp	Ca ₄ Si ₂ O ₇ (F,OH) ₂	m	m	
Ellestadite	El	Ca ₅ (SiO ₄ ,PO ₄ ,SO ₄) ₃ (F,OH,Cl)		m	m
Fluorite	Fl	CaF ₂	m		
Larnite	Lrn	Ca ₂ SiO ₄		m	
Pyrrhotite	Po	Fe _{1-x} S (x=0-0.2)	m	m	
Spurrite	Spu	Ca ₅ Si ₂ O ₈ CO ₃		m	
Wadalite†	Wad	Ca ₁₂ Al ₁₀ Si ₄ O ₃₂ Cl ₆	m		
<i>Oxides, Other Silicates, and Accessory Minerals</i>					
Calcite	Cal	CaCO ₃	m	M	
Ca-Zr-Ti oxide*	CaZrTi	Ca-Zr-Ti	m		
Cebollite†	Ce	Ca ₅ Al ₂ (SiO ₄) ₃ (OH) ₄		m	
Chromite*	Chr	FeCr ₂ O ₄	m		
Hematite	Hm	Fe ₂ O ₃		m	
Ilmenite	Ilm	FeTiO ₃	m		
Magnetite	Mgt	Fe ²⁺ Fe ³⁺ ₂ O ₄	M	m	
Quartz	Qtz	SiO ₂	M	m	
Monazite*	Mo	(Ce,La)PO ₄		m	
Perovskite	Psk	CaTiO ₃	m		
Titanite	Ttn	CaTiSiO ₄	m	m	
Spinel	Sp	(Fe,Mg)Al ₂ O ₄			M
Xenotime*	Xe	YPO ₄		m	

* Identified with SEM only † Uncertain identification

Mag Magmatic skarn xenoliths, Exo A: Exoskarn type A xenoliths, Exo B: Exoskarn type B xenoliths

For Peer Review

1 *Table 2: Average plagioclase compositions for the zones in the magmatic skarn xenoliths, and in the*
 2 *exoskarn xenoliths. All analyses normalised to 8 oxygens. Lava analyses are where the xenolith section*
 3 *had a small rind of lava still attached. Analyses are reported as the mean with one standard deviation in*
 4 *brackets. Plagioclase components: An = anorthite, Ab = albite, Or = orthoclase.*

Type Zone n	Magmatic Skarn				Exoskarn			
	Host Lava	R2	R4	Core	Exoskarn A	Exoskarn B		
	8	49	27	76	63	7		
SiO ₂	53.61 (4.03)	48.91 (4.42)	52.91 (4.28)	45.21 (2.80)	44.43 (3.50)	42.51 (0.51)		
Al ₂ O ₃	28.10 (2.94)	31.73 (3.31)	28.68 (3.00)	33.98 (2.03)	34.90 (2.48)	36.55 (0.37)		
FeO	0.72 (0.34)	0.58 (0.16)	0.94 (0.33)	0.65 (0.22)	0.33 (0.33)	0.24 (0.02)		
MgO	0.06 (0.07)	0.02 (0.02)	0.02 (0.03)	0.01 (0.02)	0.02 (0.02)			
CaO	11.12 (3.28)	15.05 (3.72)	12.25 (2.99)	17.82 (2.18)	19.09 (2.63)	20.17 (0.26)		
Na ₂ O	5.06 (1.70)	3.01 (2.12)	4.25 (1.65)	1.34 (1.23)	0.78 (1.45)	0.08 (0.03)		
K ₂ O	0.68 (0.52)	0.23 (0.20)	0.53 (0.44)	0.10 (0.14)	0.07 (0.17)	0.02 (0.01)		
Total	99.47 (0.64)	99.56 (0.87)	99.76 (1.20)	99.12 (1.09)	99.75 (1.01)	99.56 (1.06)		
Cations based on 8 oxygens								
Si	2.449 (0.166)	2.252 (0.188)	2.416 (0.168)	2.108 (0.113)	2.063 (0.138)	1.983 (0.009)		
Al	1.515 (0.168)	1.724 (0.191)	1.546 (0.178)	1.869 (0.118)	1.912 (0.146)	2.009 (0.009)		
Fe	0.028 (0.013)	0.022 (0.006)	0.036 (0.013)	0.025 (0.009)	0.013 (0.013)	0.009 (0.001)		
Mg	0.004 (0.005)	0.001 (0.001)	0.001 (0.002)	0.000 (0.001)	0.001 (0.001)	0.000 (0.000)		
Ca	0.546 (0.165)	0.744 (0.189)	0.601 (0.154)	0.891 (0.114)	0.951 (0.135)	1.008 (0.006)		
Na	0.448 (0.147)	0.267 (0.188)	0.375 (0.143)	0.120 (0.109)	0.069 (0.126)	0.007 (0.003)		
K	0.039 (0.030)	0.013 (0.012)	0.030 (0.025)	0.006 (0.008)	0.004 (0.010)	0.001 (0.000)		
ΣCations	5.032 (0.009)	5.025 (0.011)	5.011 (0.020)	5.020 (0.007)	5.017 (0.018)	5.017 (0.006)		
An	52.9 (16.2)	72.8 (19.1)	59.8 (15.5)	87.6 (11.1)	92.9 (13.1)	99.2 (0.3)		
Ab	43.3 (14.0)	25.9 (18.1)	37.2 (14.1)	11.8 (10.7)	6.7 (12.2)	0.7 (0.3)		
Or	3.8 (2.9)	1.3 (1.1)	3.1 (2.7)	0.6 (0.8)	0.4 (0.9)	0.1 (0.0)		

1 Table 3: Average clinopyroxene (cpx), wollastonite (wo), and ferrobustamite (bst) compositions for each zone in the magmatic skarn xenoliths, exoskarns,
 2 and across all samples for wollastonite and ferrobustamite as there is very little compositional variability for the pyroxenoids. Fe³⁺ calculated using
 3 Droop (1987). Analyses are reported as the mean with one standard deviation in brackets. Clinopyroxene components: Wo = wollastonite, En = enstatite,
 4 Fs = ferrosilite. All Fe assumed as Fe²⁺ for ternary component calculation.

Type	Magmatic Skarn												Exoskarn				All	All
Zone	Host Lava		R1	R2	R3	R3b	R4	Core		Exoskarn A		Exoskarn B						
Mineral	Cpx	Cpx	Cpx	Cpx	Cpx	Cpx	Cpx	Cpx	Cpx	Cpx	Cpx	Cpx	Cpx	Wo	Bst			
n	7	19	43	44	18	71	112	40	18	94	16							
SiO ₂	51.13 (0.72)	50.11 (1.54)	50.37 (0.94)	49.89 (1.41)	40.89 (0.46)	49.83 (1.70)	46.26 (1.94)	43.24 (2.67)	40.52 (1.87)	50.70 (0.69)	49.81 (0.52)							
TiO ₂	0.5 (0.11)	0.49 (0.10)	0.45 (0.16)	0.42 (0.10)	0.57 (0.10)	0.37 (0.23)	0.67 (0.27)	0.53 (0.36)	0.36 (0.27)	0.04 (0.05)	0.06 (0.04)							
Al ₂ O ₃	2.63 (0.43)	2.71 (1.56)	2.09 (0.64)	2.37 (0.59)	14.64 (0.40)	2.08 (0.96)	5.76 (2.89)	13.93 (5.95)	18.19 (1.97)	0.07 (0.08)	0.02 (0.02)							
Cr ₂ O ₃	0 (0.01)	0.02 (0.02)	0.02 (0.02)	0.02 (0.02)	0.01 (0.01)	0.01 (0.02)	0.02 (0.02)	0.01 (0.01)	0.02 (0.02)	0.01 (0.01)	0.01 (0.01)							
FeO	8.85 (0.12)	12.38 (5.99)	10.62 (1.85)	12.58 (2.84)	8.58 (0.47)	13.46 (4.14)	11.26 (3.03)	7.96 (6.72)	5.65 (1.15)	1.31 (0.80)	10.81 (0.97)							
MnO	0.56 (0.11)	0.57 (0.19)	0.55 (0.11)	0.48 (0.10)	0.32 (0.02)	0.5 (0.16)	0.21 (0.10)	0.24 (0.32)	0.08 (0.03)	0.37 (0.16)	1.13 (0.19)							
MgO	14.43 (0.43)	11.38 (4.68)	11.74 (1.77)	10.82 (2.83)	9.07 (0.52)	9.45 (2.73)	9.66 (1.41)	8.59 (2.25)	9.57 (1.12)	0.22 (0.08)	0.70 (0.22)							
CaO	21.2 (0.66)	22.06 (1.27)	22.62 (0.68)	22.72 (1.12)	25.18 (0.17)	23.9 (0.77)	23.76 (0.70)	25.04 (0.84)	25.88 (0.47)	47.09 (0.92)	38.08 (1.48)							
Na ₂ O	0.43 (0.04)	0.34 (0.12)	0.41 (0.08)	0.38 (0.07)	0.02 (0.02)	0.29 (0.14)	0.33 (0.15)	0.07 (0.07)	0.04 (0.02)	0.02 (0.02)	0.04 (0.03)							
Total	99.75 (0.50)	100.08 (0.81)	98.87 (0.71)	99.67 (0.82)	99.28 (0.64)	99.93 (0.60)	97.92 (0.70)	99.62 (1.24)	100.31 (0.81)	99.93 (0.88)	100.8 (1.40)							
Cations based on 6 oxygens, 4 cations																		
Si	1.901 (0.021)	1.895 (0.059)	1.918 (0.028)	1.898 (0.024)	1.535 (0.013)	1.906 (0.040)	1.786 (0.086)	1.624 (0.136)	1.485 (0.065)	1.967 (0.025)	1.956 (0.038)							
Ti	0.014 (0.003)	0.014 (0.003)	0.013 (0.005)	0.012 (0.003)	0.016 (0.003)	0.011 (0.006)	0.019 (0.008)	0.015 (0.011)	0.010 (0.008)	0.001 (0.001)	0.002 (0.001)							
Al ^{IV}	0.099 (0.021)	0.105 (0.059)	0.082 (0.028)	0.102 (0.024)	0.465 (0.013)	0.094 (0.040)	0.214 (0.086)	0.376 (0.136)	0.515 (0.065)	0.033 (0.025)	0.044 (0.038)							
Al ^{VI}	0.018 (0.013)	0.018 (0.021)	0.013 (0.009)	0.006 (0.008)	0.183 (0.013)	0.007 (0.018)	0.047 (0.047)	0.238 (0.117)	0.271 (0.036)	0.000 (0.000)	0.000 (0.000)							
Cr	0.000 (0.000)	0.000 (0.001)	0.001 (0.001)	0.000 (0.001)	0.000 (0.000)	0.000 (0.001)	0.000 (0.001)	0.000 (0.000)	0.000 (0.001)	0.000 (0.000)	0.000 (0.000)							
Fe ²⁺	0.190 (0.032)	0.309 (0.241)	0.264 (0.071)	0.300 (0.087)	0.019 (0.022)	0.339 (0.122)	0.212 (0.106)	0.138 (0.230)	0.000 (0.002)	0.010 (0.018)	0.269 (0.076)							
Fe ³⁺	0.086 (0.033)	0.088 (0.060)	0.075 (0.031)	0.102 (0.024)	0.251 (0.014)	0.094 (0.041)	0.153 (0.038)	0.117 (0.051)	0.173 (0.037)	0.033 (0.023)	0.086 (0.075)							
Mn	0.017 (0.004)	0.018 (0.007)	0.018 (0.004)	0.015 (0.003)	0.010 (0.001)	0.016 (0.005)	0.007 (0.003)	0.008 (0.011)	0.002 (0.001)	0.012 (0.005)	0.038 (0.006)							
Mg	0.800 (0.021)	0.635 (0.255)	0.665 (0.092)	0.611 (0.148)	0.507 (0.027)	0.536 (0.143)	0.555 (0.072)	0.478 (0.118)	0.523 (0.058)	0.013 (0.005)	0.041 (0.013)							
Ca	0.844 (0.028)	0.895 (0.064)	0.923 (0.037)	0.927 (0.060)	1.013 (0.006)	0.980 (0.022)	0.982 (0.014)	1.006 (0.016)	1.017 (0.008)	1.957 (0.033)	1.601 (0.043)							
Na	0.031 (0.003)	0.024 (0.009)	0.030 (0.006)	0.028 (0.005)	0.002 (0.001)	0.022 (0.010)	0.025 (0.012)	0.005 (0.005)	0.003 (0.001)	0.002 (0.001)	0.003 (0.002)							
#Mg	74.4 (0.6)	60.6 (22.7)	66.1 (7.3)	59.8 (11.3)	65.3 (2.5)	55.3 (14.2)	60.7 (9.9)	68.3 (21.5)	75 (5.8)	27.5 (14.1)	10.4 (3.0)							
Wo	43.6 (1.2)	46 (3.3)	47.5 (1.9)	47.4 (3.0)	56.3 (0.6)	49.8 (0.8)	51.5 (1.7)	57.9 (3.9)	59.3 (1.3)	96.7 (1.5)	78.7 (1.5)							
En	41.3 (1.1)	32.7 (13.1)	34.2 (4.7)	31.3 (7.6)	28.2 (1.4)	27.3 (7.1)	29.1 (4.1)	27.8 (7.8)	30.4 (2.9)	0.6 (0.2)	2.0 (0.6)							
Fs	15.1 (0.3)	21.3 (10.8)	18.3 (3.2)	21.3 (4.8)	15.5 (0.9)	22.9 (7.1)	19.9 (5.3)	14.3 (11.4)	10.3 (2.3)	2.7 (1.4)	19.3 (1.5)							

For Peer Review

1 *Table 4: Average garnet compositions for the zones in the magmatic skarn xenoliths, and in the exoskarn*
2 *xenoliths. Abbreviations as in Table 1. Additional garnet abbreviations: Prp - pyrope, Alm - almandine,*
3 *Sp - spessartite, Uv - uvarovite. See Methods section for end-member calculation details. Fe³⁺ calculated*
4 *using Arai (2010). Analyses are reported as the mean with one standard deviation in brackets.*

Xenolith Type Zone n	Magmatic Skarn				Exoskarn			
	R3b		Core		Exoskarn A		Exoskarn B	
	10		65		47		10	
SiO ₂	38.27	(0.23)	35.01	(2.93)	39.27	(0.55)	38.94	(0.30)
TiO ₂	0.76	(0.24)	3.45	(3.73)	0.23	(0.20)	0.29	(0.19)
Al ₂ O ₃	14.24	(0.50)	9.64	(3.16)	20.37	(1.68)	18.88	(1.02)
Cr ₂ O ₃			0.02	(0.03)	0.01	(0.02)	0.01	(0.02)
FeO	10.14	(0.49)	15.25	(3.60)	3.26	(1.88)	4.66	(1.11)
MnO	0.47	(0.05)	0.26	(0.09)	0.72	(0.68)	0.15	(0.03)
MgO	0.57	(0.04)	0.49	(0.19)	0.42	(0.17)	0.74	(0.10)
CaO	35.13	(0.26)	33.75	(0.78)	35.86	(0.78)	36.68	(0.54)
Total	99.59	(0.29)	97.86	(0.98)	100.23	(0.92)	100.35	(0.65)
Cations based on 12 oxygens, 8 cations								
Si	2.972	(0.013)	2.831	(0.196)	2.966	(0.026)	2.944	(0.032)
Ti	0.044	(0.014)	0.214	(0.243)	0.013	(0.012)	0.016	(0.011)
Al	1.304	(0.043)	0.913	(0.281)	1.813	(0.139)	1.681	(0.077)
Cr	0.000	(0.000)	0.001	(0.002)	0.000	(0.001)	0.001	(0.001)
Fe ²⁺	0.007	(0.017)	0.042	(0.042)	0.013	(0.024)	0.000	(0.000)
Fe ³⁺	0.652	(0.038)	0.995	(0.247)	0.194	(0.120)	0.295	(0.073)
Mn	0.031	(0.003)	0.018	(0.007)	0.046	(0.043)	0.010	(0.002)
Mg	0.066	(0.004)	0.059	(0.023)	0.047	(0.019)	0.083	(0.011)
Ca	2.923	(0.023)	2.926	(0.039)	2.902	(0.064)	2.970	(0.024)
Grs	64.3	(1.6)	37.5	(17.2)	87.7	(6.6)	83.9	(4.0)
Adr	33.5	(1.9)	52.0	(14.4)	9.6	(6.4)	15.1	(3.7)
Sch	1.4	(0.6)	9.3	(12.7)	0.4	(0.4)	0.7	(0.4)
Alm	0.0	(0.2)	0.2	(0.5)	0.4	(0.7)	0.0	(0.0)
Prp	0.7	(0.8)	0.8	(0.9)	0.7	(0.8)	0.3	(0.6)
Sp	0.1	(0.4)	0.1	(0.3)	1.2	(1.7)	0.0	(0.0)
Uv	0.0	(0.0)	0.0	(0.1)	0.0	(0.0)	0.0	(0.0)

1 *Table 5: Average melilite compositions for the magmatic skarn xenolith core, and in the exoskarn*
2 *xenoliths. All analyses are normalised to 7 oxygens. Abbreviations as in Table 1. See Methods section for*
3 *details about the calculation of mole fractions of end-member compositions. Analyses are reported as the*
4 *mean with one standard deviation in brackets.*

Xenolith Type Zone n	Magmatic Skarn		Exoskarn			
	Core		Exoskarn A	Exoskarn B		
	4		7	26		
SiO ₂	24.72	(0.43)	25.29	(1.80)	29.06	(3.01)
TiO ₂	0.01	(0.02)	0.01	(0.02)	0.01	(0.02)
Al ₂ O ₃	29.87	(0.47)	28.92	(2.03)	25.09	(4.37)
Cr ₂ O ₃	0.02	(0.01)	0.02	(0.01)	0.01	(0.01)
FeO	2.66	(0.07)	1.87	(0.97)	0.93	(0.18)
MnO	0.10	(0.02)	0.35	(0.24)	0.05	(0.03)
MgO	0.69	(0.03)	1.22	(1.05)	3.74	(1.43)
CaO	39.56	(0.16)	40.60	(0.43)	40.56	(0.95)
Na ₂ O	0.54	(0.10)	0.13	(0.12)	0.52	(0.21)
Total	98.17	(0.88)	98.55	(0.93)	99.99	(1.09)
Cations based on 7 oxygens						
Si	1.165	(0.013)	1.186	(0.074)	1.331	(0.136)
Ti	0.000	(0.001)	0.000	(0.001)	0.000	(0.001)
Al	1.659	(0.012)	1.600	(0.120)	1.354	(0.237)
Cr	0.001	(0.000)	0.001	(0.001)	0.000	(0.000)
Fe	0.105	(0.002)	0.074	(0.038)	0.036	(0.007)
Mn	0.004	(0.001)	0.014	(0.010)	0.002	(0.001)
Mg	0.048	(0.002)	0.085	(0.072)	0.255	(0.097)
Ca	1.998	(0.021)	2.042	(0.032)	1.990	(0.036)
Na	0.049	(0.009)	0.012	(0.011)	0.046	(0.018)
∑Cations	5.029	(0.013)	5.018	(0.012)	5.015	(0.017)
Gh	79.7	0.7	82.3	7.1	65.2	12.5
Ak	4.9	0.2	8.9	7.6	26.6	10.5
Fe-Ak	10.7	0.2	7.7	3.9	3.7	0.7
Na-Mel	4.7	0.8	1.1	1.1	4.5	1.8

1 *Table 6: Cu-bearing mineral compositions. Cubanite has only been found in magmatic skarn xenoliths,*
 2 *whilst pyrrhotite is found across all xenolith types, with little chemical variation between xenolith types.*
 3 *Analyses are reported as the mean with one standard deviation in brackets*

	Po		Cub	
<i>n</i>	10		5	
Fe	58.44	(0.49)	38.7	(1.12)
S	39.83	(0.24)	35.08	(0.67)
Co	0.20	(0.02)	0.12	(0.03)
Ni	0.48	(0.11)	0.06	(0.05)
Cu	0.30	(0.17)	24.26	(1.51)
Zn	0.03	(0.02)	0.09	(0.05)
Total	99.28	(0.60)	98.3	(0.57)
Sulphurs	1		3	
Fe	0.842	(0.007)	1.899	(0.036)
Co	0.003	(0.003)	0.005	(0.001)
Ni	0.007	(0.002)	0.003	(0.002)
Cu	0.004	(0.002)	1.048	(0.082)
Zn	0.005	(0.003)	0.004	(0.002)
Total	0.856	(0.007)	2.959	(0.072)
Fe/S	0.84	(0.01)		

1 *Table 7: Selected analyses of halogen and sulphur-bearing minerals. Wad-1, Wad-2 are the wadalite-like*
 2 *phase, found in sample MX1. Unk1 and Unk2 are unknown volatile-bearing minerals in samples CS11*
 3 *and MXCS-b respectively. SEM-EDS analysis shows the presence of Cl and F in these latter two*
 4 *minerals. Normalisation cations for the unknown volatile-bearing minerals are chosen to produce*
 5 *plausible formula units, and are not to represent any currently known minerals. Analyses are reported as*
 6 *the mean with one standard deviation in brackets*

Sample Mineral Type n	Multiple Cusp Magmatic Skarn 5		Multiple El Magmatic Skarn 4		MX1 Wad-1 Magmatic Skarn 11		MX1 Wad-2 Magmatic Skarn 2		CS11 Unk1 Exoskarn A 2		M-XCS-1 Unk2 Exoskarn B 2	
SiO ₂	32.70	(0.42)	8.37	(1.27)	17.63	(0.41)	24.98	(1.99)	26.70	(0.05)	23.33	(0.44)
TiO ₂	0.19	(0.15)	0.02	(0.03)	0.38	(0.17)	0.56	(0.29)	0.00	(0.00)	0.01	(0.02)
Al ₂ O ₃	0.02	(0.01)	0.03	(0.02)	23.85	(1.05)	19.59	(0.98)	14.47	(0.42)	12.98	(0.02)
Cr ₂ O ₃	0.02	(0.02)	0.00	(0.00)	0.01	(0.02)	0.00	(0.01)	0.00	(0.00)	0.00	(0.00)
FeO	0.14	(0.08)	0.08	(0.03)	5.63	(1.21)	6.26	(2.60)	1.52	(0.37)	0.71	(0.15)
MnO	0.08	(0.02)	0.03	(0.01)	0.18	(0.05)	0.24	(0.15)	0.26	(0.10)	0.07	(0.06)
MgO	0.07	(0.07)	0.05	(0.02)	0.60	(0.08)	0.43	(0.09)	0.24	(0.01)	0.01	(0.01)
CaO	60.20	(0.24)	54.16	(1.19)	40.18	(0.43)	39.67	(3.09)	52.48	(0.13)	56.23	(0.26)
Na ₂ O	0.02	(0.02)	0.01	(0.02)	0.17	(0.16)	0.09	(0.04)	0.00	(0.00)	0.01	(0.02)
K ₂ O	0.01	(0.01)	0.00	(0.00)	0.00	(0.01)	0.02	(0.00)	0.00	(0.00)	0.01	(0.01)
P ₂ O ₅	0.00	(0.00)	24.03	(3.25)	0.13	(0.13)	0.13	(0.18)			0.04	(0.02)
SO ₃	0.00	(0.00)	8.12	(1.42)	0.01	(0.01)	0.00	(0.00)			0.02	(0.01)
Cl	0.01	(0.00)	1.04	(0.22)	12.91	(0.17)	8.87	(2.74)			2.12	(0.00)
F	10.26	(0.14)			0.02	(0.02)	0.00				4.90	(0.00)
Total	103.70	(0.40)	95.94	(0.81)	101.69	(0.56)	100.85	(2.08)	95.67	(0.12)	100.61	(0.10)
O=(F ₂ ,Cl ₂)	-4.32	(0.06)	-0.23	(0.05)	-2.92	(0.04)	-2.00	(0.62)	0.00	(0.00)	-2.54	(0.00)
Total.1	99.38	(0.44)	95.71	(0.78)	98.77	(0.53)	98.85	(1.46)	95.67	(0.12)	98.07	(0.10)
Cations based on x cations	6		8		26		26		9		16	
Si	2.002	(0.009)	0.701	(0.106)	4.753	(0.092)	6.168	(0.277)	2.337	(0.006)	4.042	(0.058)
Ti	0.009	(0.007)	0.002	(0.002)	0.078	(0.034)	0.103	(0.051)	0.000	(0.000)	0.001	(0.002)
Al	0.001	(0.001)	0.003	(0.002)	7.578	(0.297)	5.713	(0.484)	1.493	(0.037)	2.649	(0.009)
Cr	0.001	(0.001)	0.000	(0.000)	0.003	(0.003)	0.001	(0.001)	0.000	(0.000)	0.000	(0.000)
Fe	0.007	(0.004)	0.006	(0.002)	1.270	(0.277)	1.285	(0.493)	0.112	(0.028)	0.103	(0.022)
Mn	0.004	(0.001)	0.002	(0.001)	0.042	(0.012)	0.050	(0.030)	0.019	(0.008)	0.011	(0.008)
Mg	0.007	(0.006)	0.007	(0.003)	0.240	(0.032)	0.159	(0.039)	0.031	(0.001)	0.002	(0.002)
Ca	3.949	(0.026)	4.858	(0.102)	11.610	(0.160)	10.524	(1.187)	4.923	(0.008)	10.436	(0.096)
Na	0.002	(0.002)	0.001	(0.003)	0.087	(0.083)	0.045	(0.022)	0.000	(0.000)	0.004	(0.005)
K	0.001	(0.001)	0.000	(0.000)	0.002	(0.003)	0.007	(0.000)	0.000	(0.000)	0.002	(0.002)
P	0.000	(0.000)	1.704	(0.230)	0.031	(0.029)	0.027	(0.038)	0.000	(0.000)	0.006	(0.003)
S	0.000	(0.000)	0.510	(0.089)	0.001	(0.003)	0.000	(0.000)	0.000	(0.000)	0.002	(0.001)
Cl	0.001	(0.000)	0.147	(0.031)	5.903	(0.087)	3.735	(1.277)	0.000	(0.000)	0.622	(0.003)
F	1.986	(0.044)	0.000	(0.000)	0.006	(0.011)	0.000	(0.000)	0.000	(0.000)	2.684	(0.012)

1 *Table 8: Average analyses of oxides and other silicate minerals found in the Merapi xenoliths. Analyses*
 2 *are reported as the mean with one standard deviation in brackets*

Xenolith Type Mineral	Magmatic skarn								Exoskarn A	Exoskarn B	
	Mgt	Ilm	Hem		Psk	Ttn		CaSiAlP	Sp		
n	27	1	4		3	8		1	8		
SiO ₂	0.14 (0.10)	5.92	0.31 (0.15)	1.13 (0.83)	30.91 (1.13)	33.30	0.01 (0.01)				
TiO ₂	9.91 (5.16)	43.22	0.15 (0.20)	54.75 (0.63)	36.28 (2.33)	1.19	0.01 (0.01)				
Al ₂ O ₃	2.66 (1.15)	1.10	0.59 (1.14)	0.43 (0.16)	1.70 (0.51)	26.28	66.59 (0.58)				
Cr ₂ O ₃	0.18 (0.20)	0.19	0.02 (0.02)	0.01 (0.01)	0.03 (0.03)	0.00	0.10 (0.07)				
FeO	78.73 (4.81)	42.16	86.61 (2.79)	0.80 (0.15)	1.31 (0.70)	0.28	8.48 (1.41)				
MnO	0.89 (0.30)	0.87	0.13 (0.14)	0.04 (0.03)	0.08 (0.07)	0.00	0.38 (0.08)				
MgO	1.78 (0.55)	1.54	0.35 (0.58)	0.01 (0.01)	0.12 (0.29)	0.00	22.69 (0.77)				
CaO	0.17 (0.21)	1.74	0.47 (0.19)	40.71 (0.47)	28.13 (1.04)	29.53	0.01 (0.00)				
Na ₂ O	0.05 (0.05)	0.40	0.06 (0.04)	0.02 (0.02)	0.02 (0.01)	0.46	0.00 (0.00)				
Total	94.51 (1.37)	97.37	88.70 (1.67)	97.92 (0.45)	98.66 (2.18)	102.40	98.27 (0.68)				
Cations based on oxygens	4	3	3		3	5	16	4			
Si	0.005 (0.004)	0.146	0.006 (0.005)	0.026 (0.019)	1.010 (0.034)	3.098	0.000 (0.000)				
Ti	0.280 (0.153)	0.802	0.001 (0.001)	0.944 (0.008)	0.892 (0.053)	0.084	0.000 (0.000)				
Al	0.117 (0.048)	0.032	0.001 (0.001)	0.012 (0.004)	0.065 (0.019)	2.880	1.965 (0.012)				
Cr	0.005 (0.006)	0.004	0.000 (0.000)	0.000 (0.000)	0.001 (0.001)	0.000	0.002 (0.001)				
Fe ²⁺	1.145 (0.181)	0.774	0.000 (0.000)	0.000 (0.000)	0.002 (0.007)	0.000	0.145 (0.023)				
Fe ³⁺	1.311 (0.288)	0.095	1.478 (0.985)	0.015 (0.003)	0.033 (0.022)	0.022	0.033 (0.013)				
Mn	0.028 (0.009)	0.018	0.001 (0.001)	0.001 (0.000)	0.002 (0.002)	0.000	0.008 (0.002)				
Mg	0.098 (0.029)	0.057	0.002 (0.002)	0.000 (0.000)	0.006 (0.014)	0.000	0.847 (0.024)				
Ca	0.006 (0.008)	0.046	0.009 (0.007)	1.000 (0.014)	0.985 (0.033)	2.942	0.000 (0.000)				
Na	0.003 (0.004)	0.019	0.003 (0.002)	0.001 (0.001)	0.001 (0.001)	0.082	0.000 (0.000)				

1
2

Table 9: Average interstitial glass and melt inclusion compositions for the zones in the magmatic skarn xenoliths. Analyses are reported as the mean with one standard deviation in brackets

Glass Type Zone n	Interstitial Glasses										Melt Inclusions			
	Host Lava	R1	R2	R4	Core	R1	R4 and Core							
	15	11	15	48	12	12	70							
SiO ₂	70.45 (3.36)	69.02 (2.54)	71.07 (2.76)	73.23 (2.21)	73.32 (1.78)	63.99 (3.03)	67.38 (3.72)							
TiO ₂	0.42 (0.11)	0.37 (0.10)	0.31 (0.14)	0.35 (0.13)	0.32 (0.09)	0.44 (0.05)	0.40 (0.19)							
Al ₂ O ₃	13.75 (1.83)	13.29 (0.95)	13.47 (1.17)	12.00 (0.88)	12.6 (0.38)	17.55 (0.82)	13.33 (1.97)							
Cr ₂ O ₃	0.01 (0.01)	0.01 (0.01)	0.01 (0.01)	0.01 (0.01)	0 (0.01)	0.02 (0.02)	0.01 (0.01)							
FeO	2.59 (0.79)	3.03 (0.15)	2.52 (0.28)	2.22 (0.46)	2.22 (0.56)	2.55 (0.56)	2.84 (1.31)							
MnO	0.12 (0.08)	0.13 (0.05)	0.10 (0.04)	0.07 (0.03)	0.05 (0.03)	0.13 (0.04)	0.09 (0.06)							
MgO	0.40 (0.57)	0.12 (0.09)	0.12 (0.12)	0.06 (0.06)	0.07 (0.04)	0.33 (0.22)	0.35 (0.90)							
CaO	1.05 (1.04)	4.71 (1.79)	2.49 (1.29)	3.04 (1.15)	2.26 (0.97)	2.44 (0.52)	5.87 (3.47)							
Na ₂ O	3.89 (1.15)	3.41 (0.46)	3.59 (0.46)	3.22 (0.37)	3.32 (0.53)	4.01 (0.90)	3.43 (0.74)							
K ₂ O	5.28 (0.72)	4.20 (0.52)	4.71 (0.80)	4.51 (0.56)	4.92 (0.50)	3.82 (1.03)	4.00 (0.99)							
P ₂ O ₅	0.12 (0.12)	0.08 (0.05)	0.07 (0.08)	0.09 (0.36)	0.04 (0.02)	0.23 (0.08)	0.08 (0.04)							
SO ₃	0.01 (0.01)	0.06 (0.03)	0.01 (0.01)	0.02 (0.02)	0.00 (0.01)	0.11 (0.05)	0.03 (0.03)							
Cl	0.21 (0.16)	0.27 (0.03)	0.26 (0.03)	0.29 (0.07)	0.28 (0.04)	0.29 (0.02)	0.34 (0.11)							
F (ppm)					0;00 (0.00)		184 (326)							
Total	98.26 (1.38)	98.63 (0.83)	98.73 (1.56)	99.09 (0.92)	99.39 (1.12)	95.53 (3.48)	98.14 (1.97)							

3